Redox Chemistry of Hydrated Metal Ions

Dissertation

zur Erlangung des Doktorgrades

der Mathematisch-Naturwissenschaftlichen Fakultät

der Christian-Albrechts-Universität zu Kiel

vorgelegt von

Ina Gernert

Kiel, 2015

Erster Gutachter: Prof. Dr. Martin K. Beyer
Zweiter Gutachter: Prof. Dr. Bernd Hartke

Tag der mündlichen Prüfung: 08.12.2015
Zum Druck genehmigt: 09.12.2015

gez. Prof. Dr. Wolfgang J. Duschl, Dekan

Die gute Zeit fällt nicht vom Himmel, sondern wir schaffen sie selbst; sie liegt in unserem Herzen eingeschlossen.

(Fjodor M. Dostojewski)

Für meine Eltern und Claus

Abstract

This thesis focuses on the gas phase chemistry of hydrated metal cations $[M(H_2O)_n]^+$, M = V, Cr, Mn, Fe, Co, Ni, Cu and Zn, in a cluster size regime of n = 20-50. The experiments were performed on a FT-ICR mass spectrometer with an external laser vaporization ion source. Additionally specific aspects were investigated by theoretical calculations.

Ligand exchange for all metal ions was observed with acetonitrile. For Cr(I) electron transfer to the acetonitrile molecule is assumed due to the high reaction enthalpy ΔE_{nc} = –195 ± 26 kJ mol^{-1}. Furthermore the oxidation of the metal center ion Zn^+ to Zn^{2+} followed by a proton transfer to acetonitrile and formation of $ZnOH^+$ was observed.

Oxidation reaction and ligand exchange occured in the reaction with 1-iodopropane. The ligand exchange reaction is sensitive to the size of the solvation shell and takes place mostly at longer reaction delays, i.e. small clusters. Cr, Co and Zn are oxidized to the oxidation state II by the formation of MI^+ ions. For Co^+ and Ni^+ the formation of $[MC_3H_6(C_3H_7I)_2]^+$ is observed. An oxidative insertion of the metal ion into the C-I bond and a β-H atom migration is assumed to rationalize the formation of the olefin.

No reaction was observed for Cu^+ and Zn^+ with C_6H_5X, X = F, Cl, Br and I, for fluorobenzene. Ligand exchange of up to four molecules of C_6H_5X, X = Cl, Br and I, is observed for $[Cu(H_2O)_n]^+$. Formation of the hydrated organometallic $C_6H_5Zn^+$ ion is formed in the reaction of $[Zn(H_2O)_n]^+$ with C_6H_5Cl. Further with C_6H_5X, X = Br and I, efficient formation of hydrated $ZnBr^+$ and ZnI^+ is observed. DFT calculations for the thermochemistry of the Zn^+ cation reactions demonstrate the influence of the water molecules. Only in an aqueous environment the formation of ZnI^+ and $ZnBr^+$ is thermodynamically preferred.

$[V(H_2O)_n]^+$, n = 8-12, are studied by theoretical calculations with density functional theory. Geometry optimizations show that the $[HVOH]^+$-core geometry is the most stable one. Furthermore the IR-spectra indicate a mobile proton for the $[V(H_2O)_n]^+$, n = 8-10, with hydroxide geometry, which depends on the geometry of the first solvation shell. The next stable geometry is a four square-planar coordinated structure with $[V(H_2O)_4]^+$ core.

Kurzzusammenfassung

Diese Arbeit befasst sich mit der Gasphasenchemie von hydratisierten Metallkationen $[M(H_2O)_n]^+$, M = V, Cr, Mn, Fe, Co, Ni, Cu und Zn, in einem Größenereich von n = 20-50. Die Experimente wurden mittels eines FT-ICR Massenspektrometers mit einer externen Laserverdampfungsquelle durchgeführt. Zusätzlich wurden einige Aspekte mit theoretischen Rechnungen vertieft.

Bei der Reaktion mit Acetonitril wurde Ligandenaustausch für alle Metalle beobachtet. Bei Cr(I) weist die hohe Reaktionsenthalpie von $\Delta E_{nc} = -195 \pm 26$ kJ/mol^{-1} einen Elektronentransfer zum Acetonitrilmolekül hin. Außerdem wurde die Oxidation des Metallkerns Zn^+ zum Zn^{2+} gefolgt von einem Protonentransfer und der Bildung von $ZnOH^+$ beobachtet.

Oxidationsreaktion und Ligandenaustausch wurden für die Reaktion mit 1-Iodpropan untersucht. Der Ligandenaustausch ist abhängig von der Größe der Solvathülle und wird erst bei längeren Reaktionszeiten beobachtet. Cr, Co und Zn werden bei der Bildung von MI^+ zur M^{2+} oxidiert. Bei Co^+ und Ni^+ wurde die Bildung von $[MC_3H_6(C_3H_7I)_2]^+$ festgestellt. Die Bildung des Olefins erfolgt wahrscheinlich durch die oxidative Insertion des Metallions in die C-I Bindung und der Verschiebung des β-H Atoms.

Keine Reaktion wurde bei Cu^+ und Zn^+ mit C_6H_5X, X = F, Cl, Br und I, bei Flurbenzol beobachtet. Es wurde der Ligandenaustausch von bis zu vier Molekülen von C_6H_5X, X = Cl, Br und I, für $[Cu(H_2O)_n]^+$ beobachtet. Die Bildung der metall-organischen Verbindung $C_6H_5Zn^+$ wurde bei der Reaktion von $[Zn(H_2O)_n]^+$ mit C_6H_5Cl beobachtet. Theoretische Rechnungen zur Thermochemie der Zn^+-Reaktionen zeigen den Einfluß der Solvathülle auf die Reaktion. Danach ist die Bildung von ZnI^+ und $ZnBr^+$ nur im wäßrigem Medium thermodynamisch bevorzugt.

Theoretische Rechnungen mittels Dichtefunktionaltheorie wurden für die $[V(H_2O)_n]^+$, n = 8-12, durchgeführt. Die Geometrieoptimierung ergibt, dass die Clustergeometrie mit einem $[HVOH]^+$-Kern am stabilsten ist. Des Weiteren weisen die IR Spektren auf ein mobiles Proton für die $[V(H_2O)_n]^+$, n = 8-10, mit Hydroxid-Geometrie. Dieses ist abhängig von der Geometrie der ersten Solvathülle. Die nächst stabilere Geometrie ist ein quadratisch-planar koordiniertes Metallion mit einem $[V(H_2O)_4]^+$-Kern.

Contents

List of Figures

List of Tables

List of Abbreviations

BIRD	blackbody infrared radiative dissociation
CAM	coulomb-attenuating method
CID	collision-induced dissociation
DFT	density functional theory
ESI	electrospray ionisation
FT	fourier transformation
GTO	gaussian type orbital
ICR	ion cyclotron resonance
IR	infrared
IRMPD	infrared multiphoton dissociation
LDA	local density approximation
m/z	mass-to-charge ratio
MS	mass spectrometry
MD	molecular dynamics
PBE	Perdew–Burke–Ernzerhof exchange correlation functional
PES	potential energy surface
UV	ultraviolet
UHV	ultrahigh vacuum
VASP	Vienna ab–initio simulation package
VIS	visible
TD-DFT	time-dependent density functional theory

1. Introduction

Water is a chemical compound consisting of one oxygen and two hydrogen atoms which provides the basis of live on this earth. Furthermore it is the most studied compound due to the different anomalies. The number of known anomalies for water is currently around seventy-two. [1] Due to the polar character of water molecules cluster are formed by hydrogen bonds. In the liquid state each water molecule is bound to 3.4 neighboring molecules by hydrogen bonds. [2] Although these bonds are not covalent, there is a highly ordered structure. Without the hydrogen bonds water would be a gas under standard conditions. [2] Hydrogen bonds are responsible for a further property: polar compounds, also known as hydrophilic compounds, as well as ions have good solubility in water.

Gas phase systems consisting of a solvated ion surrounded by a certain number of water molecules (so called "Nanodroplet") are good model systems for studies on the solubility and reactions in aqueous environment. [3] For $X^{+/-}(H_2O)_n$ clusters, where X can be any element, it has been shown that they behave like in bulk aqueous solutions [4,5] and that concepts such as pH and solubility have equivalents on the single ion level. [6] During the solvation of ions different inter- and intra-molecular reactions can occur, for example charge transfer or neutralization, due to the ion-solvent interactions. For example an ion association (equation 1.1), electron- or proton transfer (equation 1.2/1.3) or a conformation change (equation 1.4) of the ion can appear. [7]

$$M^{n+} + X^{m-} \xrightarrow{solvent} MX^{(n-m)+} \; ion\ association \tag{1.1}$$

$$M^{+} + X \xrightarrow{solvent} M^{2+} + X^{-} \; ion\ transfer \tag{1.2}$$

$$M^{+} + X \xrightarrow{solvent} [MOH]^{+} + XH \; proton\ transfer \tag{1.3}$$

$$RHX^{+} \xrightarrow{solvent} RXH^{+} \; rearrangement \tag{1.4}$$

However, gas phase systems are suitable to observe the influence of the solvent on the ion and its reactions.

Experiments with bare transition metal ions and metal clusters in the gas phase enable us to obtain information about reactions with various organic reactants. [8–10] A large number of metal clusters and bare metal ions can activate the C-H- or C-C- bond. [9] Despite the multi–faceted results trends can be observed for the activation:

- The activation of alkanes is most efficient for metal cations, since they interact as electrophile. [11]

- The activation is quenched for most metal ions by ligands. [9]

With respect to new coupling reactions using metal ions many open questions still exist. Also the field of metal halides, which are used beside the oxides as catalysts [12,13], has some open questions. Furthermore, the influence of the solvent is neglected and therefore the results are not transferable to liquid phase chemistry.

Hence hydrated transition metal ions consisting of a central metal ion surrounded by a solvation shell of water molecules provide an interesting medium for studies of aqueous transition metal chemistry in the unusual oxidation state +I. [3] Due to the high hydration energies of multiply charged cations their disproportionation is exothermic in water. [3] Detailed information about non–covalent interactions and their dependence on charge and electron configuration of the metal, even the effect of the metal on geometry and binding of the ligands, were possible due to experiments in the gas phase. [14–19]

Moreover thermochemical information can be obtained by the number of evaporated water molecules during the reaction. Williams et al. [7,20] determine absolute electrode potentials from gas phase experiments by mass selected hydrated multiply charged cations reacting with free electrons. Thus, they can investigate electrochemistry in the gas phase. Höckendorf et al. [21] introduced in 2010 a new variant of nanocalorimetry method, where no mass selection is required and which works in a room temperature environment. Hence, the possibility is given to determine the enthalpy of the reaction by measuring mass spectra at different time delays. This method was used for the reactions in chapter 3,4 and 5 to learn more about the diffrent reactivity of the metal ions.

To get more insight into the chemistry of hydrated metal ions the interaction of the reactant with the clusters were investigated by Fourier-transform ion-cyclotron resonance (FT-ICR) mass spectrometry.

In chapter 3 the interaction of the first row trans metal ions with acetonitirle is studied in detail. Lam et al. [22] showed the reduction of acetonitrile due to the reaction of hydrated Mg(I). The valence electron of Mg^+ is solvated by the water molecules and can reduce acetonitrile molecules followed by a proton transfer to the acetonitrile molecule. Therefore, further studies were performed to investigate the interaction between acetonitrile and the d electrons of the transition metal ions.

Based on experiments with bare metal ions for the activation of C-C [23] or C-X [24] bonds, experiments of metal cations in aqueous environment with aliphatic and aromatic compounds were performed (shown in chapter 4 and 5). A previous study of transition metal cations $[M(H_2O)_n]^+$, M = Cr, Mn, Fe, Co, Ni, Cu and Ag, in water clusters with HCl show the uptake of HCl. [6] However, loss of HCl is determined at a specific number of water molecules left in the cluster. But in the reaction with hydrated zinc cations, Zn(I) is oxidized and hydrogen is reduced upon uptake of a second HCl molecule. [6,25] These studies can give information about the thermodynamics and kinetics of the reactions and provide valuable insight into the role of metals as catalyst.

Extensive theoretical calculations were performed for the blackbody radiation induced fragmentation of $[V(H_2O)_n]^+$, n = 8-12, shown in detail in chaper 6. Due to the collision-free environment in the measurement cell the clusters absorb infrared photons from the apparaturs walls. Since the clusters are not stable at room temperature, they cool themselves by evaporating one water molecule at a time. [3] For $[V(H_2O)_n]^+$ the formation of atomic and molecular hydrogen is observed in a narrow cluster size range. [26] A assumption of the observation are different geometries of the cluster. Therefore geometry optimization and calculation of absorption spectra with density functional theory (DFT) and time-dependent DFT were performed for future studies with spectrosopy. TD-DFT is the most popular method to calculate exited states of metal complexes, since the obtained results are in a quantitative agreement with the experiment and the computantional costs are relatively low. [27] A combination of the calculations with spectroscopic experiments will enable a better understanding of the reaction of $[V(H_2O)_n]^+$, n = 8-12, with infrared photons in the future.

2. Experimental and Theoretical Methods

2.1. FT-ICR Mass Spectrometry

Mass spectrometry is an important tool for chemical analytics in a wide range of applications. The basis for ion cyclotron resonance mass spectrometry was founded by Lawrence and Livingston [28] in 1932. Due to the combination of Fourier Transformation (FT) with ICR-MS by Comisarow and Marshall [29] in 1974 it became more powerful for MS applications. FT-ICR-MS offers high mass resolution, high mass accuracy, simultaneous detection of all ions and long ion storage times. Therefore it can be used as a laboratory for gas phase chemistry. A typical FT-ICR-MS experiment consists of a combination of temporally separated events like ion formation, ion storage, mass selectrion and detection, which are discussed briefly on the next pages.

2.1.1. General

An ion with mass m and charge q moving in a spatially uniform magnetic field B is directed by the Lorentz force to rotate about the magnetic axis direction as shown in figure 2.1 with the cyclotron frequency ω_c:

$$\omega_c = \frac{q * B}{m}. \tag{2.1}$$

Due to equation 2.1 all ions of a given mass-to-charge ratio $\frac{m}{q}$ have the same ICR frequency, hence which is independent from velocity and thus kinetic energy of the ion.

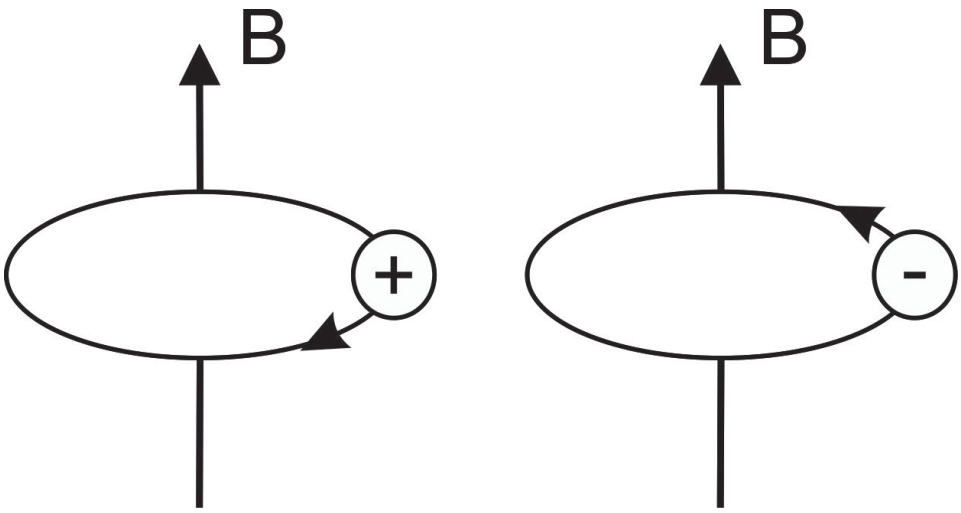

Figure 2.1.: Ion cyclotron motion. Ions rotate in a plane perpendicular to the direction of the magnetic field. Adapted and modified from Ref. [30] with permission from Elsevier.

The ion cyclotron motion is not by itself useful. Due to the different random time intervals and therefore different random phase of ions with the same $\frac{m}{q}$ ratio, a detectable macroscopic signal cannot be produced. [30] Additional the cyclotron radius of a thermal ion is too small to induce a detectable signal, even if all ions have the same cyclotron phase.

Therefore an excitation is necessary before detection. During such an excitation produced by applying an electric field the dimension of the initial ion packet remain the same and the packet is accelerated along a spiral trajectory, as shown in figure 2.2.

The coherent ion packets are inducing an electric potential between the detection plates. This potential is oscillating with the cyclotron frequency and can be detected. This signal is amplified and recorded by fast analog digital converter as a digital transient. Using Fourier transformation the digital transient, which depends on the frequency, is transformed to the frequency domain. From equation 2.1 the mass to charge ratio is obtained. Collisions with neutral background gas and Coulomb repulsion of the ions among

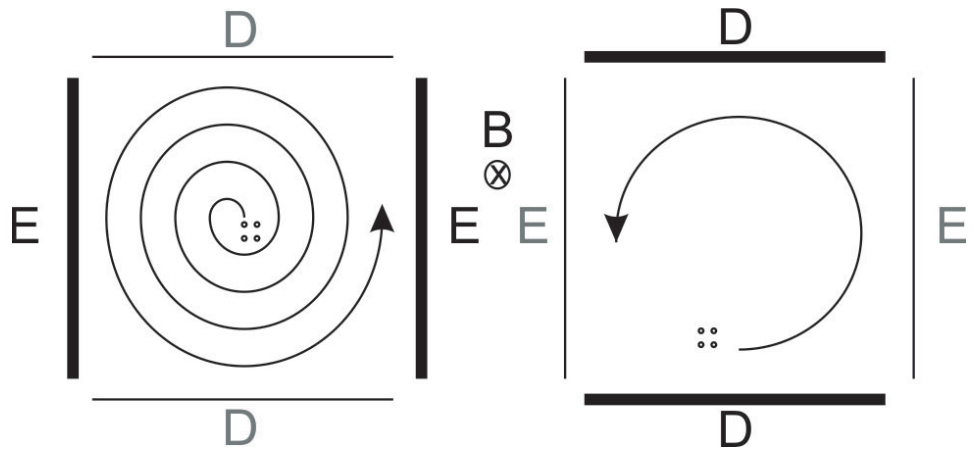

Figure 2.2.: Incoherent ion cyclotron motion (left) is transformed by excitation to a coherent detectable motion (right). Adapted and modified from Ref. [30] with permission from Elsevier.

each other cause an exponential decay of the measured signal. Therefore experiments are performed under ultra high vacuum conditions below 10^{-8} mbar. A homogeneous magnetic field is not sufficient to confine the ions, since they can move along the direction of magnetic field. An electrostatic potential field is needed for trapping the ions. The theoretically simplest trap is based on an axial quadrupolar electrostatic trapping potential, which can be realized experimentally with hyperbolically shaped electrodes. Various ion trap geometries are known, see reference [30]. Measurements in our labarotory were performed with the Bruker *Infinity cell* [31], which is based on the cylindrical cell.

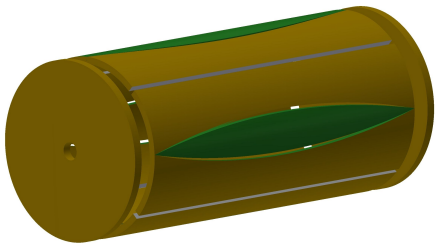

Figure 2.3.: New FT-ICR cell design with hyperbolic electric field. Adapted and modified from Ref. [32] with permission from John Wiley & Sons, Ltd.

The electrostatic trapping field has consequences for the motion, hence an axial oscillation and a magnetron drift centered in the trap symmetry axis appear. The magnetron motion is metastable, because it has a reversed energy spectrum. Therefore a large magnetron radius corresponds to low energy and the loss of the ions from the trap occurs whenever energy is drawn.

Therefore a new commercial cell is available, which is shown in figure 2.3. An hyperbolic field is used to create an electric field configuration that leaves the cyclotron frequency of the ions independent of their axial motion. [32]

2.1.2. FT-ICR MS for Cluster Research

All Experiments were performed on a modified *Bruker/Spectrospin* CMS47X FT-ICR [33], shown schematically in figure 2.4. The 4.7 Tesla unshielded superconducting magnet contains a 150 mm room temperature bore, where the *Bruker* infinity cell (yellow) is located. Ions are generated by the laser vaporization source in the first source chamber and are transported through four differential pumping stages via a system of electrostatic lenses into the ICR cell.

The average operating pressure in the first source chamber is in the order of 10^{-4} mbar and in the second chamber 10^{-6} mbar. A skimmer (white) separates source chamber I from chamber II. Furthermore the ultrahigh vacuum area can be separeted from the two source chambers with a gate valve (black) to avoid venting of the ultrahigh vacuum during maintenance work on the source.

To overcome the inhomogeneous stray field of the magnet, the ions are accelerated to 3 keV. For trapping they are decelerated in front of the ICR cell. The differential pumping stages enable an average pressure in the range of 10^{-10} mbar in the ICR cell. Moreover the ions can be trapped in the measurement cell on a timescale of few a milliseconds to minutes. Thereby the possibility is given to examine chemical reactions at defined pressure and temperature. Neutral reactants are introduced into the UHV region through a needle valve (*Balzers*, UH40). Liquid reactants with vapor pressure $\geq$ 10 mbar can be used. It is even possible to introduce corrosive reaction gases, since the needle valve consists of a sapphire-copper-gasket which can be exchanged by a gilded gasket. For the pressure measurements in the source chambers and the ultrahigh vacuum

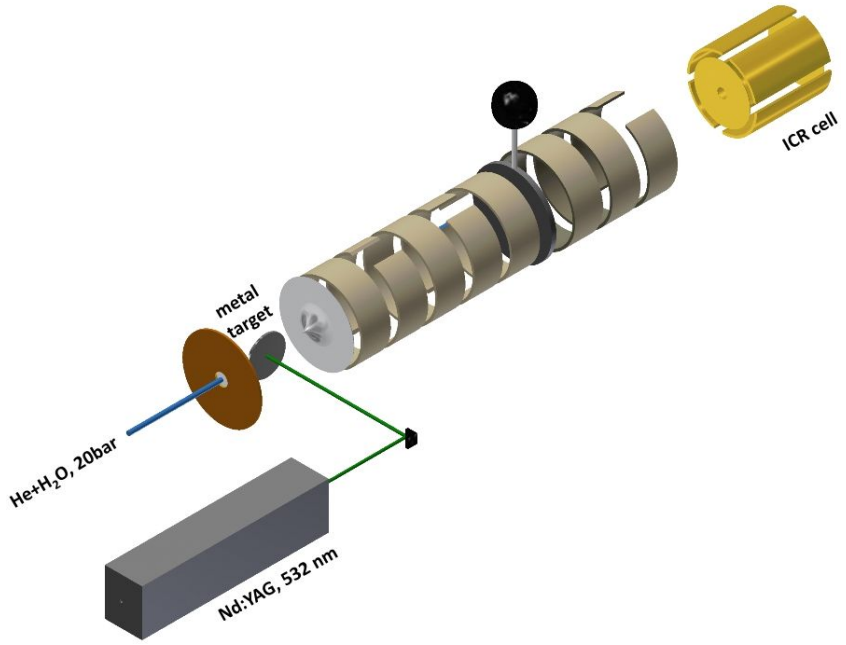

Figure 2.4.: Schematics of the FT-ICR mass spectrometer for cluster experiments. Ions are produced by the laser vaporization source using a Nd:YAG laser and are transported by a system of electrostatic lenses (grey) into the ICR cell (yellow).

region high vacuum cold cathode gauges are used. In the ultrahigh vacuum region the cathode gauge is located in front of the turbopump, so the molecular beam is not attented. Consequently the real pressure deviates from the measured pressure, since the distance to the cell amounts to at least 80 cm. Thus, a correction of the measured pressure is necessary. [34]

All experiments are directed on a *Windows XP Professional* computer via APEX III datastation by the measuring and control software *Bruker X-Mass 7.0.8*.

2.1.3. Laser vaporization source

The monovalent hydrated transition metal water clusters $[M(H_2O)^+]_n$ are produced in the external laser vaporization source, developed independently by Bondybey and Smalley. [35–37] A schematic picture of the external source is shown in figure 2.5.

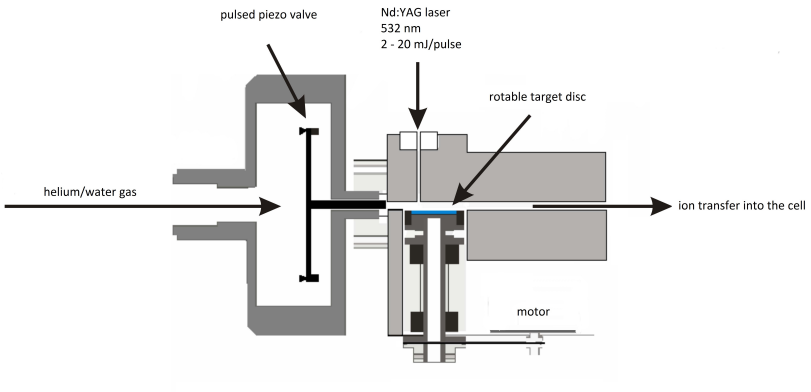

Figure 2.5.: Schematics of the external laser vaporization source. Metal plasma is produced by laser vaporization of a rotating target disc. Adapted and modified from Ref. [38] with permission from Taylor & Francis, 2002.

A laser pulse with a wavelength of 532 nm (Continuum Surelite II Nd:YAG laser) is focused on a rotating metal target, which can be changed according to the metal of interest. The laser is operating with an average energy of 12 mJ per pulse and a pulse length of 5 ns. Thus metal plasma is produced. Further the metal plasma is entrained in a supersonic expansion of the carrier gas into high vacuum. This carrier gas is helium 4.6 (maximum 20 bar), which is passing a cooling trap filled with water. Here helium is enriched with water vapour. All gas lines and the cooling trap are flushed with helium before each experiment for ideal conditions. The carrier gas pulse is provided by a piezoelectric valve.

In the supersonic expansion charged and neutral species are produced by collisions between the plasma and the carrier gas. The cluster distribution depends on the cell opening time, time of flight delay, and piezo valve delay as well as the pulse width. For every experiment the parameters are optimized for the best signal intensity. During the adiabatic supersonic expansion into the ultrahigh vacuum region the clusters are stabilized and cooled down due to collisions among themselves and with the carrier gas. Selection between negatively and positively charged clusters is possible by the polarity of the skimmer and ion transfer.

2.1.4. Sequence of a typical ICR experiment

Hydrated monovalent metal ions $[M(H_2O)_n]^+$ were generated by using isotopically enriched targets [39] where applicable: ^{52}Cr (99.9%), ^{56}Fe (99.7%), ^{58}Ni (99.9%), ^{63}Cu (99.3%) and ^{64}Zn (99.4%) (*STB Isotope Germany GmbH*).

The following chemicals were introduced into the ultrahigh-vacuum region by a needle valve at a constant pressure in the range of 3 x 10^{-9} mbar to 4 x 10^{-7} mbar: Acetonitrile (Sigma-Aldrich, $\geq$ 99.9%), fluorobenzene (Sigma-Aldrich, $\geq$ 99.5%), chlorobenzene (Sigma-Aldrich, 99%), bromobenzene (Sigma-Aldrich, 99%), iodobenzene (Sigma-Aldrich, 98%) and iodopropane (Sigma-Aldrich, 99%).

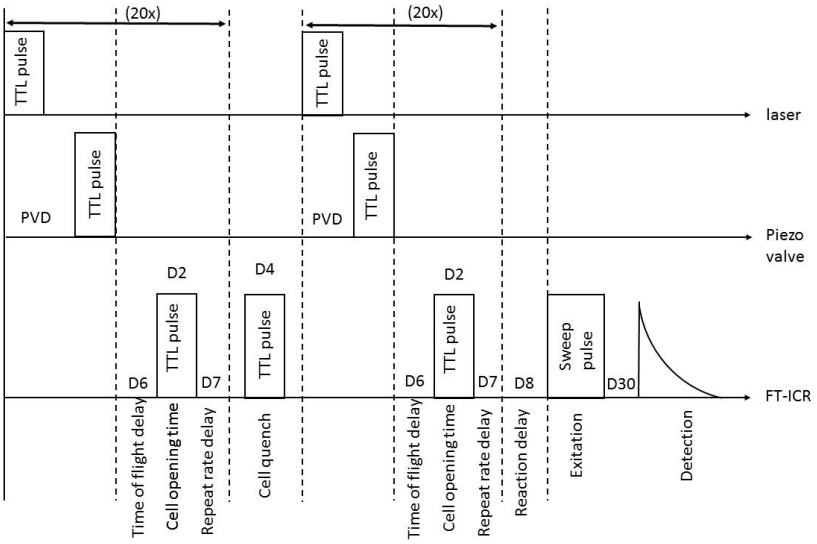

Figure 2.6.: Real time pulse schema of a typical ICR experiment. The external laser vaporization source is coupled to the measurement cycle of the ICR. Based on Ref. [40]

A typical pulse sequence of the experiments is shown in figure 2.6. The experiment starts with 20 laser shots to heat the laser system for minimizing the drift of the initial cluster size distribution. It is coupled with a gas pulse to avoid contaminations of the source. A quench puls (D4) is applied to clean the cell from ions. Thereafter the cell is filled by 20 cycles of laser vaporization, pulsing of the piezo valve and trapping. The TTL pulse (D2) is lowering the voltage of the first trapping plate, so the ions can pass into the cell. The time of flight delay (D6) and the cell opening time (D2) are used to

define the cluster size distribution. The fill cycle is necessary for a better signal-to-noise ratio, which leads to a higher signal intensity.

With the reaction delay (D8) it is possible to monitor the reactions by recording mass spectra at different reaction delays. Since the fill cycle (20 cycles of heating the laser + 20 cycles of laser vaporization) for the cell takes 2 s, some ions may have already reacted at nominal D8 = 0 s.

Finally the trapped ions are excited by a sweep pulse and the transient is detected. To ensure that the transient is not affected by the sweep pulse, excitation and detection are separated by D30.

2.2. Cluster Properties

2.2.1. Blackbody infrared radiative dissociation

A typical cluster distribution for hydrated monovalent metal ions $[M(H_2O)_n]^+$, M = Mn, is shown in figure 2.7. For nominal 0 s reaction delay the metal ion is solvated by n = 10 - 40 water molecules. While the clusters are stored in the measurement cell, they are losing water molecules continuously due to the absorption of infrared photons. After 7 s reaction delay the metal ion is solvated by n = 5-20 water molecules.

Even in the collision free environment of the ICR cell loss of water molecules is observed. The clusters are continously heated by the absorption of blackbody infrared radiation from the ICR cell walls. Consequently evaporative cooling, named blackbody infrared radiative dissociation (BIRD), results. [41–44] The loss of water molecules, shown in equation 2.2, follows pseudo-first-order kinetics [45] and shows a linear dependence on the number of water molecules in the cluster. [41]

$$X^{+/-}(H_2O)_n + h\nu_{IR} \rightarrow X^{+/-}(H_2O)_{n-1} + H_2O \tag{2.2}$$

Furthermore the loss of water molecules is linearly dependent on the absorption of photons and the intensity of black-body infrared radiation (BIRD), which overlaps with

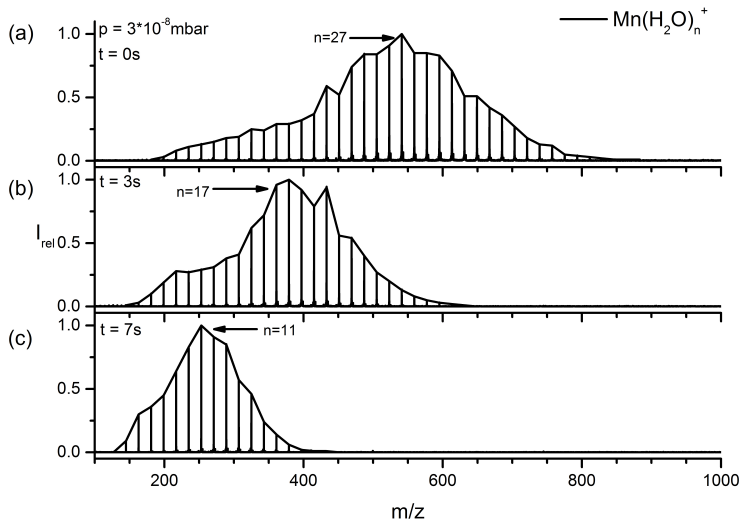

Figure 2.7.: Mass spectra of $[Mn(H_2O)_n]^+$ after 0 s (a), 3 s (b) and 7 s (c) reaction delay at 3 x 10^{-8} mbar (with iodopropane). Blackbody infrared radiative dissociation is observed for the hydrated manganese clusters.

the Planck distribution. Since the water molecules in the clusters are bound by hydrogen bonds, loss is favored due to the overlapping of the vibrational levels with the room-temperature Planck function for blackbody radiation. [41]

The absorption of infrared photons with the energy $h\nu$ leads to heating of the cluster until a water molecule evaporates. This requires an energy about 43 kJ mol^{-1}. [46] Moreover evaporation stops, when a thermal equilibrium is reached and the infrared photon absorption and emission is in balance. On the one hand the clusters reach a size, where the evaporation is inefficient due to stronger interactions between the first solvation shell and the metal core, so the loss of a further water molecule requires more energy. On the other hand loss of degrees of freedom and the absence of low frequency modes in the smaller clusters cause the decrease of the efficiency of the absorption. [41] Furthermore small clusters do not have enough internal energy for dissociation.

In addition for hydrated electrons $[(H_2O)_n]^-$ besides the loss of water molecules electron detachment is observed for clusters with $n \leq 32$. [47] For clusters with less than 20 water molecules the electron detachment is the main reaction pathway. This reaction pathway does not occur with hydrated metal ions.

2.3. Data Analysis

For the investigation of the different reactions and the reactivity of the hydrated metal ions, mass spectra at different reaction delays and pressure were recorded for each metal. The reaction delays and the pressure varies depending on the reactivity of the metal. Based on the clusters size and the intensity as a function of time, the reaction rates and nanocalorimetry reaction enthalpy can be determined. The necessary basics are discussed in detail in the following sections.

2.3.1. Kinetic Analysis

For the kinetic analysis of the reactions a pseudo-first-order law [48] can be used, if one reactant is present in large excess. This condition is fullfilled in the ICR cell, since the pressure of the neutral reactant gas is in the range of 10^9 molecules cm^{-3} in comparison the trapped ions with 10^6 ions cm^{-3}. [49]

For the time decay of the particle density N equation 2.3 is valid.

$$\frac{dN}{dt} = -kN \tag{2.3}$$

The particle density is directly proportional to the measured intensity (equation 2.4), thus it can be used directly for the further evaluation and determination of the relative rate constant k.

$$\frac{dI}{dt} = -kI \tag{2.4}$$

The equation 2.4 is only valid for a simple reaction A + B $\rightarrow$ C and does not include consecutive reactions. However, equation 2.4 can be expanded via a matrix to 2.5 to include consecutive and parallel reactions.

$$\frac{\partial \vec{I}}{\partial t} = \mathbf{K} \cdot \vec{I} = \begin{pmatrix} k_{11} & \cdots & k_{1n} \\ \vdots & \ddots & \vdots \\ k_{m1} & \cdots & k_{mn} \end{pmatrix} \cdot \vec{I} \tag{2.5}$$

The matrix **K** describes a coupled system with n ions and the corresponding reaction rates k_{nm}. Furthermore the column vector $\vec{I}$ contains the associated intensities. For a short time interval Δt = t_2 - t_1 the equation 2.5 can be approximated with a unit matrix **E**.

$$\frac{\vec{I}_{(t2)} - \vec{I}_{(t1)}}{\Delta t} = \mathbf{K} \cdot \vec{I}_{(t1)} \rightleftharpoons \vec{I}_{(t2)} = \mathbf{K}\Delta t + \mathbf{E} \cdot \vec{I}_{(t1)} \tag{2.6}$$

With the equation 2.6 the relative rate constant k *(s^{-1})* can be determined numerically by intensity-time charts. Furthermore the absolute rate constant k_{abs} *($cm^3 s^{-1}$)* can be obtained by equation 2.7.

$$k_{abs} = \frac{k_{rel}}{\rho} \tag{2.7}$$

Using $\rho = \frac{N}{V}$ and the expression pV = Nk_bT due to the perfect gas law, equation 2.8 is developed.

$$k_{abs} = K_p \frac{k_{rel} k_b T}{p_x^{exp}} \tag{2.8}$$

The pressure is corrected with an empirical method, shown in equation 2.9, with the pressure read from the sensor p_x^{exp}. Therefore the pressure correction factor K_p is obtained for describing the actual pressure in the cell p_x^{cell}.

$$p_x^{cell} = \frac{G}{R_x} * p_x^{exp} \tag{2.9}$$

The geometry factor G is independent of reaction gas and pressure range and has an experimental value of 3.7 $\pm$ 1.0. Moreover the sensitivity R_x of the pressure gauge can be estimated by equation 2.10 using polarizabilities α of the reactants. [50]

$$R_x = 0.36 * \alpha + 0.3 \tag{2.10}$$

The summed intensities belonging to one cluster distribution are normalized and the intensity-time charts can be fitted by equation 2.6. Using a genetic algorithm, rate constants are extracted with software *Analyzze* [51] developed in the group. Therefore

the intensity at t = 0 s and the allowed reaction pathways are necessary for starting the optimization.

Genetic algorithms try, starting from one or more possible solutions, to reach the optimal solution stepwise. The fundamental idea is based on the biological evolution, where starting from a random initial population a child population is generated by applying genetic factors like selection, recombination and mutations. [52, 53] By the formation of further child populations the optimum is reached gradually. The population, which has the best approximation to the optimum at the termination, appears as a solution for the problem. Additionally the termination criterium is the number of population cycles, which is defined by the user. For the evaluation of the result an error is given, which results from the differences between the theoretical and experimental values.

The relative error of the measured absolute rate constants is 25 %, which is due to the uncertainty of the pressure measurement in the ICR cell.

2.3.2. Nanocalorimetry

Besides the investigation of reaction kinetics also thermochemical information can be obtained with mass spectrometry. [7] The nanocalorimetric reaction enthalpy can be estimated from the number of water molecules evaporating during the reaction. [21] This works if the reaction is full ergodic, the reaction rate is independent of the cluster size and the internal energy does not effect the reaction rate. [21] The necessary equations are derived below. [21]

The total intensities of the educts (I_E) and products (I_P) follow pseudo-first-order behaviour.

$$\frac{dI_E}{dt} = -kI_E = \frac{dI_P}{dt} \tag{2.11}$$

Due to the influence of blackbody radiation the educt clusters shrinking. This influence is described with the parameter m, which represents the slope of the linear size dependence of the fragmentation rate due to BIRD. The rate constant $k_{f,e}$ is a linear function of the cluster size N_E, shown in equation 2.12.

$$k_{f,E} = k_{0,E} + mN_E \tag{2.12}$$

The equation 2.12 applies to educts and products. The change of the average cluster size for the educt clusters is described by equation 2.13.

$$dN_E = -k_{f,E}(N_E)dt = -(k_{0,E} + mN_E)dt \tag{2.13}$$

The change of the average cluster size of the products depends not only on the blackbody radiation but also on the reaction itself. Both contributions are described in equation 2.14.

$$dN_P = -k_f(N_P - N_{0,P})dt + (N_E - \Delta N_{vap} - N_P)\frac{kI_E}{I_P}dt \tag{2.14}$$

Fit parameters are k_f, $N_{0,E}$, $N_{0,P}$, ΔN_{vap} and the boundary conditions, like the average cluster size at t = 0 s. The slope k_f depends on the temperature, binding energy and infrared absorption intensity of the average water molecule in the cluster environment. [21] The experimental data is fitted with the programm *Nanocal 1.6* [54], where equation 2.14 is implemented.

The obtained value for ΔN_{vap} is converted to absolute thermochemical values using equation 2.14 for the total energy ΔE_{nc} released in the reaction:

$$\Delta E_{nc} = -\Delta N_{vap} * \Delta E_{vap} + \Delta E_{therm} \tag{2.15}$$

Evaporation of one water molecule requires ΔE_{vap} = 43.3 ± 3.1 kJ/mol in this cluster size range. [46, 55] ΔE_{therm} = 4.3 ± 0.5 kJ/mol takes the internal energy of the room-temperature reactant molecule and the contribution of the newly formed product ion to the heat capacity of the clusters into account. [21] Therefore ΔE_{nc} is the change in internal energy during the chemical reaction of the clusters.

An example for the nanocalorimetric results is shown in figure 2.8. Cluster sizes (a) and the difference (b) are fitted using a genetic algorithm. [53] The quality of the results is verified with the difference fit.

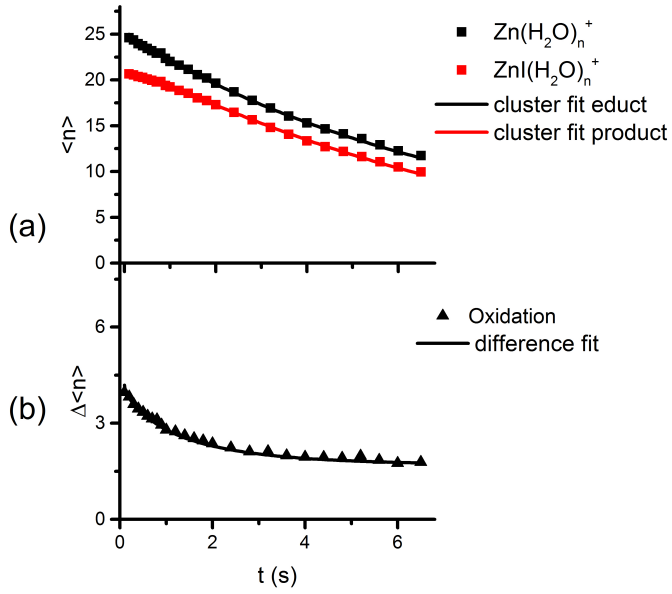

Figure 2.8.: Nanocalorimetric analysis of the reaction of $[Zn(H_2O)_n]^+$ with C_6H_5I at 4.5 x 10^{-8} mbar. The cluster fits (a) and the difference fit (b) are in good agreement with the data points of the average cluster size.

2.4. Quantum Chemical Methods

Most of the quantum chemical methods are based on the solution of the time independent Schrödinger equation 2.16 with the Hamilton operator $\widehat{H}$ of mass m_e in a hydrogen atom: [56]

$$\widehat{H}\Psi = E\Psi, \ \widehat{H} = -\frac{\hbar^2}{2m_e}\frac{d^2}{dx^2} + V \tag{2.16}$$

E describes the energy of the system relativ to a reference system, in which the nuclei are separated from the electrons and among themselves by infinite distance. Ψ is the wavefunction and the Hamilton operator introduces terms for the potential and kinetic energy. An exact solution is only possible for a two particle system, otherwise for larger systems approximation methods can be used.

For the Born-Oppenheimer approximation atomic nuclei and electrons are separated. The nuclear dynamics takes place on independent potential surfaces due to the neglection

of the coupling terms. This approximation provides reliable results for the the electronic ground state near to the equilibrium geometry. However, it fails for the transition states and closely neighboring or crossing electronic states. [57] With the Hartree-Fock method the energies are calculated from the wave functions of the system as an intrinsic value via the Hamilton operator. [58] Consequently, the energies and orbital coefficients are calculated until they do not change significantly, thus the energy is self consistent. The disadvantage of the method is, that the electron correlation energy is not included.

Ab initio methods obtain the solution without using empirical information. [56] To facilitate the calculations basis sets are used. A brief introduction of the used method and basis sets is given in the next section.

2.4.1. Density Functional Theory

The density fuctional theory is often used for theoretical calculations in molecular physics, since it provides with low computantional costs reliable results. The theory is based on the work of Hohenberg and Kohn. [59,60] They have shown that the electronic energy of a system can be described by the electron density without the exact wave function:

$$E_{DFT}(\rho) = E_{kin}(\rho) + E_{nc}(\rho) + E_{ee}(\rho) + E_{XC}(\rho) \tag{2.17}$$

Accordingly equation 2.17 the energy of a system can be separated in two parts. First the classic part with the kinetic energy of the electrons E_{kin}, the Coulomb interaction between the nuclei and the electrons E_{nc} and at least the Coulomb repulsion of the electrons E_{ee}. Second the exchange correlation term E_{XC}, which is including the remaining part of the interaction between the electrons. [61]

Furthermore the exchange correlation term includes the exchange energy due to the antisymmetry of the quantum mechanical wavefunction and the dynamic correlation due to the motion of the individual electrons. [61] Both terms are dependent on the electron density ρ.

$$E_{XC}(\rho) = E_X(\rho) + E_C(\rho) \tag{2.18}$$

Due to the density dependence both terms can be of two different types. On the one hand local functionals depend on the electron density, on the other hand gradient-corrected functionals depend on both electron density and its gradient $\nabla\rho$. [61]

Different enhancement are developed for a better description of the functional for the exchange correlation energy. Some of them are presented below.

Becke for example combined functionals of Hartree-Fock with the DFT exchange. [61]

$$E^{XC}_{hybrid} = c_{HF}E^{X}_{HF} + c_{DFT}E^{XC}_{DFT} \tag{2.19}$$

In particular the Becke-style three-parameter functional is developed from equation 2.19. [61] This was mostly used for the calculations in the dissertation.

$$E^{XC}_{B3LYP} = E^{X}_{LDA} + c_0(E^{X}_{HF} - E^{X}_{LDA}) + c_X E^{X}_{B88} + E^{C}_{VWN3} + c_C(E^{C}_{LYP} - E^{C}_{VWN3}) \tag{2.20}$$

The combination of different fuctionals for the correlation with the exchange is scaled with the parameters c_0, c_x and c_c. c_0 describes the mixture of the Hartree-Fock with the LDA local exchange. For the local density approximation (LDA) the density is treated as a uniform electron gas. [62]

$$E^{X}_{LDA} = -\frac{3}{2}\left\{\frac{3}{4\pi}\right\}^{1/3}\int \rho^{4/3}d^3r \tag{2.21}$$

For a better description equation 2.21 has been extended by Becke [63] with an generalized gradient approximation.

$$E^{X}_{B88} = E^{X}_{LDA} - \beta\rho^{1/3}\frac{x^2}{1+6\beta sinh^{-1}x}, x = \frac{|\nabla\rho|}{\rho^{4/3}} \tag{2.22}$$

The parameter β is determined to fit the known exchange energies of the inert gas atoms. Beckes gradient is included in equation 2.20 and is scaled by the parameter c_x. In addition two further functionals, E^{C}_{VWN3} and E^{C}_{LYP}, are combined in the B3LYP functional.

Using the DFT method, geometry optimization and vibrational analysis were carried out. With the frequency calculation the local minimum character of the geometry is verified, since an imaginary frequency is a sign for a transition state. Furthermore time-dependent DFT methods were employed the calculate UV/VIS spectra.

2.4.2. Basis Sets

Basis sets are introduced as an approximation of the wavefunctions. The molecular orbitals ψ_i are described as a linear combination of the atomic orbitals χ_μ, as shown in equation 2.23. [61]

$$\psi_i = \sum_{\mu=1}^{N} c_{\mu i}\chi_\mu \tag{2.23}$$

$c_{\mu i}$ is the molecular orbital expansion coefficient and describes the weighting of the atomic orbitals. The atomic orbitals are typically described by linear combinations of gaussian type orbitals (GTOs):

$$\chi_\mu = \sum_{p} d_{\mu p} g_p \tag{2.24}$$

where $d_{\mu p}$ is a fixed constant for a given basis set. The GTOs can be written in terms of polar or cartesian coordinates as shown in equation 2.25/2.26. [56]

$$g_{\zeta,n,l,m}(r,\Theta,\varphi) = NY_{l,m}(\Theta,\varphi)r^{2n-2-l}e^{-\zeta r^2} \tag{2.25}$$

$$g_{\zeta,l_x,l_y,l_z}(x,y,z) = Nx^{l_x}y^{l_y}z^{l_z}e^{-\zeta r^2} \tag{2.26}$$

Here, N is a normalization constant and Y are spherical harmonic functions. The exponent depends on the distance between the nucleus and electron. The sum of l_x, l_y and l_z describes the type of the orbital, for example if $l_x+l_y+l_z=1$ it is a p orbital. The GTO for the s orbital is shown in equation 2.27.

$$g_s(\zeta, r) = \left(\frac{2\zeta}{\pi}\right)^{3/4} e^{-\zeta r^2} \tag{2.27}$$

In this work the basis sets 6-311++g(3df,3pd) and aug-cc-pvqz were used. Furthermore effective core potentials were used for the elements Br, I and Zn. These elements have a large number of core electrons, which are less important in the chemical sense, but need a large number of basis functions for desribing the corresponding orbitals, otherwise the description of the valence orbitals can fail. [56] Furthermore relativistic effects complicate the issues. Hence, the explicit treatment is replaced by the effective core potentials, which also describe relativistic effects.

3. Reactivity of hydrated monovalent first row transition metal ions $[M(H_2O)_n]^+$, M = Cr, Mn, Fe, Co, Ni, Cu and Zn, n < 50, toward acetonitrile

Ina Herber, Wai-Kit Tang, Ho-Yin Wong, Tim-Wai Lam, Chi-Kit Siu, and Martin K. Beyer

The Journal of Physical Chemistry A,2015,119 (22), pp. 5566–5578
DOI: 10.1021/acs.jpca.5b02946

Own contributions presented in the paper:
FT-ICR mass spectrometry cluster experiments
Data analysis
Writing of the first version of the experimental results section

Abstract

Reactions of $[M(H_2O)n]^+$, M = Cr, Mn, Fe, Co, Ni, Cu, and Zn, n < 50, with CH_3CN are studied in the gas phase by Fourier transform ion cyclotron resonance (FT-ICR) mass spectrometry. Sequential uptake of 4–6 acetonitrile molecules is observed for all metals. Rate constants show a weak dependence on both the metal and the number of acetonitrile molecules already in the cluster. Nanocalorimetry yields the enthalpy of the first reaction step. For most metals, this is consistent with a ligand exchange of water against acetonitrile. For M = Cr, however, the strong exothermicity of ΔE_{nc} = –195 ± 26 kJ mol^{-1} suggests an electron transfer from Cr^+ to CH_3CN. Exclusively for M = Zn, a relatively slow oxidation of the metal center to Zn^{2+}, with formation of $ZnOH^+$ and release of $CH_3CNH^\bullet$ or $CH_3CHN^\bullet$ is observed. Density functional theory molecular dynamics simulations and geometry optimizations show that charge transfer from Zn^+ to CH_3CN as well as the subsequent proton transfer are associated with a barrier.

3.1. Introduction

Hydrated first row transition metal ions $[M(H_2O)_n]^+$ in the gas phase are valuable model systems for aqueous solutions of transient species. They have been studied in detail over the last two decades with a combination of experiment and theory.[14–19,39,64–71] The +I oxidation state of M in bulk aqueous solutions is rare because disproportionation reactions are energetically favored. In the gas phase, hydrated M(I) can be generated in a laser vaporization[35,37,72] cluster source. Many $[M(H_2O)_n]^+$ cations are stable in the nanoscale aqueous environment of 20–40 water molecules. Disproportionation is not possible in these small systems because only one metal ion is present in the cluster.[3] These conditions allow detailed studies of the reactivity of monovalent transition metals in the aqueous environment. Monovalent metal ions exhibit interesting redox chemistry, for example, the reaction of nitric oxide with $[Fe(H_2O)_n]^+$ or $[Zn(H_2O)_n]^+$ produces the respective oxidized metal(II) monohydroxide ion.[68] A hydrated V(I) shows the oxidation to V(II) or V(III) with elimination of an atomic or a molecular hydrogen, respectively.[26] This reaction is activated by blackbody radiation (BIRD) and is de-

pendent on the cluster size. In the reaction of $[Zn(H_2O)_n]^+$ with gaseous HCl, Zn(I) is oxidized and hydrogen is reduced upon uptake of a second HCl molecule. [25]

The interaction of acetonitrile with metal centers is relevant due to its use as a standard solvent for electrospray ionization. At the same time, CH_3CN is known to exhibit a specific reactivity toward the hydrated electron. Reaction of $(H_2O)_n^-$ with acetonitrile results in the addition of a hydrogen atom to acetonitrile and the generation of $[OH(H_2O)_m]^-$. [73] The possible neutral products, $CH_3CHN^\bullet$ and $CH_3CNH^\bullet$, can be generated transiently [74] and have been studied with ESR in bulk solution. [75] FT-ICR mass spectrometric experiments and DFT quantum chemical calculations have also demonstrated that collisions of CH_3CN with $[Mg(H_2O)]_n^+$ initiate the formation of $[MgOH(H_2O)]^+_{(n-1)}$ by concomitant loss of $CH_3CHN^\bullet$ or $CH_3CNH^\bullet$. [22,76]

Several experimental studies on the solvation and reactions of metal ions in the gas phase are available. The interaction between H_2O and CH_3CN in mixed-solvent clusters $[M(CH_3CN)_n(H_2O)_m]^+$ has been studied by infrared predissociation spectroscopy. These results demonstrate that the ion–dipole interaction weakens the hydrogen bonds. [77] Study of the fragmentation of acetonitrile complexes of divalent metal cations shows solvent evaporation, electron and proton transfer, as well as heterolytic cleavage and charge separation with formation of CH_3^+. [78] Low-energy collision-induced dissociation (CID) of $[M(CH_3CN)_n]^{2+}$ in comparison to pyridine and methanol show that the dissociation pathways are depending on parameters such as ionization potential and coordination type of the ligands. [79] To learn more about electron transfer chemistry of hydrated transition metals, we investigate the interaction of $[M(H_2O)_n]^+$, M = Cr, Mn, Fe, Co, Ni, Cu, and Zn ($n \sim 20$–50) with acetonitrile by Fourier–transform ion cyclotron resonance (FT–ICR) mass spectrometry.

3.2. Experimental Details

All experiments were performed on a modified Bruker/Spectrospin CMS47X FT-ICR mass spectrometer. [21,33,80,81] The instrument is equipped with an unshielded 4.7 T superconducting magnet, Bruker infinity cell, an APEX III data station, TOPPS ion optics power supply, and an ICC2 Infinity Cell Controller with BCH preamplifier. The $[Mg(H_2O)]_n^+$ ions were generated with an external laser vaporization source [35,37,72]

and were transferred by an electrostatic lens system to the ICR cell. The vaporization laser (Nd:YAG laser Continuum Surelite II, operated at 532 nm) and the frequency doubling crystal were heated by 20 laser shots for minimizing the drift of the initial cluster size distribution, followed by 20 laser shots at 10 Hz and typically 5 mJ pulse energy to fill the cell. The reaction delay was measured relative to the end of the fill cycle. Therefore, some reaction products were observed at a nominal 0 s reaction delay. Isotopically enriched targets [39] were used where applicable: ^{52}Cr (99.9%), ^{56}Fe (99.7%), ^{58}Ni (99.9%), ^{63}Cu (99.3%), and ^{64}Zn (99.4%) (STB Isotope Germany GmbH). Acetonitrile (Sigma-Aldrich $\geq$ 99.9%) was introduced into the ultrahigh-vacuum region by a needle valve at a constant pressure in the range from 2 x 10^{-9} to 5 x 10^{-8} mbar. The reactions were monitored by recording mass spectra at different reaction delays. Collision rates were calculated with the average dipole orientation (ADO) theory [82] by using literature values for the dipole moment and polarizability [83] of gaseous acetonitrile. The relative error of the measured absolute rate constants is 25%, which is due to the uncertainty of the pressure measurement in the ICR cell.

The average number of water molecules which are evaporating due to the heat of the reaction released in the cluster were determined with nanocalorimetry [20, 21] as described before. [21] The clusters are continuously heated by the absorption of room temperature blackbody radiation, which results in evaporative cooling, known as blackbody infrared radiative dissociation (BIRD). [21, 42–44, 84] To disentangle the effect of the reaction from BIRD, the average cluster sizes of reactants N_R and products N_P as a function of time are described with a set of differential eqs 3.1 and 3.2. Equation 3.1 and the first term in eq 3.2 account for BIRD, with k_f, $N_{0,R}$, and $N_{0,P}$ describing the size dependence of BIRD. The second term in eq 3.2 describes the change in average cluster size due to the heat released during the bimolecular reaction. ΔN_{vap} is the number of water molecules evaporating on average due to this heat release, k is the pseudo-first-order rate constant of the bimolecular reaction, and I_R and I_P are the summed intensities of reactant and product clusters, respectively. Fit parameters are k_f, $N_{0,R}$, $N_{0,P}$, ΔN_{vap} and the boundary conditions (i.e., the average cluster sizes at t = 0 s).

$$dN_R = -k_f((N_R - N_{0,R})dt \tag{3.1}$$

$$dN_R = -k_f(N_P - N_{0,P})dt + (N_R - \Delta N_{vap} - N_P)(kI_R/I_P)dt \tag{3.2}$$

3.3. Experimental Results

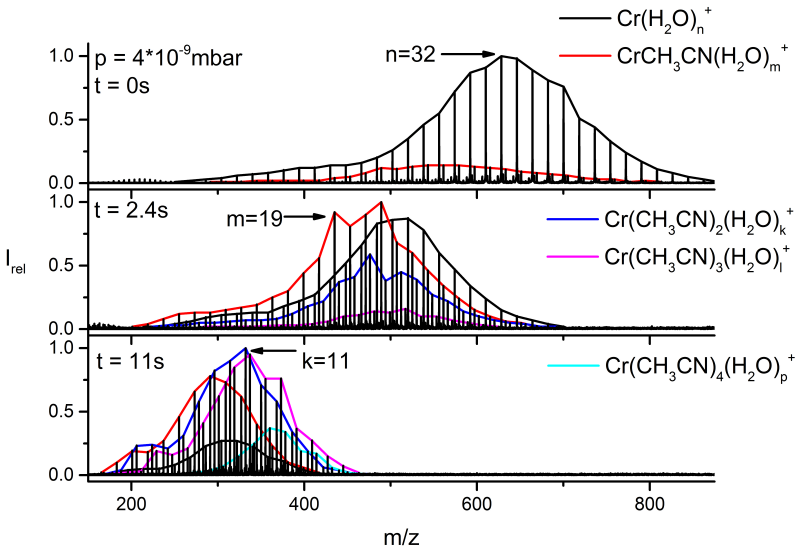

Figure 3.1.: Mass spectra of the reaction of $[Cr(H_2O)_n]^+$ with CH_3CN at a pressure of 4 x 10^{-9} mbar after 0, 2.4, and 11 s. Quantitative formation of $[Cr(CH_3CN)_4(H_2O)_p]^+$ is observed.

Figure 3.1 shows the typical mass spectra of the reaction of $[M(H_2O)_n]^+$ (e.g., M = Cr) with acetonitrile at different delays. The data for other metals are available in supporting information (appendix A.1). All studied hydrated metal ions undergo ligand exchange (eq 3.3).

$$[M(CH_3CN)_p(H_2O)_n]^+ + CH_3CN \longrightarrow [M(CH_3CN)_{p+1}(H_2O)_k]^+ + (n-k)\ H_2O \qquad (3.3)$$

Summing the ion intensity for all n at different reaction delays give the kinetics plot, which is usually pseudo-first-order, as shown in Figure 3.2. The rate constants for all M^+ studied are summarized in Table 3.1.

Assuming that the rate constant of the reaction is independent of cluster size and internal energy of the clusters and the reaction is fully ergodic, thermochemical information can be obtained by determining the average number of water molecules evaporated due to the uptake of acetonitrile with nanocalorimetry. A nanocalorimetric analysis [21] was performed for all studied metals.

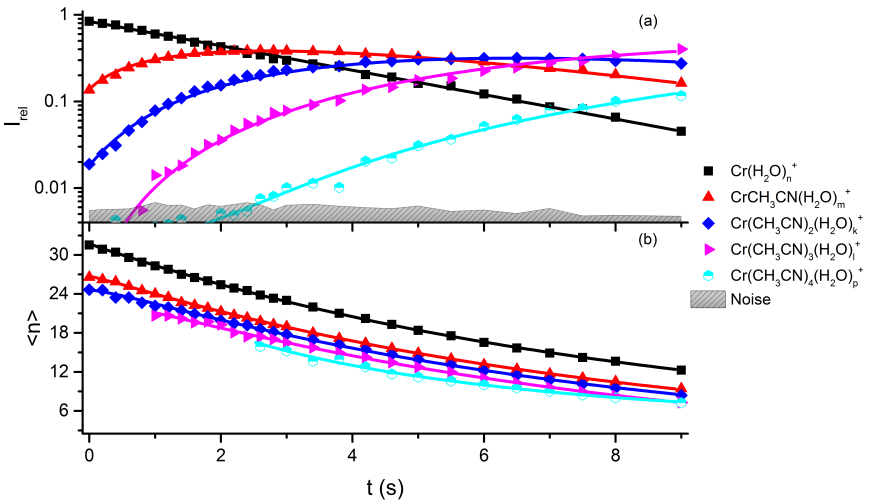

Figure 3.2.: (a) Pseudo-first-order kinetics and (b) average cluster size <n> of the reaction of $[Cr(H_2O)_n]^+$ with CH_3CN at a pressure of 4 x 10^{-9} mbar. The fits agree well with the measured average cluster size of the reaction.

Table 3.1.: Absolute Rate Constants in cm^3 s^{-1} for the reaction of $[M(H_2O)]_n^+$= Cr, Co, Cu, Fe, Mn, Ni with CH_3CN.[α]

[α] k_i refers to the uptake of the ith CH_3CN molecule.

	k_1	k_2	k_3	k_4
$[Cr(H_2O)]_n^+$	$1.7*10^{-9}$	$1.6*10^{-9}$	$1.3*10^{-9}$	$4.4*10^{-10}$
$[Mn(H_2O)]_n^+$	$1.7*10^{-9}$	$1.5*10^{-9}$	$1.1*10^{-9}$	$4.1*10^{-10}$
$[Fe(H_2O)]_n^+$	$1.2*10^{-9}$	$1.0*10^{-9}$	$8.7*10^{-10}$	$4.0*10^{-10}$
$[Co(H_2O)]_n^+$	$1.7*10^{-9}$	$1.5*10^{-9}$	$1.5*10^{-9}$	$1.3*10^{-9}$
$[Ni(H_2O)]_n^+$	$1.7*10^{-9}$	$1.5*10^{-9}$	$1.5*10^{-9}$	$1.1*10^{-9}$
$[Cu(H_2O)]_n^+$	$8.5*10^{-10}$	$7.7*10^{-10}$	$6.1*10^{-10}$	–

Figure 3.2 shows an example for the fits of the average cluster size obtained with a genetic algorithm. The fits were obtained by fitting several data sets simultaneously.

Nanocalorimetry works if the reaction rate is independent from cluster size as well as internal energy content of the clusters. Although the fits for the first uptake step look good, we do not have a direct way to verify whether all these assumptions are fulfilled. The difference fits (see Figures A11-A16 of the Supporting Information) give additional hints for cluster size-dependent reaction rates. ΔN_{vap} is converted to absolute thermochemical values using eq 3.4 for the total energy ΔE_{nc} released in the reaction:

$$\Delta E_{nc} = -\Delta N_{vap} \Delta E_{vap} + \Delta E_{therm} \tag{3.4}$$

Evaporation of one water molecule requires ΔE_{vap} = 43.3 ± 3.1 kJ/mol in this cluster size range. [46,55] ΔE_{therm} = 4.3 ± 0.5 kJ/mol takes the internal energy of the room-temperature reactant molecule and the contribution of the newly formed product ion to the heat capacity of the cluster into account. [21] ΔE_{nc} is thus the change in internal energy during the chemical reaction at the ill-defined temperature of the cluster. The results are summarized in Table 3.2.

Table 3.2.: Nanocalorimetric Analysis of the Reaction of $[M(H_2O)]_n^+$ with CH_3CN.

[α] $\Delta E_{nc,i}$ in kJ mol⁻1 is given for the uptake of the ith acetonitrile molecule. [b] These values are less reliable. [c] Some reactions are strongly size dependent, and no values are given in these cases.

	$\Delta E_{nc,1}$	$\Delta E_{nc,2}$	$\Delta E_{nc,3}$	$\Delta E_{nc,4}$
$[Cr(H_2O)]_n^+$	–195 ± 26	–59 ± 22	–45 ± 22[b]	
$[Mn(H_2O)]_n^+$	0 ± 22[b]			
$[Fe(H_2O)]_n^+$	–27 ± 22			
$[Co(H_2O)]_n^+$	–71 ± 27	–42 ± 26	–52 ± 26[b]	–45 ± 26[b]
$[Ni(H_2O)]_n^+$	–38 ± 31			
$[Cu(H_2O)]_n^+$	–57 ± 26[b]			

Chromium. Sequential uptake of four acetonitrile molecules is observed. For longer reaction delays, the loss of all water molecules is observed, followed by the evaporation

of the fourth acetonitrile molecule. The final product of the reaction is $[Cr(CH_3CN)_3]^+$. At higher pressures of 3 x 10^{-8} mbar, clusters containing up to five acetonitrile molecules are observed, but the final product of the reaction, $[Cr(CH_3CN)_3]^+$, is independent of the acetonitrile pressure. As long as water molecules are present, uptake of CH_3CN may proceed via ligand exchange. As soon as all water molecules have evaporated, however, BIRD leads to a shrinking of the acetonitrile solvent shell, until the cluster at room temperature does not contain sufficient energy for solvent evaporation. This limit is reached at $[Cr(CH_3CN)_3]^+$.

For reaction delays up to 9 s, the kinetics are pseudo-first order.At longer reaction delays loss of the fourth acetonitrile and strong size dependence become evident. The rate constants for the reaction of $[Cr(H_2O)_n]^+$ with CH_3CN decrease monotonically with the number of CH_3CN molecules in the cluster. The uptake of the fourth acetonitrile molecule is about four times slower than that of the first. Reaction of $[Cr(H_2O)_n]^+$ with the first acetonitrile molecule is an exothermic process which leads to evaporation of water molecules from the cluster. The first uptake is heavily exothermic, while values for the second and third uptake are consistent with a simple ligand exchange, in which the incoming acetonitrile molecule replaces one water molecule. The value for the fourth uptake resulting from the fit does not correlate with the overall behavior of the average cluster size. Here the presumably strong cluster size dependence of this uptake leads to unrealistic results in the genetic algorithm fit, and the result had to be discarded.

Manganese. $[Mn(H_2O)_n]^+$, starting with n = 15–40, also show the uptake of four acetonitrile molecules at a reactant pressure of 4 x 10^{-9} mbar. After 16 s, the intensity of $[Mn(CH_3CN)_4]^+$ decreases, because BIRD causes the evaporation of all water molecules and the loss of the fourth acetonitrile molecule.

The final product of the experiment is $[Mn(CH_3CN)_3]^+$.This result is somewhat surprising in view of our earlier study of the reactions of $[Mn(H_2O)_n]^+$ with D_2O. [85] The D_2O exchange experiments showed that $[Mn(H_2O)_n]^+$, $n \leq 20$, undergo an intracluster redox reaction with formation of $[HMnOH(H_2O)_{n-1}]^+$. The complete loss of water in the reaction with acetonitrile indicates that the intracluster reaction leading to $[HMnOH(H_2O)_{n-1}]^+$ is reversible. To test this hypothesis, experiments with a smaller cluster distribution of $[Mn(H_2O)_n]^+$, n = 10–20, were performed at a lower acetonitrile pressure of 8.9 x 10^{-10} mbar to make sure that $[HMnOH(H_2O)_{n-1}]^+$ are formed

by BIRD before the uptake of the first acetonitrile molecule. Also here, complete exchange of water against acetonitrile was observed, providing strong evidence that $[HMnOH(H_2O)_{n-1}(CH_3CN)_m]^+$ rearrange back to $[Mn(H_2O)_n(CH_3CN)_m]^+$. The final validation of this interpretation, however, has to be brought by spectroscopy.

While the uptake of the first molecule is the fastest process, it is basically thermoneutral (table 3.2). One may speculate that during the first uptake, $[HMnOH(H_2O)_{n-1}]^+$ rearranges to $[Mn(H_2O)_n]^+$ in an endothermic process. However, also more complex scenarios involving electron or hydride transfer to acetonitrile are conceivable.

Iron. The uptake of acetonitrile molecules by $[Fe(H_2O)_n]^+$ was studied at a pressure of 6 x 10^{-9} mbar. For the first 7 s, the kinetics exhibits pseudo-first-order behavior (see the Supporting Information). After 25 s, $[Fe(CH_3CN)_4]^+$ lose acetonitrile due to BIRD, resulting in the final product $[Fe(CH_3CN)_3]^+$. Uptake of up to six acetonitrile molecules was observed at a pressure of 4 x 10^{-8} mbar; however, leading to the same final product. The uptake of the first acetonitrile molecule is slower than for the other metal centers, and also slightly less exothermic (see tables 3.1 and 3.2). The curvature of the plot of the average cluster size, figure A7 of the Supporting Information, is pretty unusual for the second uptake product.The first and third uptake behave normal, being largely parallel to the decay of the reactant distribution, caused by BIRD. The second uptake, however, starts close to the third and converges to the first. The difference fit, Figure *S12* of the Supporting Information, also points to a strongly cluster-size-dependent reaction rate. Smaller clusters take up a second acetonitrile molecule more efficiently, therefore this value and all subsequent ones were discarded.

Cobalt. Uptake of up to five acetonitrile molecules is observed with $[Co(H_2O)_n]^+$, n = 15–40, at a pressure of 4 x 10^{-9} mbar. The resulting kinetics, shown in figure A8 of the Supporting Information, is strictly pseudo–first–order. After 8 s,the uptake of the fifth acetonitrile molecule is detected. At longer reaction delays the loss of the fifth and fourth acetonitrile molecule is observed, with $[Co(CH_3CN)_3]^+$ as the final product. The average cluster size of the third product is scattering in the first part due to the low intensity of the peaks. At a higher pressure of 4 x 10^{-8} mbar uptake of up to six acetonitrile molecules is recorded, but the final product is the same as at lower pressure. The reaction enthalpy, see Table 3.2, for the stepwise uptake fits well for a ligand exchange (i.e., uptake of one acetonitrile molecule on average leads to the evaporation of one water molecule).

Nickel. Again up to five molecules CH_3CN are taken up by $[Ni(H_2O)_n]^+$ at 4 x 10^{-9} mbar. The kinetics of the reaction are shown in Figure A9 of the Supporting Information. The reactions are following pseudo–first–order–kinetics. After 12 s, the uptake of the fifth acetonitrile molecule is observed. Only products with more than two acetonitrile molecules and water are detected after 16 s. At longer reaction delays, the intensity of $[Ni(CH_3CN)_4]^+$ and $[Ni(CH_3CN)_5]^+$ is decreasing due to BIRD. The final product of the reaction is $[Ni(CH_3CN)_3]^+$. Walters et al. [86] found by infrared spectroscopy that for $[Ni(H_2O)_n]^+$, $n \leq 3$, all water molecules are coordinated directly to the metal cation. For larger clusters formation of a hydrogen–bonded network begins. The ground state of Ni^+ is ^2D with $3d^9$ configuration, [87] favoring 4–fold coordination in square-planar geometry. Daluz et al. [87] showed that excited state Ni^+ ($3d^84s$, ^2F) interacts less strongly with one water molecule than ground state Ni^+. This suggests that Ni^+ stays in the $3d^9$ configuration for all cluster sizes, with four strongly interacting ligands in the equatorial plane and possibly one or two additional ligands in a Jahn–Teller distorted octahedral arrangement.

Copper. Up to four acetonitrile molecules are taken up by $[Cu(H_2O)_n]^+$ at a pressure of 2 x 10^{-9} mbar. At longer reaction delays, loss of the fourth and third acetonitrile molecule is observed, resulting in $[Cu(CH_3CN)_2]^+$ as the final product. The kinetic plots and the average cluster sizes are shown in Figure A10 of the Supporting Information. The uptake of acetonitrile is slower than for the other metals, see Table 3.1, and less exothermic, see Table 3.2. At higher pressure, 2 x 10^{-8} mbar, the stepwise uptake of seven acetonitrile molecules is observed. However, as for the other metals, the final product is not dependent on the pressure. Magnera et al. [88] determined the binding energies for $[Cu(H_2O)_n]^+$, n = 1–4, with collision-induced dissociation in a triple-quadrupole mass spectrometer and showed that the second water molecule is bound to the copper cation more strongly than the first one, while the third and fourth are significantly more weakly bound than the first two. Bauschlicher et al. [89] performed ab initio calculations and showed that the bonding is enhanced by hybridization of the 4s and 3d orbitals of Cu^+, resulting in a 2–fold linear coordination which is not unusual for Cu(I) complexes, [90] and which is textbook knowledge for coordination complexes of Ag^+. [91] The presence of only two preferred coordination sites in 4s3d hybridized Cu^+ rationalizes the final product $[Cu(CH_3CN)_2]^+$.

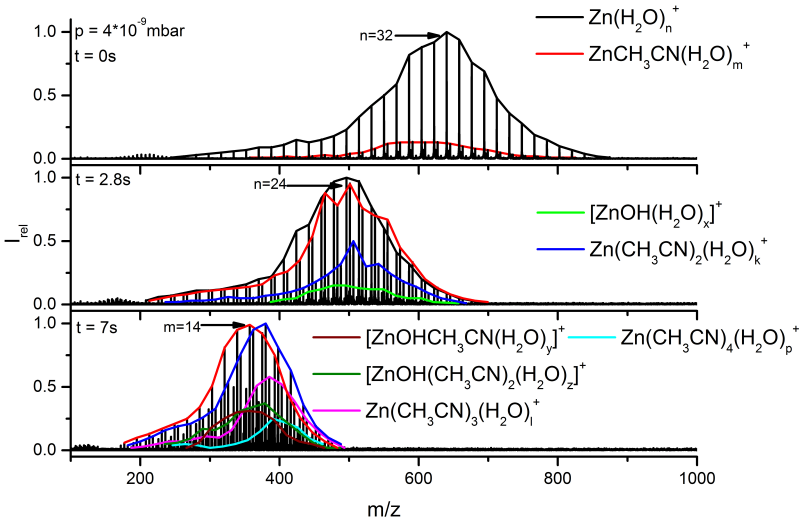

Figure 3.3.: Mass spectra of the reaction of $[Zn(H_2O)_n]^+$ with acetonitrile at a pressure of 4 x 10^{-9} mbar. The uptake of up to four acetonitrile molecules is observed, partly accompanied by loss of a hydrogen atom.

Zinc. Besides ligand exchange, also an oxidation of the metal center is observed with $[Zn(H_2O)_n]^+$ in the reaction with acetonitrile. The mass spectra shown in Figure 3.3 reveal formation of $[ZnOH(CH_3CN)_p(H_2O)_x]^+$, p = 0–4. The formation of $[ZnOH(H_2O)_x]^+$ is observed already at a 0 s reaction delay, according to the kinetics plot and fit (Figure 3.4), as a primary product.

For thermochemical reasons, we assume that the hydrogen atom is not lost on its own but covalently bound to a colliding CH_3CN molecule, as a $[CH_3CN,H]$ unit. The kinetics were fitted, assuming reactions 3.5–3.7

$$[Zn(CH_3CN)_p(H_2O)_n]^+ + CH_3CN \longrightarrow [Zn(CH_3CN)_{p+1}(H_2O)_m]^+ + (n-m)\ H_2O \tag{3.5}$$

$$[Zn(CH_3CN)_p(H_2O)_n]^+ + CH_3CN \longrightarrow [ZnOH(CH_3CN)_p(H_2O)_x]^+ + (n-x-1)\ H_2O + [CH_3CN,H] \tag{3.6}$$

$$[ZnOH(CH_3CN)_p(H_2O)_x]^+ + CH_3CN \longrightarrow [ZnOH(CH_3CN)_{p+1}(H_2O)_y]^+ + (x-y)\ H_2O \tag{3.7}$$

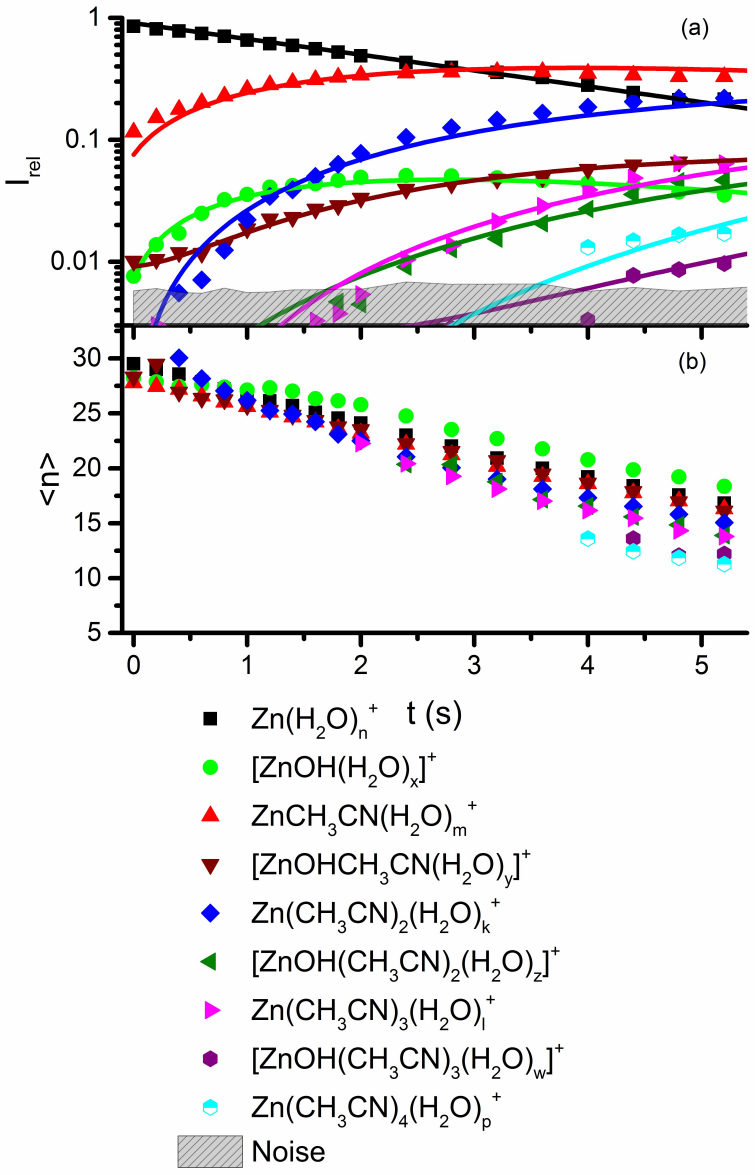

Figure 3.4.: Kinetics and average cluster size <n> for the reaction of $[Zn(H_2O)_n]^+$ with CH_3CN at a pressure of 4 x 10^{-9} mbar. The kinetic exhibit local deviations from pseudo-first-order behavior, probably caused by the strong size dependence of the hydroxide formation reaction, which is evident from the plot of average cluster sizes.

The final product after evaporation of all water molecules is $[ZnOH(CH_3CN)_3]^+$. At 4 x 10^{-8} mbar $[Zn(CH_3CN)_p(H_2O)_n]^+$ are observed with up to p = 6 acetonitrile molecules. However, oxidation products $[ZnOH(CH_3CN)_p(H_2O)_x]^+$ are observed only for $p \leq 4$.

The reaction rate constants, summarized in Table 5.3, show that the uptake of acetonitrile (reactions 3.5 and 3.7) is always more efficient than the oxidation reaction (reaction 3.6). Interestingly, the numbers suggest that $[Zn(CH_3CN)(H_2O)_w]^+$ is most efficiently oxidized in a collision with another acetonitrile molecule (reaction 3.6, p = 1), while $[Zn(CH_3CN)_2(H_2O)_w]^+$ (reaction 3.6, p = 2) is hardly oxidized at all. Due to the competing reactions, however, the fit is very flexible and together with possible size dependences, these numbers again may contain severe pitfalls.

Table 3.3.: Absolute Rate Constants in $cm^3\ s^{-1}$ for the Reaction of $[Zn(H_2O)_n]^+$ with Acetonitrile. Reactions 3.5–3.7

	p = 0	p = 1	p = 2	p = 3
reaction 3.5	$1.3*10^{-9}$	$9.1*10^{-10}$	$8.6*10^{-10}$	$1.1*10^{-9}$
reaction 3.6	$2.4*10^{-10}$	$7.7*10^{-10}$	$3.2*10^{-10}$	$3*10^{-10}$
reaction 3.7	$2.0*10^{-9}$	$1.1*10^{-9}$	$2.1*10^{-10}$	

The size dependence becomes evident in the plot of average cluster sizes (Figure 3.4). The first oxidation product, $[Zn(H_2O)_n]^+$, contains on average more water molecules than the reactant cluster population $[Zn(H_2O)_n]^+$. This is only possible if larger cluster preferentially react via oxidation, while smaller clusters rather undergo ligand exchange. For this reason, however, a quantitative nanocalorimetric analysis is not meaningful, and also the rate constants may be significantly influenced by these effects.

3.4. DFT calculations of the $[Zn(H_2O)_n]^+$ reaction

Small-Sized Model: $[Zn(H_2O)_6]^+$. *Coordination of the Hydrated Zn Complex Ions.* The reaction mechanism and thermodynamics of the reactions 3.5 and 3.6 have been examined using DFT at the M06/6–31++G(d,p) level of theory for a small model $[Zn(H_2O)_6]^+$ using the Gaussian 09 package. [92] Figure 3.5 displays some lowest-energy

structures for three types of complexes, namely $[Zn(H_2O)_6]^+$, $[Zn(H_2O)_6(CH_3CN)]^+$, and $[Zn(OH)(H_2O)_5]^+$, which are categorized as the reactants **(r)**, complexes **(c)**, and products **(p)**, respectively. The number in the labels denotes the coordination number of the Zn center. For the complexes c, an additional alphabet is used to indicate if CH_3CN is coordinated to the first solvation shell **(a)** or outer solvation shells **(b)** of the zinc center. Some structural parameters of the complexes are tabulated in Table S1 of the Supporting Information, and a list of some higher-lying structures is available in Table S2 of the Supporting Information.

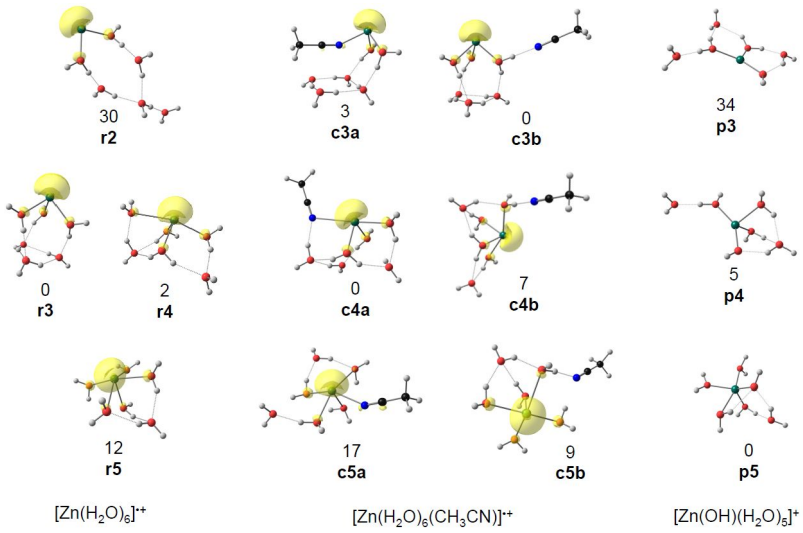

Figure 3.5.: Relative energies ΔH°_0, in kJ mol^{-1}, of the reactants $[Zn(H_2O)_6]^+$ **(r)**, the complexes $[Zn(H_2O)_6(CH_3CN)]^+$ **(c)**, and the oxidized products $[ZnOH(H_2O)_5]^+$ **(p)**, with different coordination numbers. All geometries were optimized at the M06/6–31++G(d,p) level. The spin density distributions (yellow surfaces) are shown with an isovalue of 0.01.

The lowest-energy structure of $[Zn(H_2O)_6]^+$ is **r3**, in which the Zn center is coordinated by three water molecules in its first solvation shell, forming a structure close to C_3 symmetry with the Zn–O_w distances being between 2.14 and 2.16 Å. A quasitetra coordinated structure **r4** can also be located, which is only 2 kJ mol^{-1} higher in energy than **r3**. In this structure, the Zn center forms three short Zn–O_w bonds (2.15–2.25 Å) and one long Zn–O_w bond (2.70 Å). Coordinating one more H_2O to the Zn center further destabilizes the cluster and forms a quasipenta coordinated structure **r5** (12 kJ mol^{-1}), consisting of four Zn–O_w bonds with similar distances (2.19–2.37 Å) and one

with a quite long distance (2.91 Å). No hexa–coordinated structure for $[Zn(H_2O)_6]^+$ was found.

These results suggest that $[Zn(H_2O)_6]^+$ prefers lower coordination geometries. The tri-coordinated structure for $[Zn(H_2O)_4]^+$ was also evidenced by IR action spectroscopy. [65] The smaller bicoordinated structure **r2** (30 kJ mol^{-1}) is the least favorable isomer because the charge of the Zn center is not effectively stabilized by only two water molecules ($Zn–O_w$ = 2.06 Å). In all located structures, the spin density is largely localized on the Zn center with values between 0.89 and 0.93, and the first-shell water molecules are ligated on the opposite side from this unpaired electron.

The energetically preferable tri– and tetra–coordinated structures of $[Zn(H_2O)_6]^+$ are retained when a CH_3CN molecule is added to form the complexes $[Zn(H_2O)_6(CH_3CN)]^+$. The CH_3CN can be added to the first or second solvation shell. These structures include the isoenergetic **c3b** and **c4a** (0 kJ mol^{-1}), **c3a** (3 kJ mol^{-1}), and **c4b** (7 kJ mol^{-1}). All $Zn–O_w$ distances (2.08–2.17 Å) and the Zn– N distance (2.14 Å) in the tricoordinated structures **c3a** and **c3b** are similar. Like **r4**, **c4a** is a quasitetra–coordinated structure with the Zn–N distance (3.01 Å) being significantly longer than the three $Zn–O_w$ distances (2.11–2.25 Å). Similarly, **c4b** also contains two relatively long $Zn–O_w$ bonds (2.38–2.42 Å) compared to the two shorter ones (2.15–2.18 Å). The penta–coordinated structures, **c5a** (17 kJ mol^{-1}) and **c5b** (9 kJ mol^{-1}), are less favorable, again because the spin density is largely localized on the Zn center (0.86–0.92). Therefore, similar to all above high coordinated structures, **c5a** contains a long $Zn–O_w$ bond (2.88 Å) compared to the other three shorter ones (2.22–2.33 Å), and the Zn–N bond (2.37 Å) and **c5b** also contains a long $Zn–O_w$ (2.63 Å) compared to the other four shorter ones (2.21–2.33 Å).

For the oxidized products $[ZnOH(H_2O)_5]^+$, the lowest energy structure is **p5** (0 kJ mol^{-1}) in which the Zn center is penta-coordinated by four water molecules ($Zn–O_w$ = 2.04–2.24 Å) and a hydroxide ion ($Zn–O_{OH}$ = 1.86 Å). The tetra–coordinated structure **p4** (5 kJ mol^{-1}) and the tri–coordinated structure **p3** (34 kJ mol^{-1}) are less favorable because the ionic core contains a higher charged Zn^{2+} center. Therefore, the Zn–ligand distances in the oxidized $[ZnOH(H_2O)_5]^+$ are also in general shorter than those in $[Zn(H_2O)_6]^+$; for instance, the $Zn–O_w$ and $Zn–O_{OH}$ distances are 2.04–2.24 and 1.86 Å for **p5**, 1.99–2.06 and 1.83 Å for **p4**, and 1.91–2.00 and 1.79 Å for **p3**.

These results suggest that the stability of the Zn complexes is strongly affected by its coordination and valence; the tri– or tetra–coordinated structures are preferred for the reactant $[Zn(H_2O)_6]^+$ and the complexes $[Zn(H_2O)_6(CH_3CN)]^+$, while the penta–coordinated structures are preferred for the oxidized products $[ZnOH(H_2O)_5]^+$. Therefore, the reduction of CH_3CN by $[Zn(H_2O)_6]^+$ likely involves a change in coordination structure of the zinc center.

Reactions of $[Zn(H_2O)_6]^+$ with Acetonitrile. Figure 3.6 shows the potential energy surface of the proposed mechanisms for the reaction between $[Zn(H_2O)_6]^+$ and CH_3CN, with the energies given relative to **r3** + CH_3CN.

In general, the overall reactions from the low lying **r3** or **r4** toward CH_3CN, forming the lowest energy product **p5** and different isomers of $[CH_3CN,H]^\bullet$ (including $CH_3CHN^\bullet$, *E*–$CH_3CNH^\bullet$, and *Z*–$CH_3CNH^\bullet$) are endothermic by 20–63 kJ mol^{-1}. These reactions may proceed with a series of electron and proton transfers among various isomers of the $[Zn(H_2O)_6(CH_3CN)]^+$ complexes. Transition structures were optimized based on initial geometries located approximately at local maxima obtained from PES scans along the reaction coordinates. All geometries at local minima or maxima were confirmed with zero or one imaginary frequency, respectively.

Binding of CH_3CN to the first solvation shell of Zn in the lowest energy tricoordinated **r3** can form the tetra–coordinated **c4a** (–61 kJ mol^{-1}). Then, CH_3CN can be reduced by Zn^+ via the transition structure **c4a-n-ts1** (–45 kJ mol^{-1}), in which the unpaired electron has partially transferred from the Zn center into the π^* orbital of CH_3CN with its CCN angle bent from linear to 153°. Further electron transfer and bending of the CCN angle to 143° yields $CH_3CN^{\bullet-}$ that is directly coordinated to the resulting Zn^{2+} through its nitrogen atom, giving the metastable intermediate **c4a-n** (–44 kJ mol^{-1}). The CCN angle in this structure is still significantly greater than that in the isolated $CH_3CN^{\bullet-}$ (130°), [76, 93] suggesting that the $CH_3CN^{\bullet-}$ in **c4a-n** is still not completely reduced, probably because there are not enough water molecules in this small cluster to fully stabilize $CH_3CN^{\bullet-}$ and Zn^{2+} at the same time. The Zn–N distance of 1.96 Å in **c4a-n** is significantly shorter than that in clusters with nonreduced CH_3CN. Subsequent proton transfer either to the carbon or nitrogen atom of the $CN^{\bullet-}$ moiety via the transition structures **c4a-n-ts2** (–19 kJ mol^{-1}) or **c4a-n-ts3** (–7 kJ mol^{-1}) can produce **c4a-n-ch** (–56 kJ mol^{-1}) or **c4a-n-nh(*E*)** (–37 kJ mol^{-1}), respectively. This proton transfer

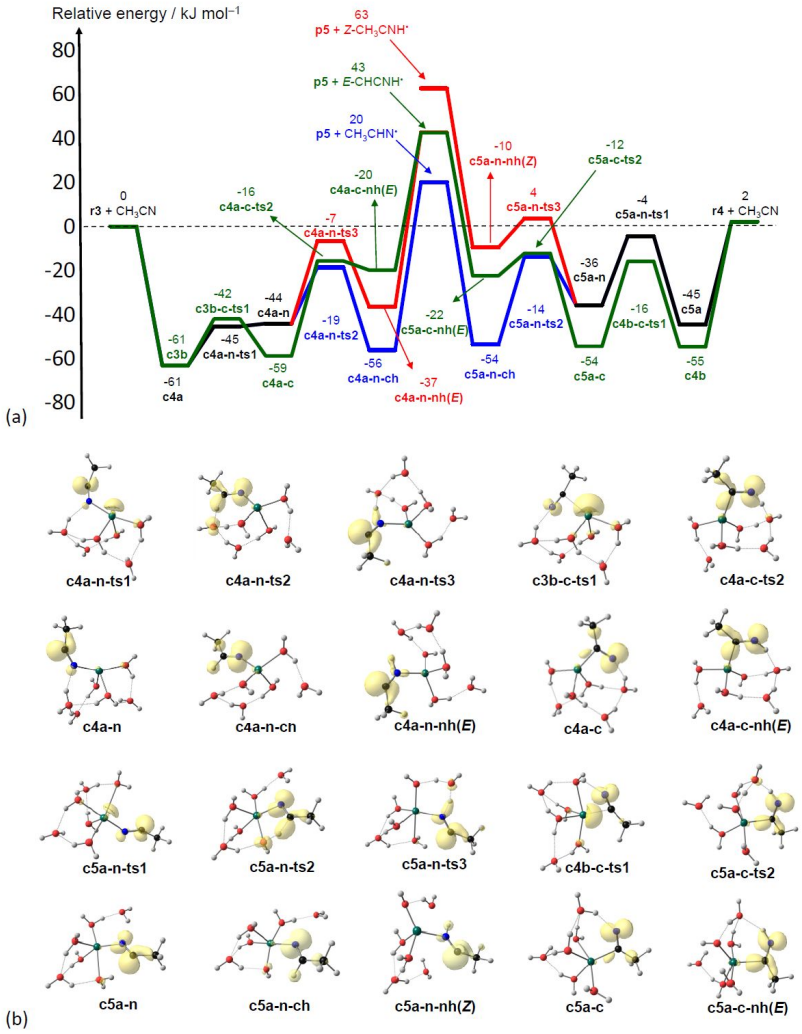

Figure 3.6.: (a) Potential energy surface for the reaction of $[Zn(H_2O)_6]^+ + CH_3CN \rightarrow [ZnOH(H_2O)_5]^+ + [CH_3CN,H]^\bullet$. (b) Optimized geometries of $[Zn,CH_3CN,(H_2O)_6]^+$. All geometry optimizations and relative energies ΔH°_0, in kJ mol^{-1}, were obtained at the M06/6–31++G(d,p) level.

further stabilizes the reduced $CH_3CN^{\bullet-}$,forming CH3CHN$^\bullet$ or *E*-$CH_3CNH^\bullet$, indicated by their smaller CCN angles (126° and 134°, respectively). The Zn–N interactions in these structures are also weaker and their distances are also increased to 2.01 and 2.03 Å, respectively.

Alternatively, CH_3CN can also bind to the second solvation shell of Zn in **r3** to give **c3b** (–61 kJ mol^{-1}). Electron transfer can also occur when the CN moiety of this second shell CH_3CN is approaching to Zn^+ via the transition structure **c3bc-ts1** (–42 kJ mol^{-1}). In the resulting structure **c4a-c** (–59 kJ mol^{-1}), $CH_3CN^{\bullet-}$ binds to Zn^{2+} through the carbon atom of its $CN^{\bullet-}$ moiety (Zn–C = 2.02 Å). The CCN angle in **c4a-c** of 131° was smaller than that in **c4a-n**, suggesting that $CH_3CN^{\bullet-}$ is better stabilized through the Zn–C coordination in this small cluster, also consistent with the fact that **c4a-c** is lower-lying than **c4a-n**. A proton transfer to the nitrogen atom in **c4a-c** via **c4a-c-ts2** (–16 kJ mol^{-1}) gives **c4a-c-nh(*E*)** (–20 kJ mol^{-1}). The Zn–C interaction in this structure is also weaker with its distance increased to 2.13 Å.

A similar mechanism is possible starting from the higher coordinated **r4**. Binding of CH_3CN to the first or second shell of Zn^+ in **r4** gives **c5a** (–45 kJ mol^{-1}) or **c4b** (–55 kJ mol^{-1}). An electron transfer via **c5a-n-ts1** (–4 kJ mol^{-1}) or **c4b-c-ts1** (–16 kJ mol^{-1}) results in **c5a-n** (–36 kJ mol^{-1}) or **c5a-c** (–54 kJ mol^{-1}). The respective Zn–N and Zn–C distances are 1.92 and 2.03 Å. For **c5a-n**, a proton transfer to the carbon or nitrogen atom of its $CN^{\bullet-}$ moiety via **c5a-n-ts2** (–14 kJ mol^{-1}) or **c5a-n-ts3** (4 kJ mol^{-1}) can produce **c5a-n-ch** (–54 kJ mol^{-1}) or **c5a-n-nh(*Z*)** (–10 kJ mol^{-1}), respectively. For **c5a-c**, a proton transfer to the nitrogen atom via **c5a-c-ts2** (–12 kJ mol^{-1}) gives **c5a-c-nh(*E*)** (–22 kJ mol^{-1}). The CCN angle of $CH_3CN^{\bullet-}$ in the Zn–N coordinated **c5a-n** (133°) is larger than that in the Zn–C coordinated **c5a-c** (130°), also suggesting that $CH_3CN^{\bullet-}$ is better stabilized by the Zn–C coordination rather than the Zn–N coordination in this small cluster.

In all structures as shown in Figure 3.6, the reduced $CH_3CN^{\bullet-}$ and $[CH_3CN,H]^\bullet$ are produced in the first solvation shell of Zn. Reduction of CH_3CN in **c4b** and **c5b** with the reduced $CH_3CN^{\bullet-}$ remaining in the second solvation shell has also been examined by scanning its CCN angle. In these simulations, the energy was monotonically increasing with decreasing CCN angle, and no electron transfer to the π^* orbital of CN was observed. Instead, the spin density was always mainly localized on the zinc center.

Medium–Sized Model: $[Zn(H_2O)_{16}]^+$. *Coordination of the Hydrated Zn Complex Ions.* Multiple uptakes of CH_3CN by $[Zn(H_2O)_n]^+$ were observed in the mass spectrometric studies. This result is in contrast to the observations for the analog system $[Mg(H_2O)_n]^+$, for which $[Mg(H_2O)_n(CH_3CN)_p]^+$ was not observed. It is probably because the subsequent reduction of CH_3CN in the initially formed $[Mg(H_2O)_n(CH_3CN)_p]^+$ was highly efficient and formed $[CH_3CN,H]^\bullet$ that was liberated from the cluster rapidly. Therefore, only the oxidized products $[MgOH(H_2O)_{n-1}]^+$ were observed. The present mechanistic studies for the small–sized model $[Zn(H_2O)_6]^+$ also support that the reaction of $[Zn(H_2O)_6]^+$ is energetically less favorable than that of $[Mg(H_2O)_6]^+$. [22]

For $[Zn(H_2O)_n]^+$, $[Zn(H_2O)_nCN_3CN]^+$ ions were still predominant up to a reaction delay of 7 s. To further understand the relatively low reactivity of Zn^+ with CH_3CN as compared with the case of Mg^+, the solvation structures and the reaction thermodynamics of a medium–sized cluster $[Zn(H_2O)_{16}]^+$ were examined. An initial geometry of $[Zn(H_2O)_{16}]^+$ was first generated based on the previously well equilibrated $[Mg(H_2O)_{16}]^+$ geometry at 300 K, [94,95] with the Mg ion replaced by a Zn ion. Then, the masses of all hydrogen and oxygen atoms in $[Zn(H_2O)_{16}]^+$ were modified to 2 atomic mass units (amu) so that all water molecules were 3 times lighter than their nominal mass in order to speed up the reorganization of the solvation structures about the Zn center during MD simulations. A DFT–MD annealing simulation was performed for this mass–modified $[Zn(H_2O)_{16}]^+$, with the temperature gradually changed from 300 to 100 K in 5 ps. Then, the mass of all water molecules was switched back to the nominal value (i.e., 18 amu). An additional 5 ps equilibration MD at a constant temperature of 300 K controlled by a Nosè thermoset was run. The above annealing and equilibration procedures were repeated for 9 times. For each equilibration trajectory, ten geometries with an interval of 0.5 ps were selected and optimized at the M06/6–31++G(d,p) level. These hundred optimized geometries were summarized as Table S3 of the Supporting Information. All DFT–MD simulations were performed by the VASP program [96] at the PBE level with a planewave basis set (Ecutoff = 283 eV). [94] All geometry optimizations and spin–density calculations were performed using the Gaussian 09 package. [92]

Among all optimized geometries for the reactant clusters $[Zn(H_2O)_{16}]^+$, the Zn center is either tri– or tetra–coordinated and can be solvated in the interior or on the surface of the cluster. Figure 3.7a shows the lowest lying structure each for these types. The Zn center of the lowest–energy geometry is tetra–coordinated and interior-solvated (**R4i**)

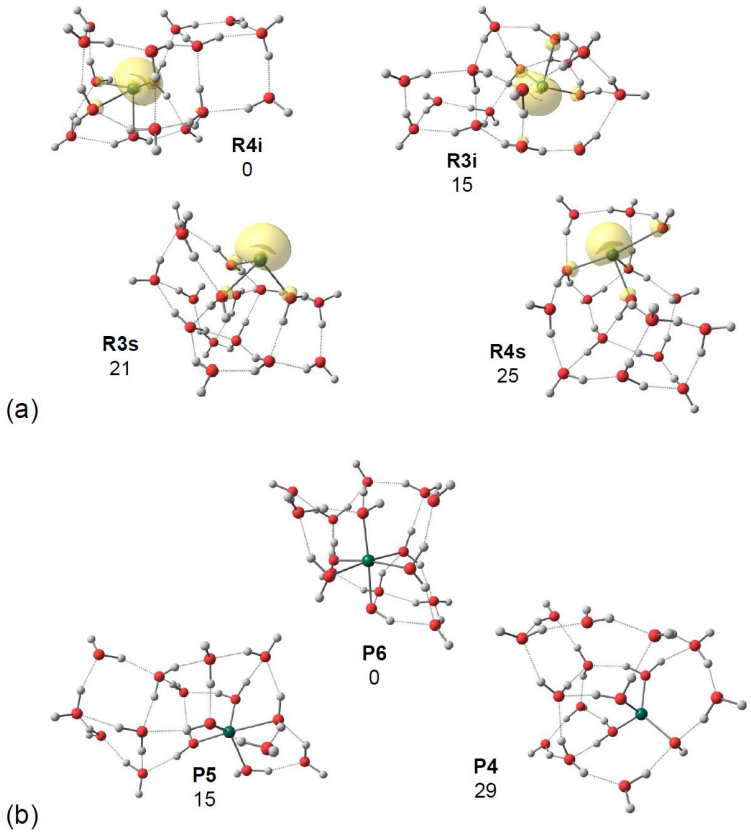

Figure 3.7.: Optimized geometries for (a) the reactant $[Zn(H_2O)_{16}]^+$ and (b) the oxidized products $[ZnOH(H_2O)_{15}]^+$. All geometry optimizations and relative energies ΔH°_0, in kJ mol^{-1}, were evaluated at the M06/6–31++G(d,p) level. The spin-density distributions (yellow surfaces) are shown with an isovalue of 0.01.

(0 kJ mol^{-1}). The four Zn–O_w bonds are within 2.15–2.37 Å. Similar to the small $[Zn(H_2O)_6]^+$, the unpaired electron is largely localized on the Zn center with a spin density of 0.87. This electron is enclosed by the water molecules. For **R3i** (15 kJ mol^{-1}), the Zn center is also interior–solvated but tricoordinated with the three Zn–O_w bonds within 2.10–2.20 Å. For **R3s** (21 kJ mol^{-1}) and **R4s** (25 kJ mol^{-1}), the Zn center is surface–solvated with its spin density pointing away from the cluster. The Zn–O_w bonds are within 2.06–2.21 Å for **R3s** and 2.11–2.45 Å for **R4s**.

Some lowest-energy structures for the oxidized products $[ZnOH(H_2O)_{15}]^+$ are shown in Figure 3.7b. Similar to the oxidized products for the smaller clusters **(p)**, the Zn^{2+} center is preferred to have a higher coordination. The lowest–energy structure is **P6**, in which Zn^{2+} is hexa–coordinated by five H_2O molecules (Zn–O_w = 2.10–2.33 Å) and one OH^- (Zn–O_{OH} = 1.96 Å). Comparing to the small cluster of n = 6, this larger cluster can better stabilize the hexa-coordinated structure. The penta-coordinated (**P5**) and tetra-coordinated (**P4**) structures are higher lying by 15 and 29 kJ mol^{-1}, respectively. It is expected that the ligands are attracted tighter to Zn^{2+} in these lower–coordinated structures **P5** (Zn–O_w = 2.01–2.24 Å; Zn–O_{OH} = 1.90 Å) and **P4** (Zn–O_w = 1.98–2.01 Å; Zn–O_{OH} = 1.88 Å).

Reactions of $[Zn(H_2O)_{16}]^+$ with Acetonitrile. Adding CH_3CN to the second solvation shell of **R4i** is exothermic, producing **C4b** with a relative energy of –53 kJ mol^{-1}. This second–shell CH_3CN did not alter the solvation structure of Zn; the four Zn–O bond distances in **C4b** (2.14–2.35 Å) remain similar to those in **R4i**. Migrating CH_3CN closer to the Zn center gives **C5a** (–48 kJ mol^{-1}), in which the first solvation shell contained three short Zn–O bonds (2.20–2.27 Å), one long Zn–O bond (2.62 Å), and one long Zn–N bond (2.87 Å). It is reasonable that one Zn–O is significantly elongated when a bulky CH_3CN is penetrated into the first solvation shell of Zn which is interior–solvated. **C6a-n** (–49 kJ mol^{-1}) and **C6a-c** (–40 kJ mol^{-1}) are the electron–transfer products in which the reduced $CH_3CN^{\bullet-}$ is coordinated to Zn^{2+} via its nitrogen and carbon atoms, respectively. In this larger cluster of n = 16, the Zn–N–coordinated structure (**C6an**) is stronger than the Zn–C–coordinated structure (**C6a-c**) when the Zn center has higher coordination. A proton transfer to the carbon atom and nitrogen atom of $CH_3CN^{\bullet-}$ in these structures yield **C6a-n-ch** (–69 kJ mol^{-1}), the lowest–energy isomer in Figure 3.8, and **C6a-c-nh(*E*)** (–43 kJ mol^{-1}). Liberation of $CH_3CHN^{\bullet}$ or *E*-$CH_3CNH^{\bullet}$ initially generates a penta–coordinated $[ZnOH(H_2O)_{15}]^+$. Similarly, uptake

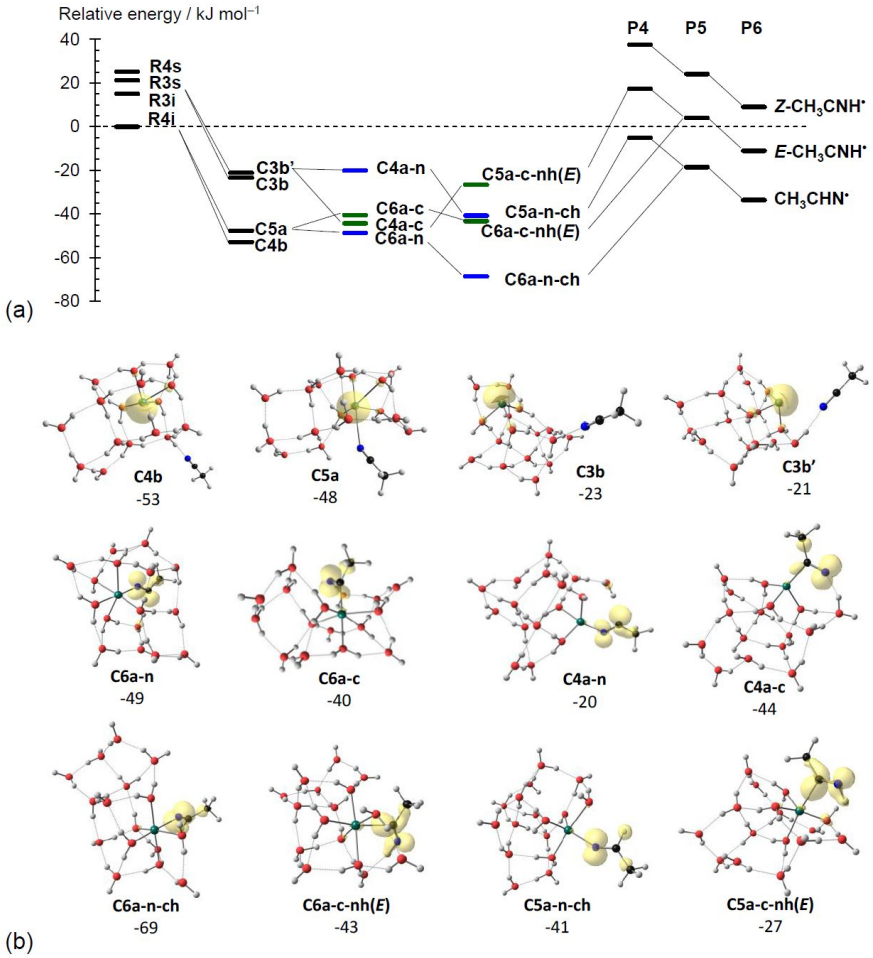

Figure 3.8.: (a) Potential energy surface for the reaction of $[Zn(H_2O)_{16}]^+ + CH_3CN \rightarrow [ZnOH(H_2O)_{15}]^+ + [CH_3CN,H]^\bullet$. (b) Optimized geometries of $[Zn,CH_3CN,(H_2O)_{16}]^+$. Energies ΔH°_0, in kJ mol^{-1}, are relative to the energies of **R4i** + CH_3CN.All calculations were performed at the M06/6–31++G(d,p) level. The spin-density distributions (yellow surfaces) are shown with an isovalue 0.01.

of CH_3CN by the surface solvated structure **R3s** can give the tricoordinated complexes **C3b** (–23 kJ mol^{-1}) and **C3b'** (–21 kJ mol^{-1}). Comparing these two geometries,the CH_3CN in **C3b'** is closer to the Zn center with a Zn–N distance of 3.27 Å. Subsequent electron transfer yields **C4a-n** (–20 kJ mol^{-1}) and **C4a-c** (–44 kJ mol^{-1}), in which the nitrogen and carbons atoms of $CH_3CN^{\bullet-}$ are coordinated to Zn^{2+}, respectively, with a Zn–N distance of 1.87 Å and a Zn–C distance of 2.02 Å. Similar to the smaller clusters **c5a-n** and **c5a-c**, the Zn center in **C4a-n** and **C4a-c** is less coordinated and closer to the surface of the cluster and in both these two sizes, the Zn–N binding is less favorable than the Zn–C binding. Further proton transfer produces **C5a-n-ch** (–41 kJ mol^{-1}) and **C5a-c-nh(*E*)** (–27 kJ mol^{-1}), respectively. The Zn–N and Zn–C distances are also elongated to 2.05 and 2.44 Å. Liberation of $CH_3CHN^{\bullet}$ or *E*-$CH_3CNH^{\bullet}$ initially generates a tetra-coordinated $[ZnOH(H_2O)_{15}]^+$.

3.5. Discussion

Meyerstein and Mulack derived an order of reactivity $Zn^+ \sim Co^+ \geq Cd^+ \geq Ni^+$ from studying reactions with good electron acceptors using pulse radiolysis. [97,98] They attributed the different reactivity to the electronic structure of the monovalent metals. [97,98] Whereas in Zn^+, the additional electron is located in an s orbital, in Ni^+, it is located in the 3d shell. [97,98] In the present study, Zn^+, Co^+, and Ni^+ react with very similar total rates. However, as the quantum chemical calculations show, electron transfer is taking place only after the uptake, so this disagreement simply reflects the fact that the uptake of CH_3CN does not require electron transfer.

In comparison to our previous study of the same hydrated metal ions with O_2, N_2O, and CO_2, [39] as well as NO, [68] we can draw some parallels but also note differences. The obvious difference between previously studied reactants and acetonitrile is the ability of the latter to participate in the hydrogen-bonded network of the hydration shell. [99] This explains why CH_3CN in collisions with a water cluster has a long residence time in the cluster, leading to overall higher reactivity than with the previously studied small and less polar molecules. Its high dipole moment of 3.92 D, compared to 1.85 D for H2O, makes it a stronger ligand than water, explaining why in the late stages of the reaction, water evaporates preferentially, while acetonitrile ligands stay coordinated to

the metal center. Consequently, all studied hydrated metal ions react with acetonitrile. The higher volatility of acetonitrile compared to water, on the other hand, is the reason why the uptake is limited to a small number. Although in the kinetic models only the uptake of CH_3CN was considered, it is likely that when the maximum number is reached, loss of CH_3CN may start competing with loss of H_2O during BIRD. This assumption is consistent with the increased number of CH_3CN molecules taken up at elevated reactant pressures.

While all studied $[M(H_2O)_n]^+$ are reactive against acetonitrile, only $[Co(H_2O)_n]^+$ was reacting with N_2O, although no obvious explanation for this behavior is at hand. The reaction with CO_2 is very slow and occurred only at a pressure in the 10^{-7} mbar range for $[Cr(H_2O)_n]^+$ and $[Co(H_2O)_n]^+$. O_2 was taken up by $[M(H_2O)_n]^+$, M = Cr, Co, Ni, Zn. Looking for correlations with the CH_3CN results, we can state that the two metal centers with the lowest reactivity in the present study, Cu^+ and Fe^+, also showed no reactivity against O_2, CO_2, or N_2O. The hydrated chromium species, on the other hand, exhibit a pronouncedly exothermic uptake of CH_3CN, in parallel to the exothermicity of the O_2 uptake and the high reactivity with CO_2 and NO. On the precise reason for this behavior we can only speculate, lacking further information even on the electronic state of the metal center in $[Cr(H_2O)_n]^+$. However, a picture emerges that $[Cr(H_2O)_n]^+$ shows enhanced reactivity with molecules which can act as electron acceptors. At the same time, $[Cr(H_2O)_n]^+$ seems to be reluctant with respect to hydroxide formation, which might explain its inertness toward N_2O.

Exchange experiments with D_2O together with BIRD experiments for the same metals showed that only $[Mn(H_2O)_n]^+$ undergoes an intracluster redox reaction to form $[HMnOH(H_2O)_{n-1}]^+$ for $n \leq 20$.[85] In the present study, however, complete loss of water molecules is observed, suggesting that the uptake of CH_3CN reverses the intracluster reaction. This illustrates a potential way to prevent corrosion.

Bauschlicher et al. calculated the binding energies and structures for $[Fe(H_2O)_{1-4}]^+$ using density functional theory.[71,100,101] Accordingly, the coordination of two ligands becomes favorable for $[Fe(H_2O)_2]^+$ because the metal–ligand repulsion is minimized by sd_σ hybridization, the lowest quartet state, is linear. The sd_σ hybridization is less efficient for three waters. Ohashi et al.[102] observed for $[Fe(H_2O)_{3-8}]^+$ a linearly coordinated $[Fe(H_2O)_2]^+$ core surrounded by water molecules. This peculiar structural feature of

hydrated Fe(I) may be responsible for the unusual size–dependence evident from the average cluster size plot upon uptake of the second acetonitrile molecule. The Fe^+ center is directly accessible if only two water molecules coordinate directly. However, at the latest when two acetonitrile molecules are coordinated to Fe^+, the linear 2–fold coordination will break down because the hydrophobic methyl groups of CH_3CN are not suitable as anchoring points of a hydrogen-bonded network.

Only Zn^+ is showing the formation of hydrogen. In contrast to the reaction with nitric oxide, [68] where the first event is the uptake of NO, the oxidation products are formed through collisions with acetonitrile. Our previous investigation of the interaction of $[Mg(H_2O)_n]^+$ with CH_3CN and quantum chemical calculations [76] revealed the formation of magnesium hydroxide by concomitant loss of $CH_3CHN^\bullet$ or $CH_3CNH^\bullet$. Similar to the magnesium study, here electron transfer followed by proton transfer leads to formation of $CH_3CHN^\bullet$ or $CH_3CNH^\bullet$ and oxidation of Zn^+ to $ZnOH^+$. In contrast to the magnesium case, however, the first uptake of acetonitrile does not inevitably lead to hydroxide formation. Instead, uptake of CH_3CN and hydroxide formation compete, and any $[Zn(CH_3CN)_m(H_2O)_n]^+$ intermediate may undergo hydroxide formation upon collision with CH_3CN, or through an intracluster rearrangement.

Previous study of the reactions of acetonitrile with hydrated electrons $[(H_2O)_n]^-$, n = 25–60, showed that the hydrated electron induces the transfer of an H atom from water to acetonitrile by formation of $[OH(H_2O)n]^-$. [73] Wang et al. [103] studied the potential energy surface of the hydrogen addition of CH_3CN + H at the G3 level of theory. [103] They showed that among the 11 different possibilities they investigated, the product of hydrogen addition at the carbon atom is the thermochemically most favorable product. Formation of $[ZnOH(H_2O)_n]^+$ and $CH_3CHN^\bullet$ or $CH_3CNH^\bullet$ is in line with these previous studies.

A reduced reactivity of $[Zn(H_2O)_n]^+$ compared to $[Mg(H_2O)_n]^+$ was previously observed with HCl, [25] as well as with CO_2 and O_2. [39] The DFT calculations show that for both the small– and medium–sized models (n = 6 and 16), the spin density in $[Zn(H_2O)_n]^+$ is still largely localized on the Zn center. Reduction of CH_3CN is favorable only when it is directly coordinated to the first solvation shell of Zn. After the electron-transfer process to produce $CH_3CN^{\bullet-}$, the coordination number of the Zn center will increase in order to better stabilize the higher charged Zn^{2+}. Proton transfers to $CH_3CN^{\bullet-}$ can then

happen to give the $ZnOH^+$ ionic core and the neutral products $[CH_3CN,H]^\bullet$ (including $CH_3CHN^\bullet$, *E*-$CH_3CNH^\bullet$, or *Z*-$CH_3CNH^\bullet$). These reduced neutral products are less tightly bound to $ZnOH^+$, as compared with the binding between $CH_3CN^{\bullet-}$ and Zn^{2+}. Evaporation of these $[CH_3CN,H]^\bullet$ produced $[ZnOH(H_2O)_n]^+$. For n = 6, the overall reaction is highly endothermic by 20–63 kJ mol^{-1}, compared with the exothermicity of 16–63 kJ mol^{-1} for the reaction of $[Mg(H_2O)_6]^+$ with CH_3CN. [76] For n = 16, the reaction is almost thermal neutral for Zn^+, while highly exothermic by 96– 145 kJ mol^{-1} for Mg^+. [76] It is in agreement with the experiments that the reaction is feasible but relatively slow as compared with the analog reaction between $[Mg(H_2O)_n]^+$ and CH_3CN.

3.6. Conclusion

All studied $[M(H_2O)_n]^+$ exchange water against several acetonitrile molecules. Acetonitrile is a stronger ligand than water, therefore, water molecules evaporate preferentially via BIRD, and metal ions solvated only with acetonitrile are observed in the late stages of the reaction. The number of acetonitrile molecules taken up by the clusters is, however, limited and depends on the reactant gas pressure, indicating that a stationary state between acetonitrile uptake and evaporation is established around 4–6 acetonitrile molecules in the clusters, depending on the metal and the reactant gas pressure. Uptake of the first acetonitrile molecule by $[Cr(H_2O)_n]^+$ is unusually exothermic, suggesting electron transfer from Cr^+ to acetonitrile. With $[Zn(H_2O)_n]^+$, formation of $[ZnOH(CH_3CN)_m(H_2O)_n]^+$ is observed. This reaction proceeds considerably more slowly than the previously studied reaction of $[Mg(H_2O)_n]^+$ with CH_3CN, a reactivity trend observed before in reactions with HCl, CO_2, and O_2. Quantum chemical calculations corroborate that the reaction proceeds via electron transfer from Zn^+ to CH_3CN, followed by proton transfer from a water molecule in the first solvation shell of Zn^{2+} to $CH_3CN^{\bullet-}$.

Supporting Information

Figures with mass spectra, kinetics and average cluster size and difference in average cluster size for M = Mn, Fe, Co, Ni, Cu. Tables with structural parameters, relative energies, and free energies of selected calculated structures. Full Cartesian coordinates, harmonic frequencies, and energies of all calculated structures. The Supporting Information is available free of charge on the ACS Publications website at
DOI: 10.1021/acs.jpca.5b02946.

Acknowledgements

I.H. and M.K.B. thank the Deutsche Forschungsgemeinschaft for financial support, Grant BE2505/4–3. Financial support from Research Grants Council , HKSAR (Grant CityU_ 102911) and City University of Hong Kong (CityU) (Grant 7004211) is also acknowledged by W.K.T., T.W.L, and C.K.S. H.Y.W. also thanks the Student Exchange Fund from CityU to support his overseas BSc Final-Year Project.

4. Reactivity of hydrated monovalent first row transition metal ions $[M(H_2O)_n]^+$, M = V, Cr, Mn, Fe, Co, Ni, Cu and Zn, n $\leq$ 40, towards iodopropane

4.1. Introduction

Catalytic processes were examined with bare metal ions in the gas phase. [9,10] With guided ion beam technique Fisher et al. [104] studied the reaction of Co^+ and Ni^+ with methyl halides in the gas phase and observed the formation of $[MCH_3^+]$ and $[MX^+]$. However, Allison and Ridge [24] showed for Fe^+, Co^+ and Ni^+ metal insertion into the X-C bond and dehydrogenation of alkyl halides and alkohols with a β-hydrogen in the gas phase. Also the insertion of the metal ion (Fe^+, Co^+ and Ni^+) into the C-C bond of linear alkanes were investigate by Jacobson et al. [23] with collision induced dissociation. They observed the formation of olefines. Overall, the trans metal cations with 3d and 4d occupation cannot activate the C-H bonds of methane at thermal energies, while several 5d metal cations are able to form the metal-carbene cations. [9]

In addition alkyl halides show an interesting chemistry in the gas phase. For example Miller and Gross [105] studied the reaction of benzene radical cations with 2-iodoalkanes with tandem mass spectrometry. They observed the formation of isobutylbenzene or isobutylated benzene. Furthermore the addition of 2-iodopropane to the $[M\text{-}H]^+$ ion of pyrene, whereon fragmentation by the loss of $I^\bullet$ or $CH_3^\bullet$ follows, were observed. [106]

To learn more about the reaction of the transition metal cations with alkyl halides in aqueous environment and the electron transfer between metal ion and organic compounds, reactions for the interaction of $[M(H_2O)_n]^+$, M = V, Cr, Mn, Fe, Co, Ni, Cu and Zn ($n \leq 40$), with C_3H_7I by Fourier-transform ion cyclotron resonance (FT-ICR) mass spectrometry were performed.

4.2. Experimental Results

Vanadium. $[V(H_2O)_n]^+$, starting with n= 20 – 40, is unreactive towards iodopropane. The measurements were done in the pressure range of 3 x 10^{-8} until 2 x 10^{-7} mbar and no reaction was observed. The published reaction [26] with infrared photons was already observed for clusters with $n \leq 20$. The loss of atomic and molecular hydrogen followed by the oxidation and formation of $[V(II)OH(H_2O)_m]^+$ and $[V(III)(OH)_2(H_2O)_l]^+$ is determined. Both reactions are strongly dependent on the cluster size. However, no

further reaction is observed with the oxidation products except shrinking of the cluster distribution through absorbed blackbody radiation, followed by evaporative cooling, a process called blackbody infrared radiative dissociation (BIRD). [21, 42–44] Hydrated monovalent vanadium ions show low reactivity towards other substances. Even with small molecules like NO [68] no reaction and with NO_2, O_2 and CO_2 [39] reactions with very low reactivity have been observed in our working group.

Chromium. Hydrated monovalent $[Cr(H_2O)_n]^+$, n= 20 – 45, cations react with C_3H_7I by formation of $[CrI(H_2O)_m]^+$ due to the oxidation of the metal center. The mass spectra, shown in Figure 4.1 at a pressure of 5 x 10^{-9} mbar, reveal formation of $[CrI(H_2O)_m]^+$ at nominally 0 s reaction delay.

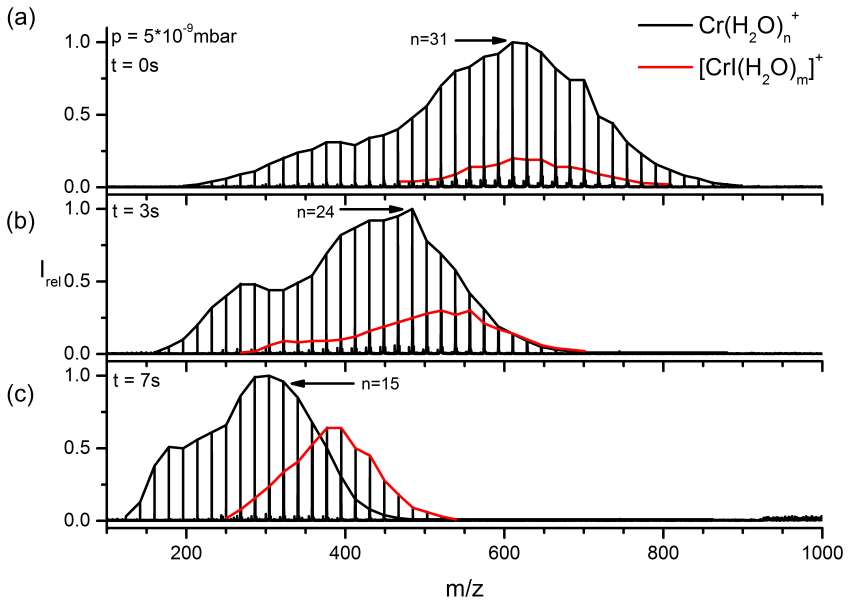

Figure 4.1.: Mass spectra of the reaction of $[Cr(H_2O)_n]^+$ with C_3H_7I at a pressure of 5 x 10^{-9} mbar after 0 (a), 3 (b) and 7 (c) s. Oxidation of Cr^+ is observed.

For the first 18 s the formation of iodide is noticed, according to the equation below:

$$[Cr(H_2O)_n]^+ + C_3H_7I \rightarrow [CrI(H_2O)_m]^+ + C_3H_7^{\bullet} + (n-m)\ H_2O \qquad (4.1)$$

Furthermore weak ligand exchange is observed at 30 s

$$[Cr(H_2O)_n]^+ + C_3H_7I \rightarrow [CrC_3H_7I(H_2O)_l]^+ + (n-l)\ H_2O\ ;\ l \leq 2 \qquad (4.2)$$

Also the ligand exchange of iodopropane for the primary product $[CrI(H_2O)_m]^+$ is observed at 20 s reaction delay:

$$[CrI(H_2O)_m]^+ + C_3H_7I \rightarrow [CrIC_3H_7I(H_2O)_k]^+ + (m-k)\ H_2O\ ;\ k \leq 4 \qquad (4.3)$$

After 80 s reaction delay the signal of $[CrI(H_2O)_3]^+$ has the highest intensity (shown in supporting information). Moreover two more signals are present $[CrI(C_3H_7I)(H_2O)_2]^+$ and $[Cr(C_3H_7I)_2]^+$. After 80 s reaction delay increase of the intensity of the two clusters until 1000 s reaction delay is observed, thus both are very stable.

Kinetic analysis, shown in figure 4.2a, were done to examine the reaction rate for the oxidation reaction. The summed intensities of the educt and product are scattering slightly due to problems to keep the pressure of the reactant constant. The reaction rates for all metals are summarized in table 4.1. Chromium is reacting slightly faster than cobalt. Furthermore nanocalorimetric analysis was done for the oxidation reaction and is shown in figure 4.2b/c. Due to the behavior of the average cluster size and the difference fit, smaller clusters are reacting faster as the larger ones. The difference fit in 4.2c differs from the data points after 4 seconds, which is a sign of higher reactivity of the smaller clusters. Loss of 2.4 water molecules for the oxidation reaction is determined.

Table 4.1.: Absolute reaction rates in $cm^3\ s^{-1}$ and reaction enthalpy in $kJ\ mol^{-1}$ for the reaction of $[M(H_2O)_n]^+$, M = Cr, Mn, Fe, Co, Ni, Cu and Zn with C_3H_7I.

$[M(H_2O)_n]^+$, M=	k_{abs}	$\Delta E_{nc,1}$
Cr	$3*10^{-10}$	-102 ± 31
Mn	n. a.	n. a.
Fe	n. a.	n. a.
Co	$2.6*10^{-10}$	-36 ± 22
Ni	n. a.	n. a.
Cu	$1.5*10^{-10}$	-132 ± 24
Zn	$4.1*10^{-10}$	-75 ± 23

Cr^+ has a half-filled 3d shell with the stable configuration $3d^5$ of five parallel spins. [107] Despite this stability the oxidation reaction at nominally 0 s reaction delay to Cr^{2+} is

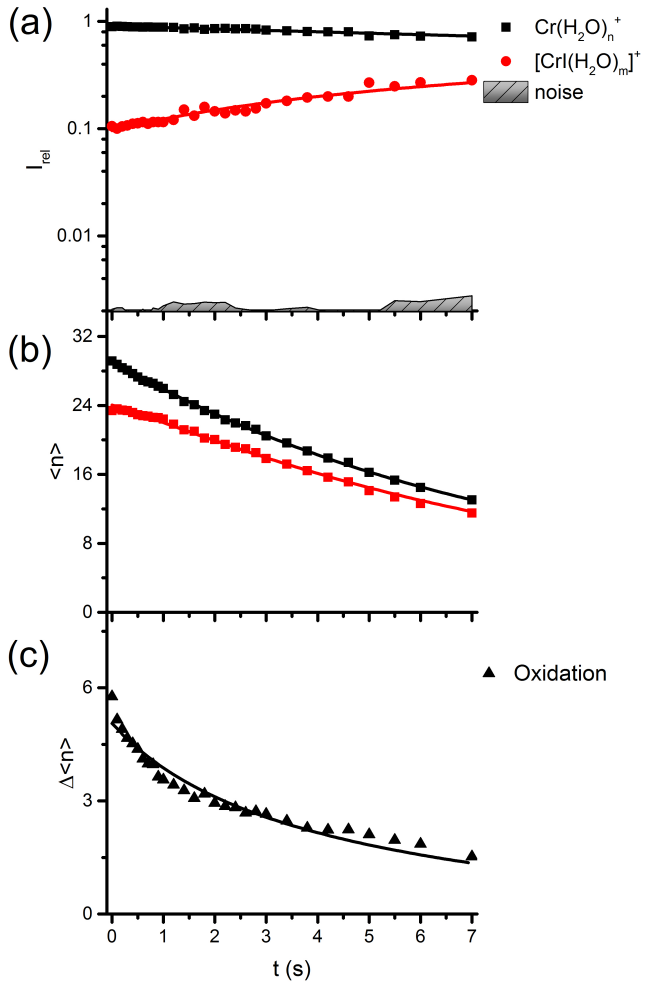

Figure 4.2.: Kinetics (a), average cluster size <n> (b) and difference of the cluster size Δ<n> (c) of the reaction of $[Cr(H_2O)_n]^+$ with C_3H_7I at a pressure of 5 x 10^{-9} mbar. Difference fit is not in good agreement with the data points

observed with iodopropane. For the ligand exchange with oxygen an intracluster reaction and formation of $[Cr,O_2,OH]^+(H_2O)_{n-y}$ was examined. [39] This reaction is only observed after the ligand exchange, in contrast with iodopropane the oxidation reaction occurs immediately. Furthermore there are indications for a charge transfer with acetonitrile, since the reaction is strongly exothermic. Moreover ligand exchange of the oxidation product is observed, which is caused by the higher electrostatic interaction between the

oxidized metal core and the iodopropane, since iodopropane has a higher polarizability (11.5 x 10-24 cm^3) [83] as water. Additionally ligand exchange is observed for smaller clusters, which is strongly size dependent. With decreasing cluster size the probability increases that iodopropane reaches a free coordination site of Cr^+.

Oxidation reactions of chromium with alkyl halides are only published with Cr^{2+} to our knowledge, since Cr^+ is not stable in aqueous environment. Kochi and Powers [108] analyzed the reduction of alkyl halides with different Cr(II) complexes. For the most reactions they observed a reduction of the alkyl halide and the formation of Cr(III) complexes with the halide. This corresponds with our observations for Cr(I).

Manganese. The reaction of hydrated Mn(I) ions, starting n = 20 – 40, with iodopropane is strongly size dependent. Only after 28 s reaction delay, shown in the mass spectra in figure 4.3 at 3 x 10^{-8} mbar, ligand exchange of one iodopropane molecule is observed.

$$[Mn(H_2O)_n]^+ + C_3H_7I \rightarrow [MnC_3H_7I(H_2O)_m]^+ + (n-m)\ H_2O\ ;\ m \leq 4 \qquad (4.4)$$

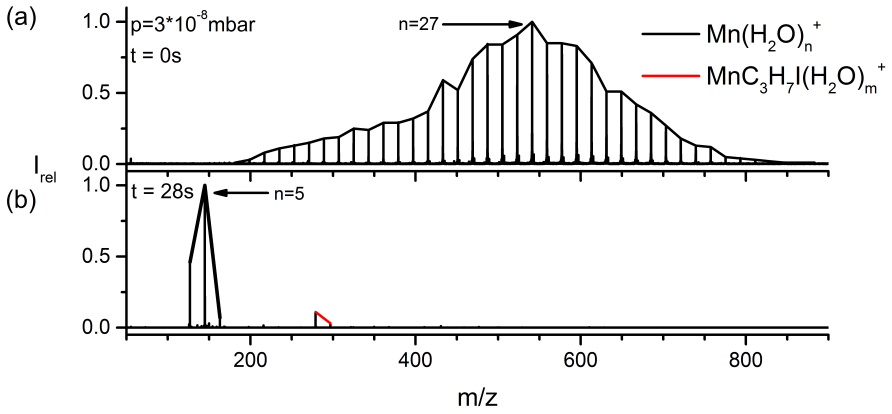

Figure 4.3.: Mass spectra of the reaction of $[Mn(H_2O)_n]^+$ with C_3H_7I at a pressure of 3 x 10^{-8} mbar after 0 (a) and 28 (b) s. Ligand exchange with iodopropane is observed.

Furthermore the formation of $[Mn(C_3H_7I)_2(H_2O)_k]^+$ is determined for longer reaction delays. The direct coordinated product without water and just iodopropaen molecules is observed as in the experiments with acetonitrile before.

$$[MnC_3H_7I(H_2O)_m]^+ + C_3H_7I \rightarrow [Mn(C_3H_7I)_2(H_2O)_k]^+ + (m-k)\ H_2O\ ;\ k \leq 2 \qquad (4.5)$$

After 30 s reaction delay low formation of oxidation product is observed.

$$[Mn(H_2O)_n]^+ + C_3H_7I \rightarrow [MnI(H_2O)_l]^+ + C_3H_7^\bullet + (n-l)\ H_2O\ ;\ l \leq 3 \tag{4.6}$$

After 80 seconds reaction delay the formation of $[MnI(C_3H_7I)(H_2O)_p]^+$ is noticed.

$$[MnI(H_2O)_l]^+ + C_3H_7I \rightarrow [MnIC_3H_7I(H_2O)_p]^+ + (l-p)\ H_2O\ ;\ p \leq 2 \tag{4.7}$$

$[MnI(C_3H_7I)(H_2O)_p]^+$ react further by ligand exchange. The last products of the reaction after 300 s reaction delay are $[MnI(C_3H_7I)_2]^+$ and $[MnI(C_3H_7I)_3]^+$ (see supporting information).

Both reactions occur at long reaction delay, when the cluster size is smaller than 10 water molecules, hence the free coordination site is more accessible. Furthermore at long reaction delays the oxidation product $[MnI(C_3H_7I)_{2\text{-}3}]^+$ is more stable than the ligand exchange product $[Mn(C_3H_7I)_2]^+$. As in the case of the reaction with acetonitrile the complete loss of water molecules is observed.

An earlier study of the reactions of $[Mn(H_2O)_n]^+$ with D_2O showed that $[Mn(H_2O)_n]^+$, n $\leq$ 20, undergo an intracluster redox reaction with formation of $[HMnOH(H_2O)_{n\text{-}1}]^+$. [85] Therefore equation 4.6 can be described with the hydroxide geometry.

$$\begin{aligned}[HMnOH(H_2O)_{n-1}]^+ + C_3H_7I \rightarrow \\ [HMnOHI(H_2O)_{l-1}]^+ + C_3H_7^\bullet + (n-l)H_2O\ ;\ l \leq 3\end{aligned} \tag{4.8}$$

The complete loss of water molecules indicates that the intracluster reaction leading to $[HMnOH(H_2O)_{n\text{-}1}]^+$ is reversible. This was verified by experiments with a smaller cluster distribution of $[Mn(H_2O)_n]^+$, n = 10 – 20, performed at the same pressure, to make sure that $[HMnOH(H_2O)_{n\text{-}1}]^+$ are formed by BIRD before the uptake of the first acetonitrile molecule. Loss of all water molecules was also observed here.

Mn^+ has a half-filled 3d shell and one electron in the 4s shell. [109] Thus, the oxidation is possible with the loss of the 4s electron. Either ligand exchange nor the oxidation of the metal were observed by Uppal and Staley [109] with bare manganese monovalent cations with different alkyl chlorides in the gas phase.

Iron. Monovalent hydrated $[Fe(H_2O)_n]^+$ ions, starting with n= 15 – 40, show as manganese clusters a strong size dependence. Only after 5 seconds reaction delay ligand

exchange reaction, as shown in equation 4.9, with iodopropane is observed. But for the first seconds the signal intensity is rather low. Mass spectra are shown in the supporting information. After 9 seconds reaction delay oxidation reaction is observed.

$$[Fe(H_2O)_n]^+ + C_3H_7I \rightarrow [FeC_3H_7I(H_2O)_m]^+ + (n-m)\ H_2O\ ;\ m \leq 10 \qquad (4.9)$$

$$[Fe(H_2O)_n]^+ + C_3H_7I \rightarrow [FeI(H_2O)_l]^+ + C_3H_7^{\bullet} + (n-l)\ H_2O\ ;\ l \leq 10 \qquad (4.10)$$

Stronger increase of the product intensity is observed only at 12 seconds reaction delay, when the educt clusters consists of up to 10 water molecules. Furthermore for longer reaction delay the ligand exchange for the primary products is noticed.

$$[FeC_3H_7I(H_2O)_m]^+ + C_3H_7I \rightarrow [Fe(C_3H_7I)_2(H_2O)_k]^+ + (m-k)\ H_2O\ ;\ k \leq 3 \qquad (4.11)$$

$$[FeI(H_2O)_l]^+ + C_3H_7I \rightarrow [FeIC_3H_7I(H_2O)_p]^+ + (l-p)\ H_2O\ ;\ p \leq 3 \qquad (4.12)$$

$[FeI(C_3H_7I)_3]^+$ is the most stable product till 250 s reaction delay. Reactions with impurities in the measurement cell after 50 s cause the decay. Furthermore the insertion into the I-C bond cannot be excluded.

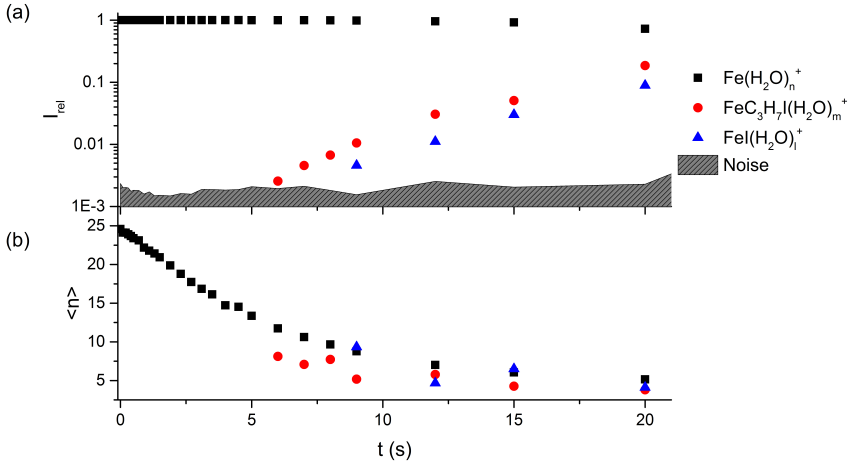

Figure 4.4.: Summed intensities (a) and average cluster size (b) of the reaction of $[Fe(H_2O)_n]^+$ with C_3H_7I at a pressure of 4 x 10^{-8} mbar. High reactivity for small clusters is observed from 12 s reaction delay.

As in figure 4.4a shown, the summed intensity of the products is increasing not continuously and not with pseudo first order behavior like the reaction with chromium. Also the

sudden decrease of the intensity of $[Fe(H_2O)_n]^+$ after five seconds reaction delay shows the high reactivity of the small clusters. Furthermore the behavior of the educt average cluster size is changing after 5 seconds, since the reaction is starting. Previously the cluster size is shrinking caused by BIRD. Comparison of the product intensities with the average cluster size shows that the ligand exchange reaction occur in a small cluster-size regime around n = 4-20 and the oxidation reaction n = 4 – 15. A similar cluster size dependence was observed for the reaction of $[Fe(H_2O)_n]^+$ with nitric oxide. [68] The initial uptake of NO and formation of HNO occur in a cluster regime around n = 15 – 25. It seems that the solvation shell is hindering the reaction of Fe^+, since iodopropane is a relatively large molecule in comparison with nitric oxide the reaction is starting in a smaller cluster size regime as for nitric oxide.

The oxidation product is more stable than the ligand exchange product, since the interactions between the metal core Fe^{2+} and the ligands are higher as for Fe^+. Furthermore Baranov et al. [110] observed for FeO^+ the sequential addition of three ligand molecules with H_2O, CO_2 and N_2O in the gas phase. These observations are corresponding to the availability of three free coordination sites around the iron ion, since Fe^{2+} has the electron configuration d^5. [107] Our results are consistent with the measurements of Allison and Ridge. [24] They examined the chemistry of bare metal cations Fe^+ with alkyl halides and alcohols in the gas phase. The formation of FeI^+ and the formation of $FeCH_3I^+$ was observed with iodomethane. The addition of the whole molecule was only observed by ligand exchange with $Fe(CO)^+$.

Cobalt. The oxidation reaction of $[Co(H_2O)_n]^+$, starting with n = 15 – 40, was studied with iodopropane. Mass spectra are shown in the supporting information. Product peaks of $[CoI(H_2O)_m]^+$ with very low intensity are noticed at nominally 0 s reaction delay.

$$[Co(H_2O)_n]^+ + C_3H_7I \rightarrow [CoI(H_2O)_m]^+ + C_3H_7^\bullet + (n-m)\ H_2O \qquad (4.13)$$

Furthermore ligand exchange is observed after 10 s reaction delay:

$$[Co(H_2O)_n]^+ + C_3H_7I \rightarrow [CoC_3H_7I(H_2O)_l]^+ + (n-l)\ H_2O\ ;\ l \leq 5 \qquad (4.14)$$

Both products are reacting further by ligand exchange with up to three iodopropane molecules.

Furthermore at 15 s reaction delay the additional formation of $[CoC_3H_6(C_3H_7I)_2]^+$ is observed, which is besides $[CoI(C_3H_7I)_3]^+$ the second main product of the reactions.

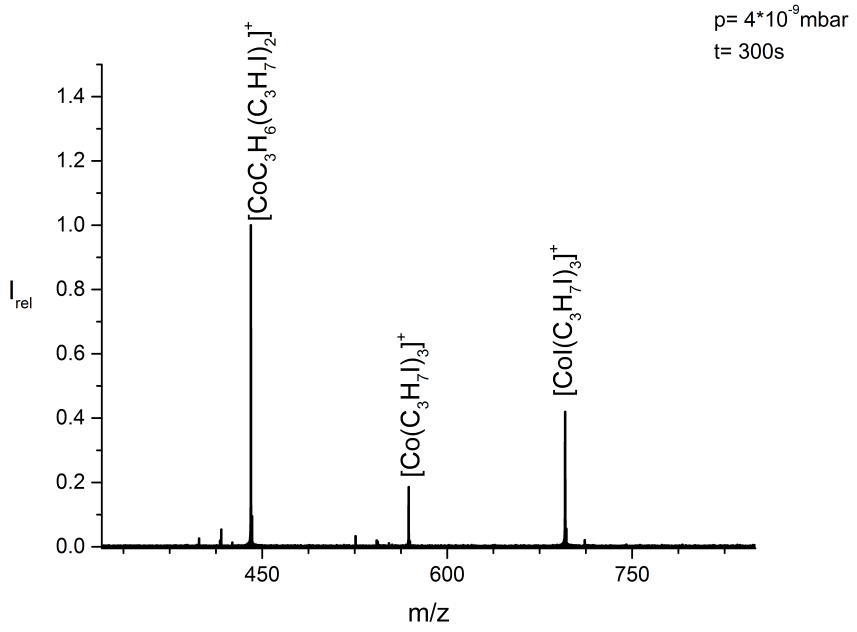

Figure 4.5.: Mass spectrum of the reaction of $[Co(H_2O)_n]^+$ with C_3H_7I at a pressure of 4 x 10^{-9} mbar after 300 s. Quantitative formation of $[Co(C_3H_7I)_2C_3H_6]^+$ is observed. Small peaks caused by reactions with impurities are noticed at longer reaction delays.

$[CoI(C_3H_7I)_3]^+$ is the product of the oxidation reaction, while $[CoC_3H_6(C_3H_7I)_2]^+$ is the product of the ligand exchange reaction. It seems to be more favored and stabilized as the oxidation product, since the intensity of the clusters is the highest one until 300 s reaction delay (figure 4.5). Moreover the ratio between both products remains the same for longer reaction delays except the fact that product intensities with impurities increase (figure 4.6).

The kinetic and nanocalorimetric analysis of the oxidation reaction, shown in figure 4.7, is in good agreement with the data points. Both the cluster fit (b) and the difference fit (c) not deviates from the data points, which is different to chromium. Therefore the resulting value for the reaction enthalpy seems to be reliable. During the oxidation

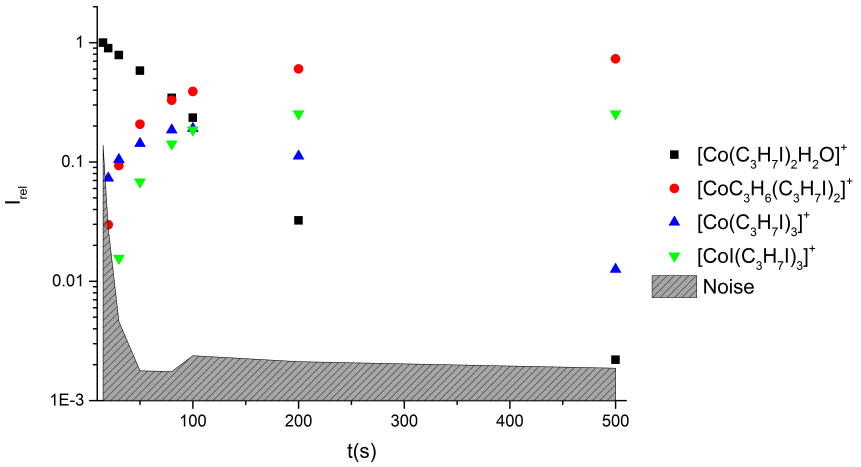

Figure 4.6.: Product intensity as a function of reaction delay (15 – 500 s) for $[Co(C_3H_7I)_3]^+$ (blue) and $[Co(C_3H_7I)_2C_3H_6]^+$ (red).

loss of one water molecule is determined, thus the reaction is not as exothermic as with hydrated chromium or zinc cations. Also the oxidation reaction with cobalt is the slowest one.

Compared with the other metals for cobalt small clusters are additionally reacting by ligand exchange too. However, formation of $[CoC_3H_6(C_3H_7I)_2]^+$ is observed at longer reaction delay. Two mechanisms are possible for the formation. On the one hand loss of HI of $[Co(C_3H_7I)_3]^+$ and on the other hand the reaction of $[Co(C_3H_7I)_2(H_2O)]^+$ with iodopropane may lead to the formation of the product (see figure 4.6). A hint is the almost complete loss of the signal intensity of $[Co(C_3H_7I)_3]^+$ at 500 s reaction delay. This reaction is known for bare cobalt cations with 2-chloropropane in the gas phase. [111] Allison and Ridge [111] observed for the reaction of bare Co^+ and Ni^+ with chloropropane in the gas phase a metal insertion followed by formation of $MC_3H_6^+$ and HCl. Furthermore they observed for the ligand exchange product $[Co(NO)C_3H_7Cl]^+$ the formation of $[C_3H_6Co(NO)C_3H_7Cl]^+$ during the reaction with a further i-C_3H_7Cl. These reactions are only noticed in presence of a β-hydrogen, since for chloromethane no formation of HCl was observed, shown in equation 4.15/4.16. [111]

$$M^+ + CH_3Cl \nrightarrow [MCH_2]^+ + HCl \tag{4.15}$$

$$M^+ + C_2H_5Cl \rightarrow [MC_2H_4]^+ + HCl \tag{4.16}$$

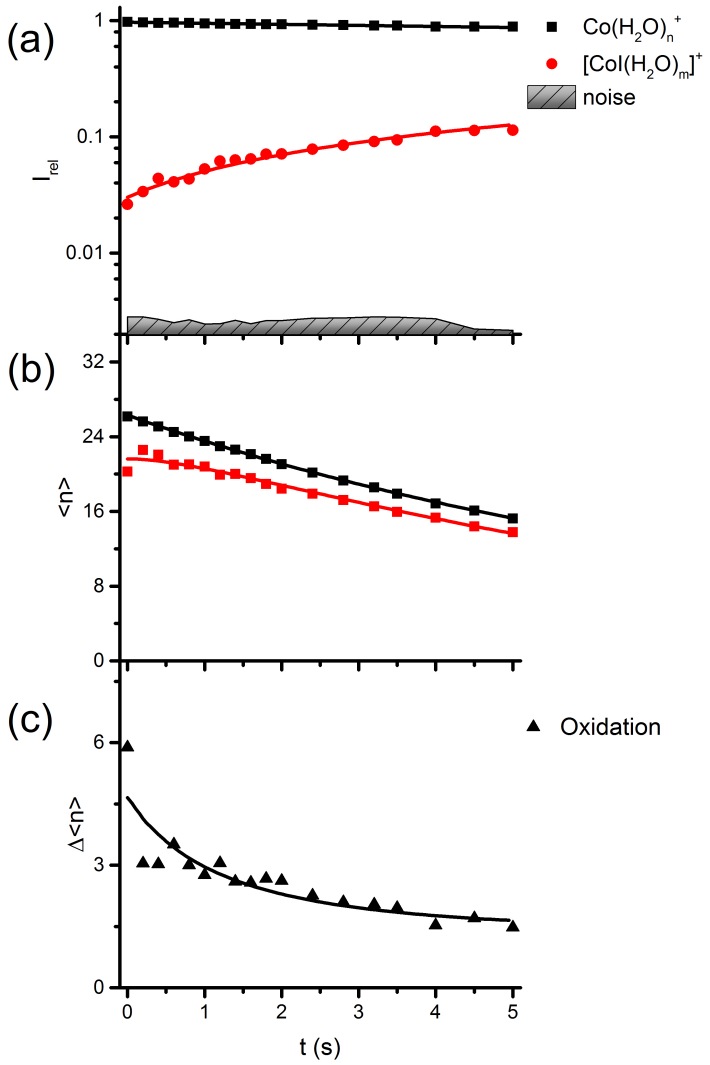

Figure 4.7.: Kinetics (a), average cluster size <n> (b) and difference of the cluster size Δ<n> (c) of the reaction of $[Co(H_2O)_n]^+$ with C_3H_7I at a pressure of 4 x 10^{-9} mbar. The fits agree well with the measured average cluster size of the reaction.

Moreover the formation of methanol and ethane were observed for reactions with propanol and bare Co^+ ions. [8]

Nickel. Monovalent hydrated Nickel cations $[Ni(H_2O)_n]^+$, starting with n = 15 – 40, show a weak ligand exchange with iodopropane for the first 3 seconds. Mass spectra are shown in the supporting information.

$$[Ni(H_2O)_n]^+ + C_3H_7I \rightarrow [NiC_3H_7I(H_2O)_m]^+ + (n-m)\ H_2O \tag{4.17}$$

Due to the weak ligand exchange the product peaks intensity is low until 3 seconds reaction delay. After 3 seconds reaction delay, when the number of water molecules is for the product clusters $m \leq 6$, the reaction is faster. After 6 seconds reaction delay the sequential uptake of up to four iodopropane molecules is observed.

$$[NiC_3H_7I(H_2O)_m]^+ + C_3H_7I \rightarrow [Ni(C_3H_7I)_{2-4}(H_2O)_k]^+ + (m-k)\ H_2O \tag{4.18}$$

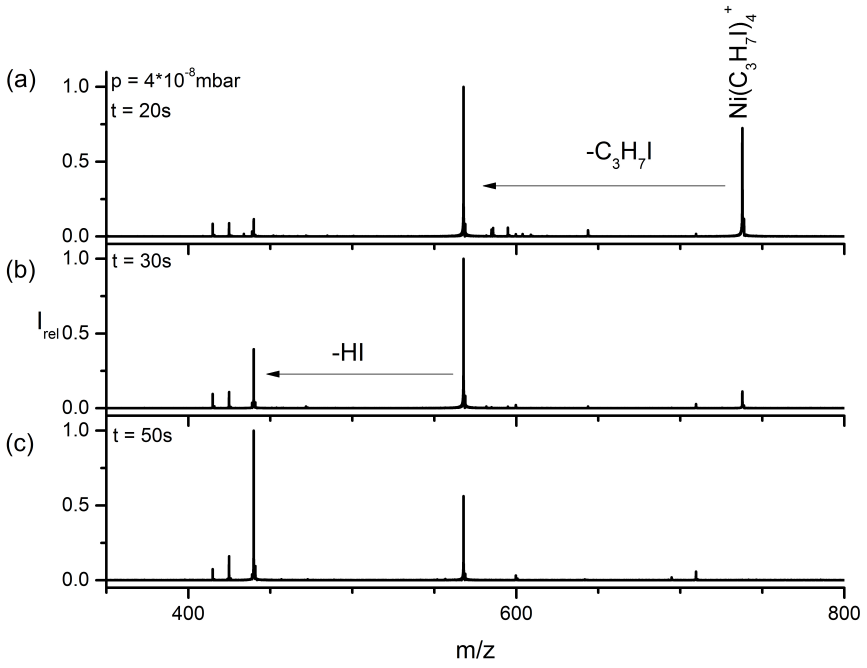

Figure 4.8.: Mass spectra of the reaction of $[Ni(H_2O)]_n^+$ with C_3H_7I at a pressure of 4 x 10^{-8} mbar after 20 (a), 30 (b) and 50 s (c). Formation of $[Ni(C_3H_7I)_2C_3H_6]^+$ is observed. Small peaks are belonging to reaction with impurities

At 15 seconds reaction delay $[Ni(C_3H_7I)_4]^+$ has the highest intensity. Particularly after 10 seconds reaction delay the formation of $[Ni(C_3H_7I)_2C_3H_6]^+$ is observed. The mass

spectra and the product intensity as a function for the reaction delay for the formation are shown in figure 4.8/4.9. The intensity of $[Ni(C_3H_7I)_3]^+$ is constant until 30 s, since it is formed by the loss of iodopropane from $[Ni(C_3H_7I)_4]^+$. $[Ni(C_3H_7I)_2C_3H_6]^+$ cannot be the product of the reaction of $[Ni(C_3H_7I)_2]^+$ with iodopropane due to the absence of $[Ni(C_3H_7I)_2]^+$. So we assume the loss of HI and formation of $[Ni(C_3H_7I)_2C_3H_6]^+$ as shown in equation 4.19.

$$[Ni(C_3H_7I)_3]^+ \rightarrow [Ni(C_3H_7I)_2C_3H_6]^+ + HI \tag{4.19}$$

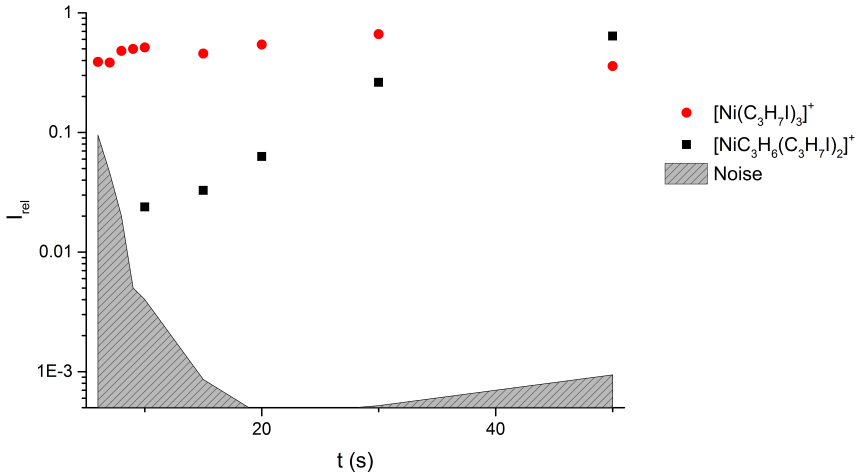

Figure 4.9.: Product intensity as a function of reaction delay (6 – 50 s) for $[Ni(C_3H_7I)_3]^+$ (red) and $[Ni(C_3H_7I)_2C_3H_6]^+$ (black).

The measured summed intensities and the average cluster size for the ligand exchange reaction are shown in figure 4.10. For the first 2 seconds the intensity of the product clusters is low and a weak increase of the intensity is observed. After 3 s reaction delay the intensity of the product is strongly increasing. Furthermore the intensity of $[Ni(H_2O)_n]^+$ is decreasing with higher reactivity after 5 s reaction delay. This behavior is also reflected in the average cluster size, since the loss of water molecules is a nonlinear process. Surprisingly the average cluster size of the product remains constant after the first seconds reaction delay. This is evident in the mass spectra (see supporting information) due to the constant product cluster distribution, which does not change to smaller clusters in the period of 4 until 8 seconds reaction delay. In this time period only the increase of the intensity of the product clusters is observed. These clusters react

further by ligand exchange. Due to the high reactivity of the further ligand exchange and the high reactivity of the first ligand exchange the cluster size remains constant and loss of water molecules caused by BIRD is not observed for the first 15 seconds. Thus, it is a stationary state where the clusters are preferably formed and react further.

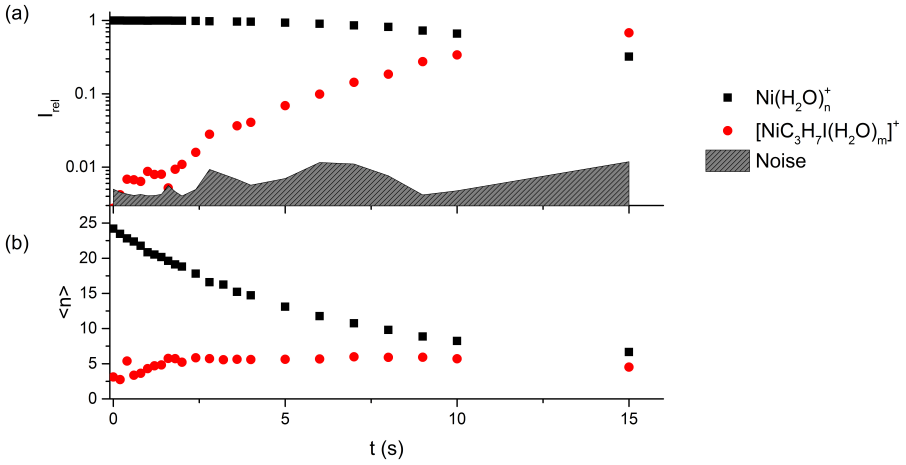

Figure 4.10.: Summed intensities (a) and average cluster size (b) of the reaction of $[Ni(H_2O)_n]^+$ with 1-C_3H_7I at a pressure of 4 x 10^{-8} mbar. High reactivity for small clusters is observed from 3 s reaction delay.

Besides cobalt also for bare monovalent nickel cations several experiments [8,23,111] are known, where a metal insertion mechanism is followed by formation of olefins in the gas phase investigated.

Copper. $[Cu(H_2O)_n]^+$, starting with n= 15–40, are reacting towards iodopropane, showing in figure 4.11 at a pressure of 4 x 10^{-8} mbar, by ligand exchange.

$$[Cu(H_2O)_n]^+ + C_3H_7I \rightarrow [CuC_3H_7I(H_2O)_m]^+ + (n-m)\ H_2O \qquad (4.20)$$

At nominally 0 seconds reaction delay the uptake of the first molecule is determined. After 1.2 s reaction delay the uptake of the second molecule is noticed. 50 % of the educt reacted at 4 seconds reaction delay and at 5 seconds the intensity of the $[Cu(C_3H_7I)_2(H_2O)_k]^+$ is higher than of the educt. Additionally the uptake of the third iodopropane molecule was observed at 5 s. Overall the uptake of up to five molecules was determined. However at long reaction delays the evaporation of the uptake iodopropane

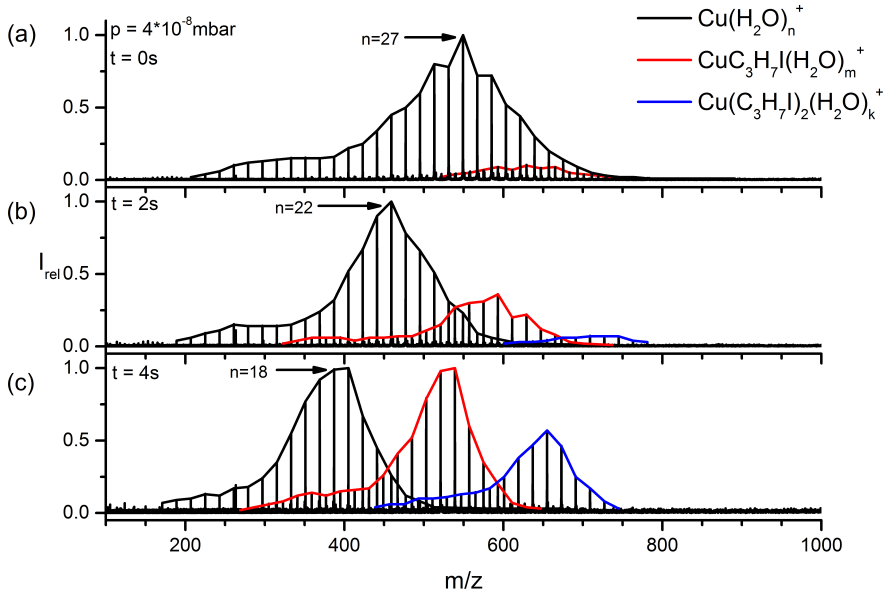

Figure 4.11.: Mass spectra of the reaction of $[Cu(H_2O)_n]^+$ with C_3H_7I at a pressure of 4 x 10^{-8} mbar after 0 (a), 2 (b) and 4 (c) s. The ligand exchange with two iodopropane molecules was observed.

molecules is noticed (shown in the supporting information). After 500 s reaction delay at a pressure of 4 x 10^{-9} mbar the products of the reaction are $[Cu(C_3H_7I)_2]^+$ and $[Cu(C_3H_7I)H_2O]^+$, which show the high stability of the clusters.

The kinetic analysis could not be done for the pressure of 4 x 10^{-8} mbar, because the fit was impossible due to the fast second uptake. Therefore the kinetic and nanocalorimetric analysis was done for 4 x 10^{-9} mbar. As shown in figure 4.12 the intensity of $[Cu(C_3H_7I)_2(H_2O)_k]^+$ is increasing faster than from the first product. A possible explanation is that the first iodopropane molecule is polarizing the metal core, due to the higher dipole moment (2.04 D) and polarizability (11.5 x 10^{-24} cm^3) than water [83], whereby the uptake of the second molecule is preferred. The cluster size could have an important influence as well. The uptake of the second molecule starts at 1.2 seconds with $[CuC_3H_7I(H_2O)_m]^+$, so the charge of the metal core has a stronger influence on the molecule.

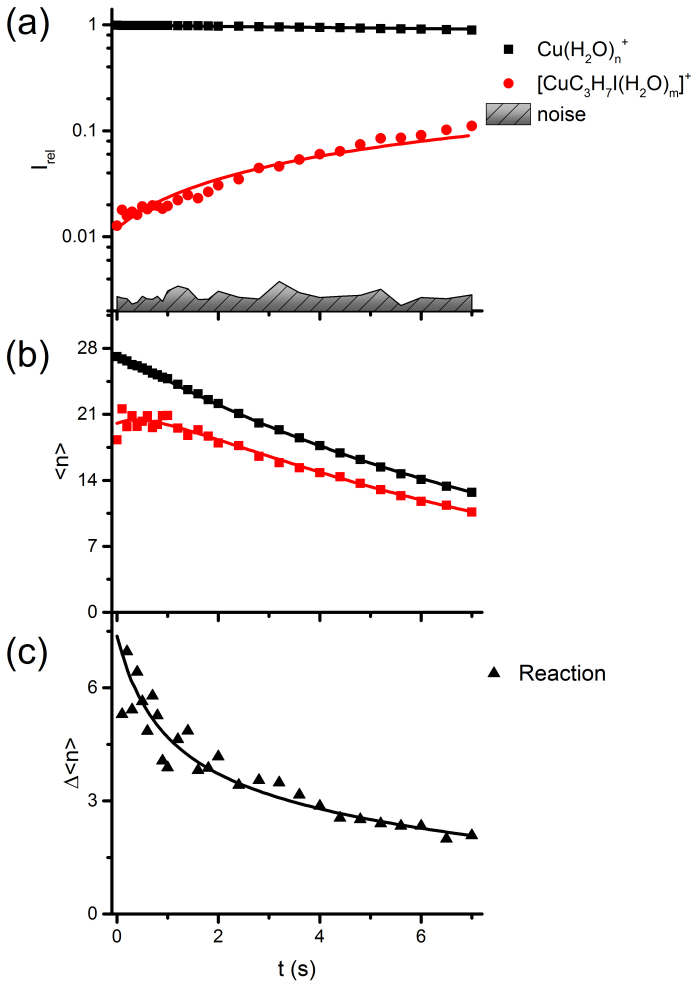

Figure 4.12.: Kinetics (a), average cluster size <n> (b) and difference of the cluster size Δ<n> (c) of the reaction of $[Cu(H_2O)_n]^+$ with C_3H_7I at a pressure of 4 x 10^{-9} mbar. The fits agree well with the measured average cluster size of the reaction.

Furthermore another explanation is possible. Jones and Staley [112] analyzed the chemistry of Cu^+ with alkyl chlorides in the gas phase. They observed that Cu^+ reacts with alkyl halides by dehydrochlorination with retention of HCl or alkene by Cu(I). It is nontransferable one–to–one due to their experimental conditions, but it shows that the reaction between alkyl halides and Cu^+ ions is possible. Furthermore Lang et al. [113]

determined the amination of aryl halides using Cu(I) catalysis in solution. Using Cu_2O as a catalyst iodobenzene was converted to aniline with 74 % yield.
They assume the insertion of Cu(I) in the I-C bond and subsequent activation for the amination. Therefore we assume there is an intra–cluster reaction, where Cu^+ inserts into the I–C_3H_7 bond. It would explain the slow reaction towards the second uptake and the high stability of $[Cu(C_3H_7I)H_2O]^+$. But the energy barrier for the elimination of HI is higher than for cobalt and nickel. Furthermore the nanocalorimetry analysis (shown in figure 4.12) shows that the reaction with the first iodopropane molecule is exothermic.

Zinc. The reaction of iodopropane with $[Zn(H_2O)_n]^+$ is the fastest reaction. The mass spectra at a pressure of 4 x 10^{-8} mbar are shown in the supporting information. At nominally 0 s reaction delay the intensity of the product $[ZnI(H_2O)_m]^+$ is higher than the educt. After 6 seconds all educt clusters reacted completely and only $[ZnI(H_2O)_m]^+$ is detected. At 8 seconds a ligand exchange of $[ZnI(H_2O)_m]^+$ is observed.

$$[ZnI(H_2O)_m]^+ + C_3H_7I \rightarrow [ZnI(C_3H_7I)_{1-3}(H_2O)_k]^+ + (m-k)\ H_2O\ ;\ m \leq 21 \qquad (4.21)$$

In figure 4.13 the stepwise uptake of C_3H_7I at 20 s is shown. Accordingly to the loss of water molecules the iodopropane molecules seems to be bound stronger than the water molecules, since all water molecules are exchanged. After 60 s reaction delay $[ZnI(C_3H_7I)_3]^+$ has the highest intensity, but at longer reaction delays loss of ligands is observed.

The final product of the reaction could not be observed due to the relatively high pressure and reactions with impurities.

Our results with alkyl iodide show the primary formation of $[ZnI(H_2O)_m]^+$ by an oxidation, which can undergo ligand exchange reaction with iodopropane molecules at longer reaction delays. Hence, ligand exchange reaction occur in a small cluster size regime for the other metals, the reaction is not observed, since all clusters are reacting by oxidation before reach the small cluster size regime. The kinetic and nanocalorimetric analysis are shown in figure 4.14. For the smaller clusters the difference fit is not in a good agreement with the data points, since the clusters are reacting faster than the larger clusters.

The results of Guijaro et al. [114] show that the reaction of activated zinc with alkyl bromides follow a different mechanism as aryl halides. Due to their Hammett plots they

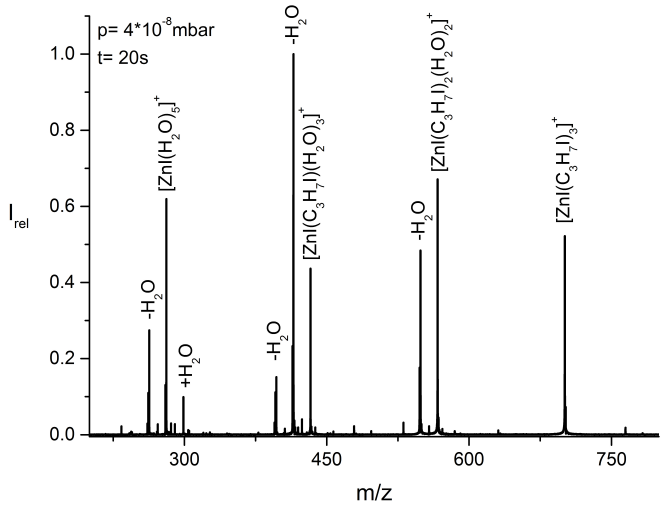

Figure 4.13.: Mass spectrum of the reaction of $[Zn(H_2O)_n]^+$ with C_3H_7I at a pressure of 4 x 10^{-8} mbar after 20 s. A stepwise ligand exchange of $[ZnI(H_2O)_m]^+$ with C_3H_7I is observed. Small peaks are belonging to the zinc dimer products and impurities with ammonia.

suggest an oxidative addition via an inner sphere electron transfer. They could not prove it, hence after a further electron transfer Zn^{2+} is reacting very fast by ligand exchange to RZnBr.

4.3. Discussion

In the study two primary reactions ligand exchange and oxidation reaction by formation of MI^+- core with iodopropane were observed. Only for vanadium no reaction with iodopropane was observed, although empty and partly filled d orbitals are available for bonding in V^+. It is possible, that $V^+(H_2O)$ contain a $HVOH^+$ ionic core with the spin multiplicity triplet, [115] which would change the coordination chemistry and reactivity of the vanadium center.

The oxidation reaction was observed for chromium, manganese, iron, cobalt and zinc, only monovalent copper and nickel cations are not showing the formation of MI^+-core.

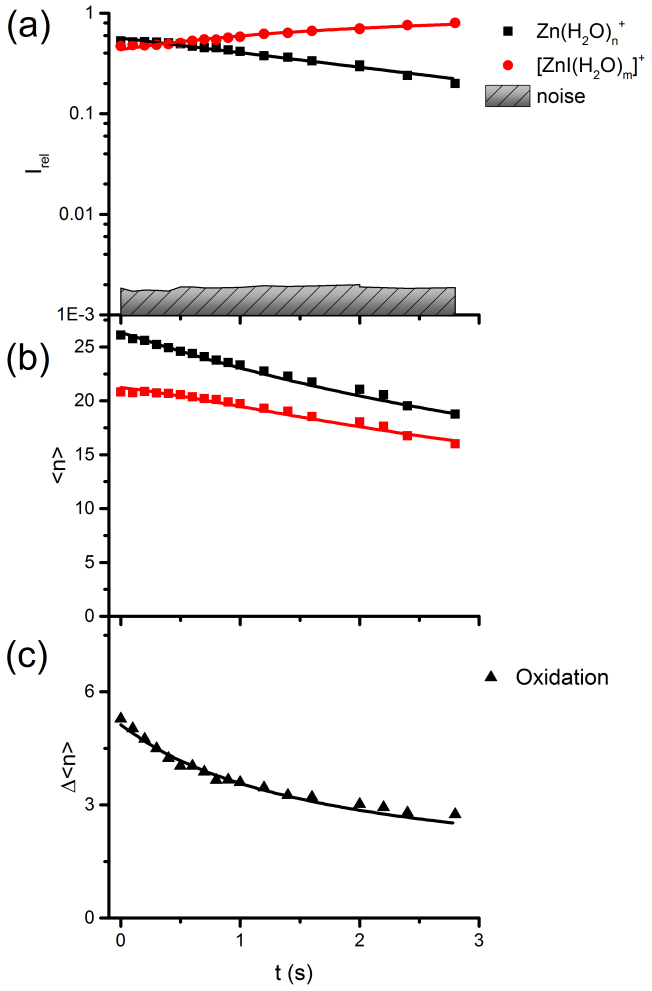

Figure 4.14.: Kinetics (a), average cluster size <n> (b) and difference of the cluster size Δ<n> (c) of the reaction of $[Zn(H_2O)_n]^+$ with C_3H_7I at a pressure of 4 x 10^{-9} mbar for the first 3 seconds. The kinetic fits follow a pseudo first order behaviour.

Cu^+ has filled d orbitals and an empty 4s orbital, [107] therefore the reactivity of hydrated monovalent copper ions is low. [68] Although Ni^+ has an electron configuration of $3d^9$ and one partly filled d orbital is available, [87] it shows for the most reactions only ligand exchange. [39,68] It seems that the reactivity of Ni^+ is sensitive to the hydration shell.

Furthermore this is confirmed by the observations, that the ligand exchange is faster with decreasing cluster size.

Chromium, cobalt and zinc are reacting with very similar total rates, but they differ in the determined reaction enthalpy. Thereafter the reaction with $[Co(H_2O)_n]^+$ is less exothermic than with zinc and chromium. The different reactivity can be justified in the electronic structure of the monovalent metals. Whereas for Zn^+ the additional electron is located in an s orbital, for Cr^+ and Co^+ it is located in the d orbital. Moreover Co^+ has the electron configuration $3d^8$ with low energy density on six coordination sites, [69] while Cr^+ has singly occupied d orbitals. [116] Therefore high reaction enthalpy was also observed for the reaction of Cr^+ with acetonitrile and oxygen. [68] However, manganese and iron are only showing a reaction in a narrow cluster size regime. This shows a high dependence on the solvation shell of the reactivity. Furthermore for manganese exchange experiments with D_2O together with BIRD experiments for the same metals showed that only $[Mn(H_2O)_n]^+$ undergoes an intracluster redox reaction to form $[HMnOH(H_2O)_{n-1}]^+$ for $n \leq 20$. [85] Therefore the reason for the late reaction could be caused by the reverse of the intracluster reaction.

Ligand exchange reaction is observed for all metals except zinc. This reaction is strongly dependent on the cluster size and mostly occurs at small cluster sizes. On the one hand it depends probably on the bad solubility (1.14 g/kg H_2O) [83] of iodopropane in aqueous environment, on the other hand the solvation shell inhibits the free coordination sites of the metal ion. $[Zn(H_2O)_n]^+$ is not reacting by ligand exchange, since all clusters react by formation of $[ZnI(H_2O)_n]^+$ before small clusters of the educt can be reached.

For the ligand exchange reaction of $[Ni(H_2O)_n]^+$ and $[Co(H_2O)_n]^+$ with iodopropane the formation of $[MC_3H_6(C_3H_7I)_2]^+$ is observed for longer reaction delay. The formation of $MC_3H_6^+$ with cobalt and nickel was also investigated by Allison and Ridge. [24] Our results show, that $[NiC_3H_6(C_3H_7I)_2]^+$ is formed by loss of HI from $[Ni(C_3H_7I)_3]^+$, while for cobalt it is not so explicit and can also be formed by the reaction of $[Co(C_3H_7I)_2]^+$ with a further iodopropane.

The formation of olefins by metal insertion of cobalt and nickel was already studied by several groups and used commercially. Allison and Ridge [24] observed the formation of $MC_3H_6^+$ with alcohols and alkyl halides in the gas phase. This was only noticed for reactant molecules with β-H atoms. The possible metal insertion mechanism is shown

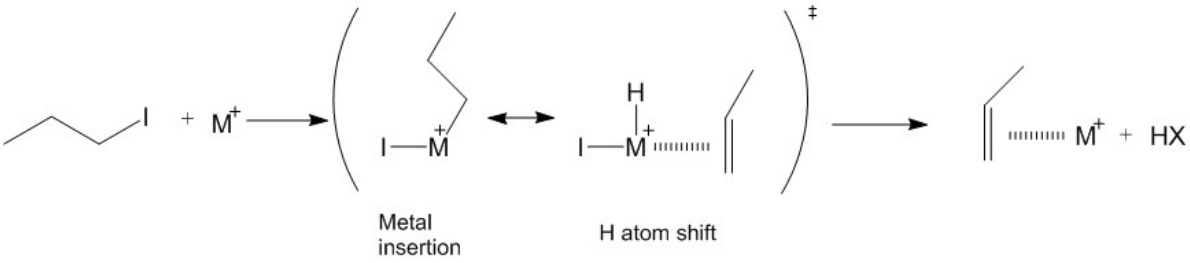

Scheme 4.1: Possible metal insertion mechanism for cobalt and nickel for the formation of $MC_3H_6^+$. Based on Ref. [24]

in scheme 4.1. The metal inserted into the RC–I bond by formation of a halide–metal–carbon complex. Within this complex a migration from the β–H atom to the metal is possible. This migration results in the formation of a double bond between the carbon atoms. It follows the loss of hydrogen iodide and the observed complex of the metal with the olefin. Moreover monovalent cobalt and nickel cations react with linear alkanes by insertion into the C-C bond through the formation of olefins. [23] Therefore nickel was used commercially as catalyst for the preparation of nylon. [117]

An indication for the formation of the olefin is the product $[MC_3H_6(C_3H_7I)_2]^+$. For both $[Co(H_2O)_n]^+$ and $[Ni(H_2O)_n]^+$ it has been demonstrated by infrared spectroscopy, that the first solvation shell is consisting of three water molecules and the fourth molecule is located in the second solvation shell. [69, 86] This is also verified by the ligand exchange reaction with acetonitrile hence the products $[Co(CH_3CN)_3]^+$ and $[Ni(CH_3CN)_3]^+$ were observed. Would it be a covalent bond between the metal ion and the carbon atom of C_3H_6, then the oxidation state of the metal would change and therefore the coordination chemistry. In conclusion, an metal insertion into the I-C bond cannot be excluded for all metals. This has to be proved with spectroscopy.

Supporting Information

The mass spectra for the reaction of $[M(H_2O)_n]^+$, M = Fe, Co, Ni and Zn, with C_3H_7I are summarized in the supporting information. Additionally figures with mass spectra for the reaction of hydrated Cr(I), Mn(I), Fe(I) and Cu(I) with C_3H_7I for long reaction delays are shown.

5. Reactivity of hydrated monovalent first row transition metal ions $M(H_2O)_n^+$, M = Cu and Zn, n $\leq$ 50, towards C_6H_5X (X = F, Cl, Br and I)

5.1. Introduction

For the chemistry of bare metal ions [111] mechanistic investigations are focused on the activation of the C-Cl bond of alkyl chlorides. For example the reactions of Pt^+ with alkyl chlorides and fluoride were studied experimentally and theoretically. [118] Dehydrogenation and HX elimination were found to be the primary reaction channels. On the other hand chlorine transfer and oxidative halogen transfer by formation of TiX^+ are the most common reactions of Ti^+ with halomethanes and alkyl chlorides in the gas phase. [119] Several transition metals, such as Sc^+, Ti^+, V^+, Fe^+, Co^+ and Ni^+ induce a metal catalyzed polymerization with halonaphthalenes forming $[M(C_{10}H_6)_n]^+$. [120] Metal Fe^+ cations show interesting results with aryl halides in the gas phase, due to the induced dehydrohalogenation and polymerization. [121] In addition Fe(benzene)$^+$ and Fe(naphthene)$^+$ are reacting with unsaturated hydrocarbons by coupling reactions. [122, 123]

Aryl halides are important chemical building blocks in the organic chemistry. They are used for derivatization or coupling reactions. Above all, they are often used in organometallic synthesis, like in the Ullmann reaction (copper-catalyzed N-arylation of amines) [124] and the related Goldberg reaction (copper-catalyzed N-arylation of amides). [125] The necessity of high temperatures, highly polar solvents and often large amounts of copper reagents have prevented these reactions from being employed to their full potential. [126] In general, catalytical organometallic chemistry for the formation of carbon-heteroatom bonds is less developed and is less well understood. Therefore further information about the metal catalytic processes is necessary for the optimization of the syntheses.

To learn more about the reactions of the transition metal cations in water clusters with aryl halides, the interaction of $[M(H_2O)_n]^+$, M = Cu and Zn (n$\sim$ 20–50) with C_6H_5X (X = F, Cl, Br and I) was investigated. Zinc was chosen due to the high reactivity with other reactants and copper as an example for the low reactivity metals. Furthermore DFT calculations were done to explain the reactions with monovalent hydrated Zn(I).

5.2. Experimental and Theoretical Details

The reactants were introduced into the ultrahigh vacuum region by a needle valve at a constant pressure in the range of 5 x 10^{-9} mbar to 4 x 10^{-7} mbar. Moreover geometry optimization and thermochemistry for the reactions:

$$Zn(H_2O)_3^+ + C_6H_5X \longrightarrow ZnC_6H_5(H_2O)_3^+ + X^\bullet \tag{5.1}$$

$$Zn(H_2O)_3^+ + C_6H_5X \longrightarrow ZnX(H_2O)_3^+ + C_6H_5^\bullet \tag{5.2}$$

have been examined using DFT at the B3LYP aug-cc-pVQZ-PP level of theory for a small model $Zn(H_2O)_3^+$ using the Gaussian 09 package. [92]

5.3. Experimental Results

Reaction with fluorobenzene. Both monovalent hydrated copper and zinc cations do not react with fluorobenzene even at a relatively high pressure of 10^{-7} mbar.

Copper.*Reaction with chlorobenzene.* Hydrated monovalent copper ions $[Cu(H_2O)_n]^+$, starting with n = 15 – 40, are reacting towards chlorobenzene. Figure 5.1 shows the mass spectra of the reaction of $[Cu(H_2O)_n]^+$ with chlorobenzene at different delays. A ligand exchange between water and chlorobenzene was observed from nominally 0 seconds reaction delay.

The cluster distribution is shrinking through absorbed blackbody radiation, followed by evaporative cooling (BIRD). [21, 42–44] For all hydrated cupper ions ligand exchange, as shown in equation 5.3/5.4 , is determined:

$$[Cu(H_2O)_n]^+ + C_6H_5Cl \longrightarrow [CuC_6H_5Cl(H_2O)_m]^+ + (n-m)\ H_2O \tag{5.3}$$

$$[CuC_6H_5Cl(H_2O)_m]^+ + C_6H_5Cl \longrightarrow [Cu(C_6H_5Cl)_2(H_2O)_k]^+ + (m-k)\ H_2O \tag{5.4}$$

Here, n denotes the number of water molecules in the reactant clusters and m/k are the numbers of water molecules left in the clusters. After 9 seconds reaction delay the uptake of a second chlorobenzene molecule is observed and after 14 seconds a third uptake is determined. Loss of the third molecule is observed for longer reaction delays

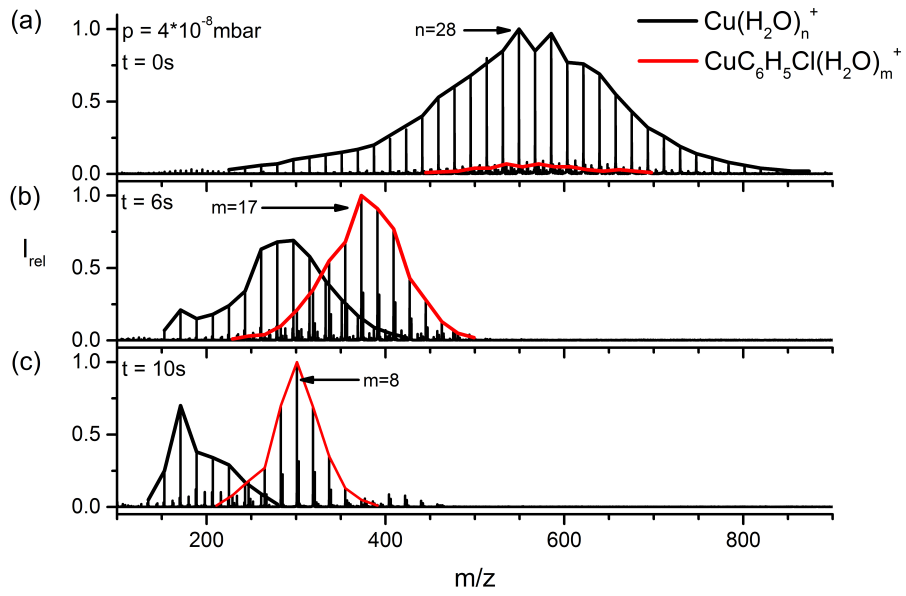

Figure 5.1.: Mass spectra of the reaction of $[Cu(H_2O)_n]^+$ with C_6H_5Cl at a pressure of 4 x 10^{-8} mbar after 0 (a), 6 (b) and 10 (c) s. Quantitative formation of $[CuC_6H_5Cl(H_2O)_m]^+$ is observed. The smaller peak next to the product peak is $[CuC_6H_5{}^{37}Cl(H_2O)_m]^+$. Furthermore dimers $[Cu_2(H_2O)_n]^+$ and also at 10 seconds $[Cu_2C_6H_5Cl(H_2O)_m]^+$ peaks are present.

and the product is the dehydrated $[Cu(C_6H_5Cl)_2{}^+]$. After long reaction delay (250 s) the decrease of the product intensity is observed due to the increase of the signal-to-noise ratio at the relatively high pressure. Bauschlicher et al. [127] performed ab initio calculations for the binding energy of one and two H_2O molecules with the first row transition metal cations and showed that the bonding is enhanced by hybridization of the 4s and 3d orbitals of Cu^+, resulting in a twofold linear coordination which is not unusual for Cu(I) complexes. [90] This was already observed for copper for the ligand exchange with acetonitrile. The kinetic and nanocalorimetric plots are shown in figure 5.2.

There is a fluctuation in the measured relative intensity based on the difficulty to keep the pressure of the reactant constant at the relatively high pressure regime. The determined reaction rates are summarized in table 5.1. $[Cu(H_2O)_n]^+$ is reacting slowly with the benzene compounds, therefore the measurements were done at relatively high pressure.

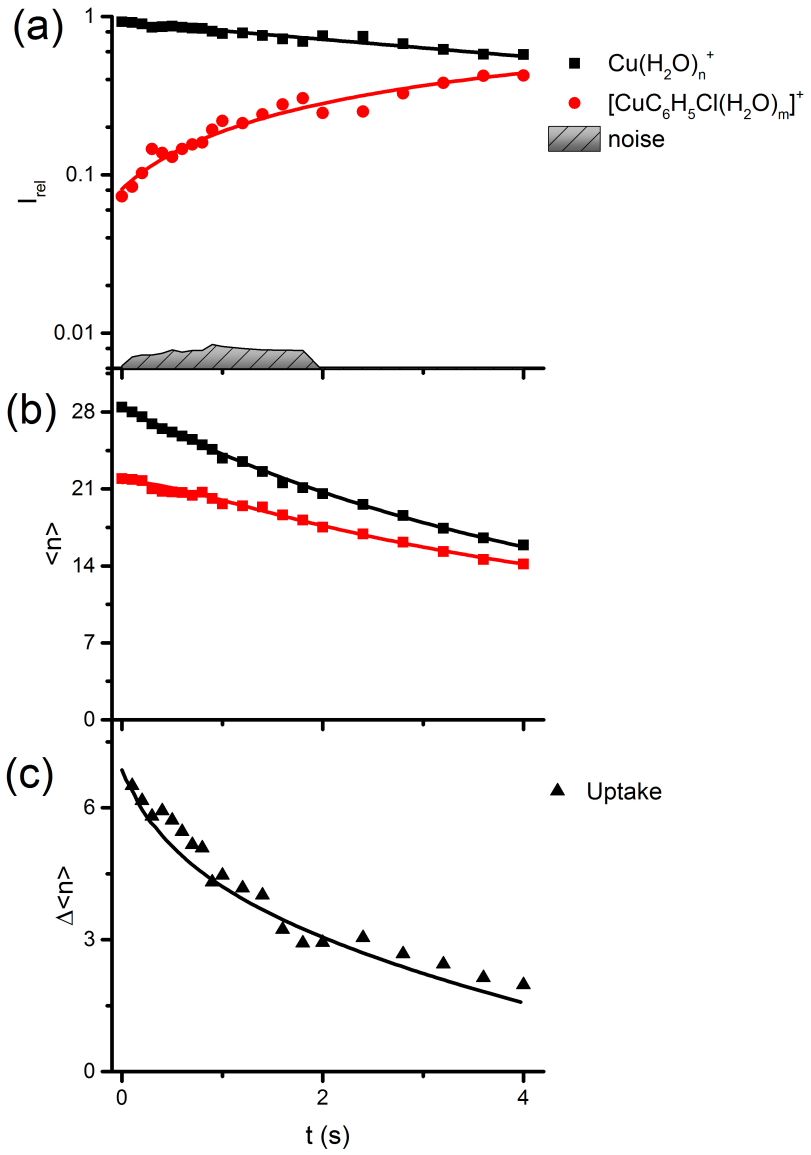

Figure 5.2.: Kinetics (a), average cluster size <n> (b) and difference of the cluster size Δ<n> (c) of the reaction of $[Cu(H_2O)_n]^+$ with C_6H_5Cl at a pressure of 4 x 10^{-8} mbar. The fits agree well with the measured average cluster size of the reaction.

Jones and Staley [112] and Bjarnason [128] studied the reaction of bare Cu^+ ions with C_6H_5Cl in the gas phase. Both groups observed the uptake of chlorobenzene molecule forming $Cu(C_6H_5Cl)^+$. The rate constant 2.3 x 10^{-10} cm^3 $molecule^{-1}$ s^{-1} for the uptake at 6.5 x 10^{-1} mbar determined from Jones and Staley [112] is in a similar range with the current reaction constant. The reaction of the bare Cu^+ is faster due to the absence of the water ligands. Additionally they observed the second uptake of chlorobenzene which is consistent with our measurements.

Table 5.1.: Absolute reaction rates of the reaction of $[Cu(H_2O)_n]^+$, n= 15-40, with C_6H_5Cl, C_6H_5Br and C_6H_5I.

	k_{abs}/cm^3s^{-1}
C_6H_5Cl	$1.57*10^{-10}$
C_6H_5Br	$1.76*10^{-10}$
C_6H_5I	$3.25*10^{-11}$

The small clusters react faster than the larger one due to the trend of the difference of the cluster size and the corresponding fit. Both for the large and for the small clusters the difference fit differs from the data points. With decreasing cluster size the probability of reaching the free copper coordination site increase. Therefore the value for the reaction of chlorobenzene is not fully reliable due to the difference of the reactivity for small and large clusters. The nanocalorimetric results are summarized for copper in table 5.2.

Table 5.2.: Results of Nanocalorimetric Analysis of the Reaction of $[Cu(H_2O)_n]^+$ with C_6H_5Cl, C_6H_5Br and C_6H_5I.

	ΔN_{vap}	ΔE_{nc}/ kJ mol^{-1}
C_6H_5Cl	*4.7* ± 0.7	*-199* ± 34
C_6H_5Br	*3.1* ± 0.6	*-131* ± 28
C_6H_5I	0.002 ± 0.5	4 ± 22

Reaction with bromobenzene. For the reaction of hydrated $[Cu(H_2O)_n]^+$ ions with bromobenzene the stepwise ligand exchange of up to four molecules was observed. The mass spectra are summarized in the supporting information A.3.

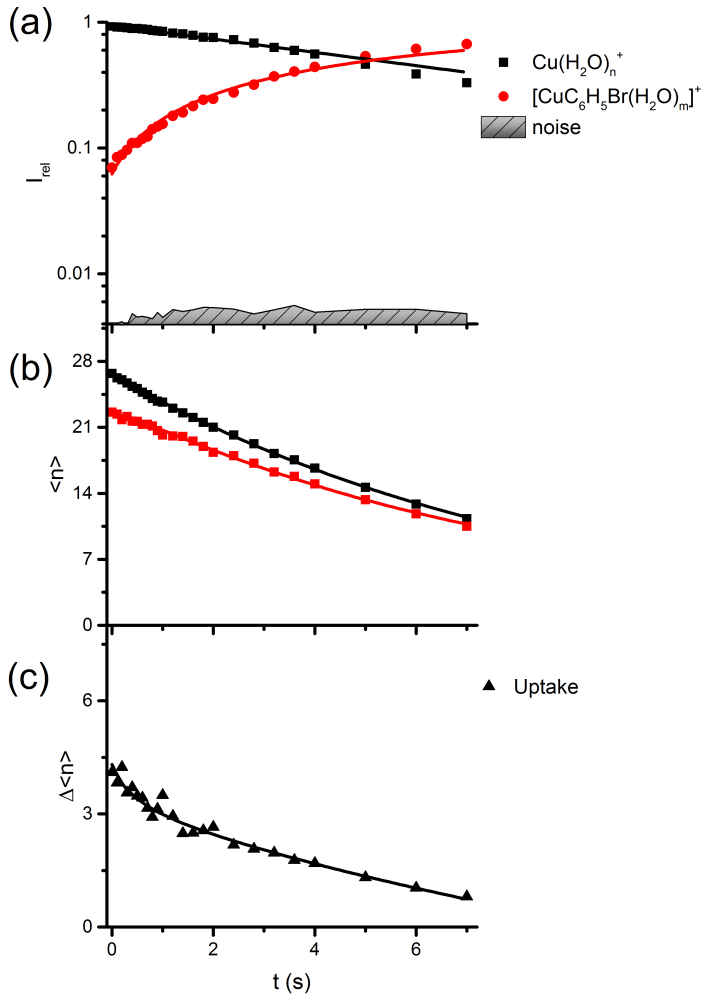

Figure 5.3.: Kinetics (a), average cluster size <n> (b) and difference of the cluster size Δ<n> (c) of the reaction of $[Cu(H_2O)_n]^+$ with C_6H_5Br at a pressure of 4 x 10^{-8} mbar. The kinetics show the ligand exchange of bromobenzene with pseudo–first–order behavior.

After 5 seconds reaction delay 50 % of the hydrated metal clusters reacted by ligand exchange to $[CuC_6H_5Br(H_2O)_m]^+$. At 14 s reaction delay the formation of $[Cu(C_6H_5Br)_4]^+$

is evident. The loss of the bromobenzene molecule can be observed at longer delays and $[Cu(C_6H_5Br)_2]^+$ is the product of the reaction. This is consistent with theoretical calculations which attributed the anomaly 4s-3d hybridization in Cu^+. [89,129] Thereof the stability of the twofold coordination follows. Furthermore it is also consistent with the observations with chlorobenzene and acetonitrile.

The kinetic and nanocalorimetric analysis are shown in figure 5.3. With bromobenzene no strong fluctuations of the pressure occured, therefore the fluctuation of the intensity is less present in comparison with chlorobenzene.

Ligand exchange of bromobenzene follows pseudo-first-order behavior and the rate constant is in the same range as for chlorobenzene. Further the behavior of the average cluster size fits show cluster size dependence. It seems that the exothermicity is decreasing with decreasing average cluster size. Therefore the determined nanocalorimetric values are not fully reliable. However, in comparison the average cluster size of product and educt is for the uptake of chlorobenzene more exothermic and cluster size dependent. Since chlorobenzene solves slightly better in water than bromobenzene the uptake is more preferred. Our results are consistent with the results of Bjarnason. [128] They obtained the uptake of bromobenzene for bare Cu(I) ions.

Reaction with iodobenzene. Ligand exchange of up to three iodobenzene molecules were observed for the reaction with $[Cu(H_2O)_n]^+$. The mass spectra are shown in the supporting information A.3. At nominally zero seconds reaction delay the first product peaks appear. The increase of the product intensity is very low, even at 5 s only one third of the product has reacted. After 7 s reaction delay the uptake of a second reactant molecule and at 14 s the third one was observed. Loss of the third iodobenzene molecule is noticed at longer reaction delays. The directly coordinated $[Cu(C_6H_5I)_2]^+$ is product of the reaction.

The kinetic analysis, shown in figure 5.4, confirms the observation that the reaction between $[Cu(H_2O)_n]^+$ and iodobenzene is the slowest one. The values are scattering due to the difficulty to hold the reactant pressure constant since iodobenzene has the lowest vapor pressure [83] of the used chemicals, which complicates the measurement. The reaction rate is smaller than the others by an order of magnitude.

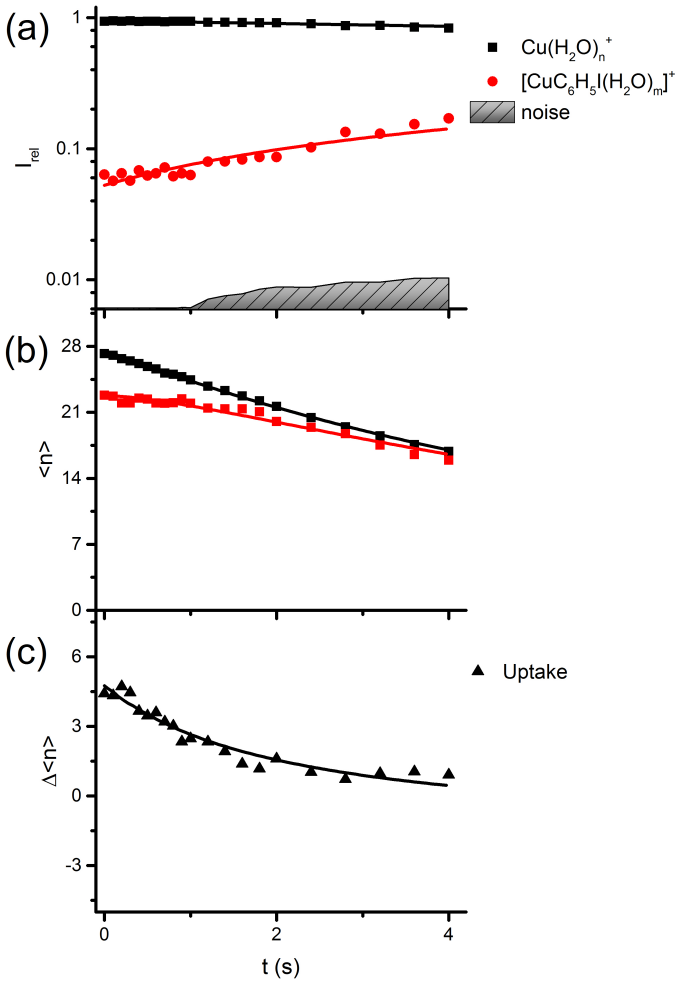

Figure 5.4.: Kinetics (a), average cluster size <n> (b) and difference of the cluster size Δ<n> (c) of the reaction of $[Cu(H_2O)_n]^+$ with C_6H_5I at a pressure of 5 x 10^{-8} mbar. The reaction proceeds very slowly with pseudo-first-order behavior.

This is in good agreement with the nanocalorimetric results, because the average number of water molecules which are evaporating due to the reaction is very low. This is consistent with the difference of the cluster size, since after the first two seconds, in which the accumulation takes place in the measurement cell, the difference values are constant. Consequently the uptake of iodobenzene is weakly exothermic.

Zinc. *Reaction with chlorobenzene.* The reaction of $[Zn(H_2O)_n]^+$ with chlorobenzene did not appear in the pressure region of 10^{-9} mbar and at 10^{-8} mbar a reaction is observed at 30 s, when the educt clusters have reached a size of n = 3-5 water molecules. The determination of the reaction rate for this pressure is not possible. For 4 x 10^{-7} mbar the reaction with $C_6H_5^\bullet$ is observed, shown in equation 5.5. Due to the relatively high pressure the reaction could be only studied for the first 6 seconds. This reaction was only observed for chlorobenzene and monovalent zinc ions.

$$[Zn(H_2O)_n]^+ + C_6H_5Cl \longrightarrow [ZnC_6H_5(H_2O)_m]^+ + (n-m)\ H_2O + Cl^\bullet \qquad (5.5)$$

The mass spectra are shown in figure 5.5. Due to the relatively high pressure the educt clusters have less water molecules than for the other reactions. Product peaks with $C_6H_5^\bullet$ are observed at nominally 0 seconds. The intensity of $[ZnC_6H_5(H_2O)_m]^+$ is increasing slowly until the signal is lost. Scattering of the intensity due to the pressure variations could not be avoided.

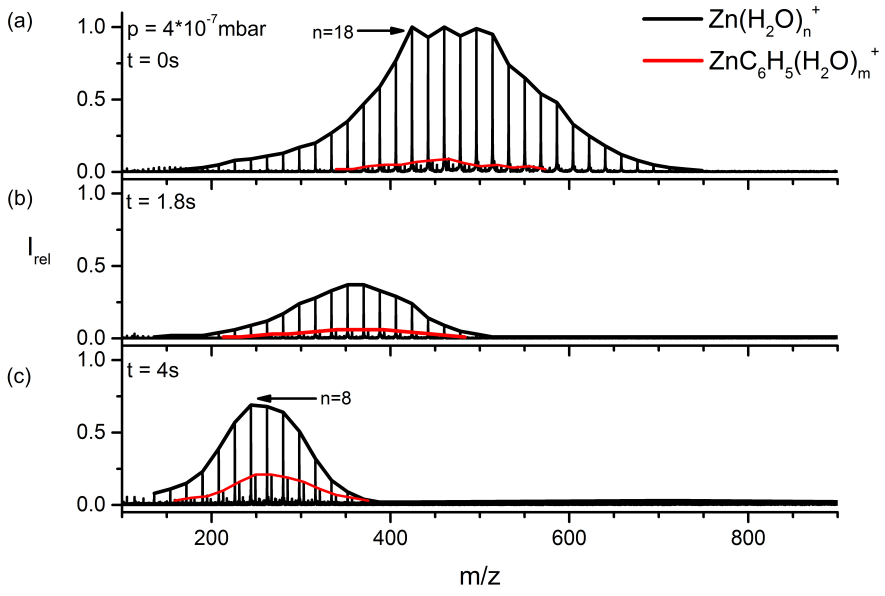

Figure 5.5.: Mass spectra of the reaction of $[Zn(H_2O)_n]^+$ with C_6H_5Cl at a pressure of 4 x 10^{-7} mbar after 0 (a), 1.8 (b) and 4 (c) s. Reaction with $C_6H_5^\bullet$ was observed. Small peaks of the dimers zinc water clusters are present.

The kinetic and nanocalorimetric plots are shown in figure 5.6.

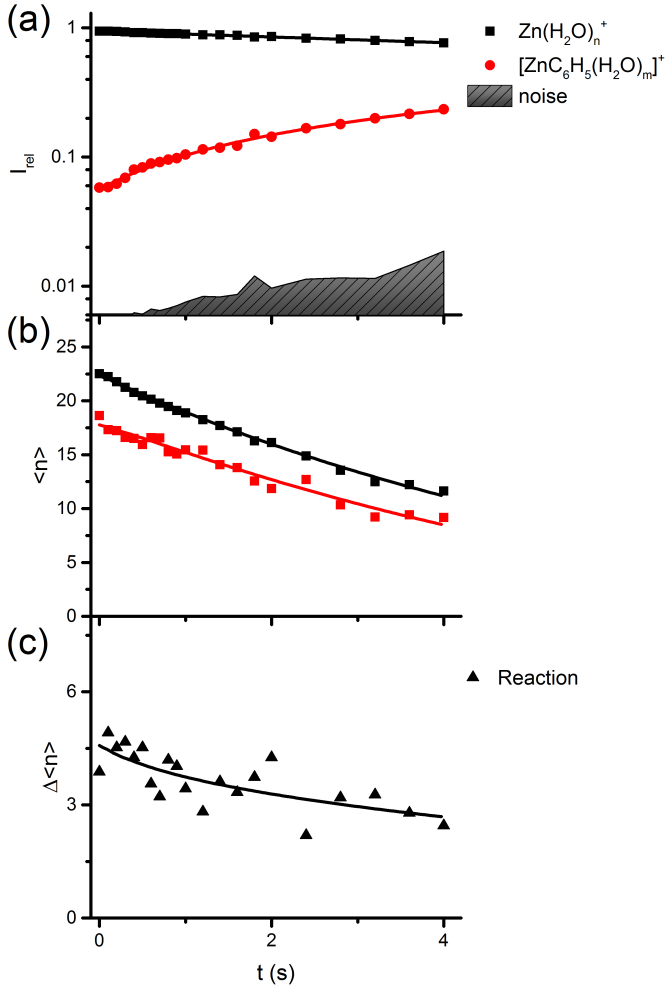

Figure 5.6.: Kinetics (a), average cluster size <n> (b) and difference of the cluster size Δ<n> (c) of the reaction of $[Zn(H_2O)_n]^+$ with C_6H_5Cl at a pressure of 4 x 10^{-7} mbar for the first 4 seconds. The kinetic fits follow a pseudo first order behavior. Scattering of the relative intensity and average cluster size depends on the pressure.

The measured values for the relative intensity and for the average cluster size is scattering, because the pressure had to be adjusted several times and the intensity of the educt clusters is low. The determined reaction rates (table 5.3) are consistent with the observation, that this reaction is the slowest one.

Table 5.3.: Absolute reaction rates of the reaction of $[Zn(H_2O)_n]^+$, n= 15-40, with C_6H_5Cl, C_6H_5Br and C_6H_5I.

	k_{abs}/cm^3s^{-1}
C_6H_5Cl	$7.69*10^{-12}$
C_6H_5Br	$1.08*10^{-10}$
C_6H_5I	$2.64*10^{-10}$

However, this reaction is also the most exothermic (see table 5.4) one. The average loss of 4 water molecules is observed for the reaction with the radical $C_6H_5^{\bullet}$. However, the value is not fully reliable, since at this pressure the requirements for the nanocalorimetry are not fulfilled.

Table 5.4.: Results of Nanocalorimetric Analysis of the Reaction of $[Zn(H_2O)_n]^+$ with C_6H_5Cl, C_6H_5Br and C_6H_5I.

	ΔN_{vap}	ΔE_{nc}/ kJ mol^{-1}
C_6H_5Cl	*3.9* $\pm$ 0.5	*-163* $\pm$ 25
C_6H_5Br	*0.5* $\pm$ 0.7	*-18* $\pm$ 30
C_6H_5I	1.1 $\pm$ 0.5	-41 $\pm$ 22

A possible mechanism for the formation of $ZnC_6H_5^+$ could be the oxidative addition of Zn(I) via a nucleophilic attack to the carbon atom of chlorobenzene as shown in scheme 5.1.

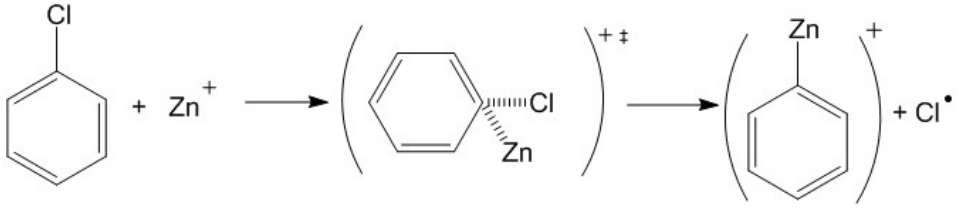

Scheme 5.1: Addition of Zn^+ via nucleophilic attack and insertion into the C_6H_5-Cl bond.

The ground state of Zn^+ has the electron configuration $3d^{10}4s^1$ and an organic metallic bond formation is possible. This was confirmed by the geometry optimization with DFT shown in figure 5.7.

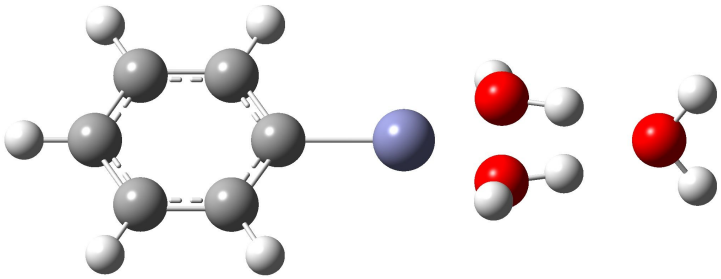

Figure 5.7.: Optimized structure of $[ZnC_6H_5(H_2O)_3]^+$.

A heterolytic cleavage of the carbon-chloride bond followed by an electron transfer is unrealistic, due to the high electronegativity of chlorine. [83] To our knowledge the observed reaction has not yet been published. Although the insertion of zinc dust into benzyl halides was reported [130,131], but at the end of the reaction there was always a product with the halides and not with the aryl part. Egorov et al. [130] studied the reaction of zinc powder with benzyl halides in DMF with low-temperature ESR-spectroscopy. The results show that reaction of zinc with benzyl bromide and benzyl iodide form benzyl radicals. For benzyl chloride additionally the formation of ion-radical pairs $RX^{-\bullet}$-$Zn^{\bullet}$ at 77 K was determined. It confirms that the formation of organozinc halides is possible from benzyl derivate, but the reaction depends on the type of halogen. Additionally Hoshi et al. [132] observed the electrolysis of chlorobenzene using naphthalene as a mediator only for Ag, Zn and Pt electrodes. For Cd, Sn and In such a behavior was not observed. These examples show the dependency of the relevant reactants on the formation of the product.

Reaction with bromobenzene. Hydrated monovalent zinc cations $[Zn(H_2O)_n]^+$ react with bromobenzene by formation of $[ZnBr(H_2O)_m]^+$. The mass spectra are shown in the supporting information A.3. For small clusters $[Zn(H_2O)_n]^+$, $n_{max} \leq 6$, a further reaction (5.7) was observed after 18 s reaction delay.

$$[Zn(H_2O)_n]^+ + C_6H_5Br \longrightarrow [ZnBr(H_2O)_m]^+ + (n-m)\ H_2O + C_6H_5^{\bullet} \qquad (5.6)$$

$$[Zn(H_2O)_n]^+ + C_6H_5Br \longrightarrow [ZnC_6H_5Br(H_2O)_l]^+ + (n-l)\ H_2O;\ l \leq 3 \qquad (5.7)$$

After 30 s the uptake of a second bromobenzene molecule is developed for both products (see supporting information A.3). Due to the relatively high pressure and impurities of ammonia the product of the reaction could not be observed at long reaction delays.

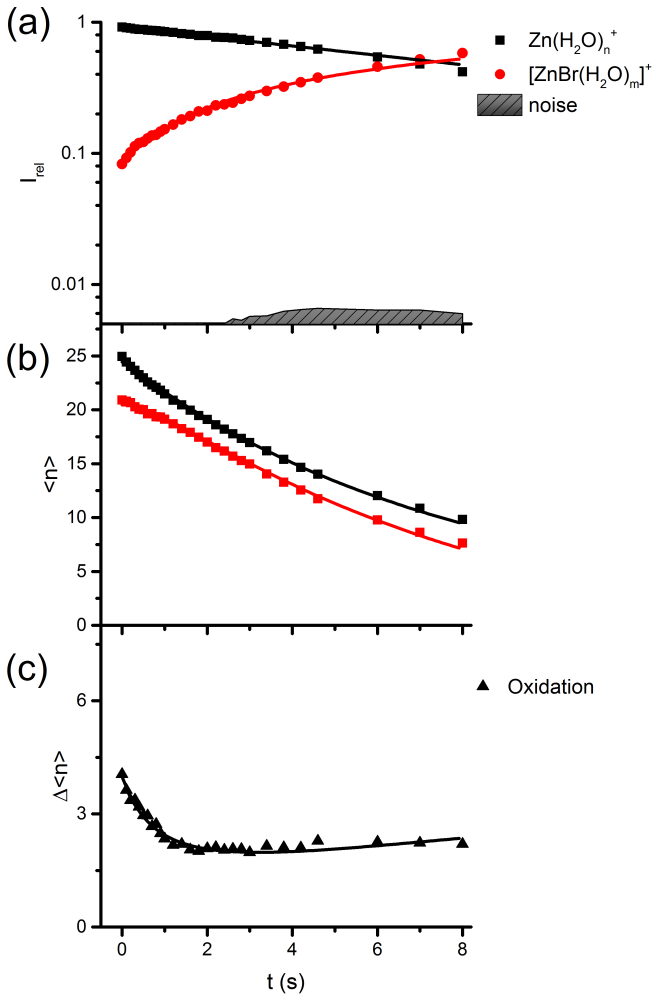

Figure 5.8.: Kinetics (a), average cluster size <n> (b) and difference of the cluster size Δ<n> (c) of the reaction of $[Zn(H_2O)_n]^+$ with C_6H_5Br at a pressure of 4.4 x 10^{-8} mbar for the first 8 seconds. The kinetic fits follow a pseudo first order behavior.

As shown in figure 5.8 the reaction with bromobenzene is dependent on the cluster size. The smaller clusters are reacting with higher reactivity due to the increasing of the average number of loss water molecules in the last 2 seconds. The reason could be that for smaller clusters the polarization of the metal core by bromobenzene is favored due to the smaller solvation shell. It is consistent with the observations since only for

small clusters a ligand exchange was observed. In contrast to chlorobenzene no product $ZnC_6H_5^+$ was observed. Guijaro et al. [114] analyzed the reaction of activated zinc with organic bromides. In the case of aryl halides, there Hammett plots are consistent with the participation of aryl halides radical anions as intermediates of the reaction. They assume an oxidative addition via a radical anion intermediate like in reaction equation 5.8 [114]

$$\begin{aligned} Zn_{(s)} + Br - Ar \rightleftharpoons [Zn_{(s)}Br - Ar \leftrightarrow Zn^+_{(s)}[Br - Ar]^{\bullet -}]^{\ddagger} \rightarrow \\ Zn^+_{(s)}Br^- + Ar^{\bullet} \rightleftarrows RZnBr \end{aligned} \tag{5.8}$$

Since the electron configuration of Zn^+ is $3d^8 4s^1$ an oxidative addition by forming Zn^{2+} and Br^- is possible. Perhaps the reaction with chlorobenzene is different due to a variable mechanism or is activated by collision because of the higher pressure.

Reaction with iodobenzene. Also with iodobenzene the reaction with the halide was observed (shown in supporting information). After 18 s reaction delay also the ligand exchange of the iodobenzene molecule is determined, but the intensity of the ligand exchange product is located in the noise level and does not increase significant.

$$[Zn(H_2O)_n]^+ + C_6H_5I \longrightarrow [ZnI(H_2O)_m]^+ + (n-m)\ H_2O + C_6H_5^{\bullet} \tag{5.9}$$

$$[Zn(H_2O)_n]^+ + C_6H_5I \longrightarrow [ZnC_6H_5I(H_2O)_l]^+ + (n-l)\ H_2O;\ l \leq 2 \tag{5.10}$$

After 15 seconds reaction delay an uptake of iodobenzene of the primary product is noticed:

$$\begin{aligned} [ZnI(H_2O)_m]^+ + (1-3)C_6H_5I \longrightarrow [ZnI(C_6H_5I)_{1-3}(H_2O)_k]^+ + \ (m-k)H_2O; \\ for\ 1\ C_6H_5I\ k \leq 6 \end{aligned} \tag{5.11}$$

The reaction is faster than the reaction with bromobenzene shown in the kinetic analysis in figure 5.9. Furthermore it is not dependent on the cluster size as with bromobenzene. The oxidation of the metal core by iodide permits further reactions, whereby ligand exchange of the iodobenzene and formation of $[ZnI(C_6H_5I)_{1\text{-}3}(H_2O)_k]^+$ is observed (shown in supporting information). For the oxidation vaporization of one water molecule is determined.

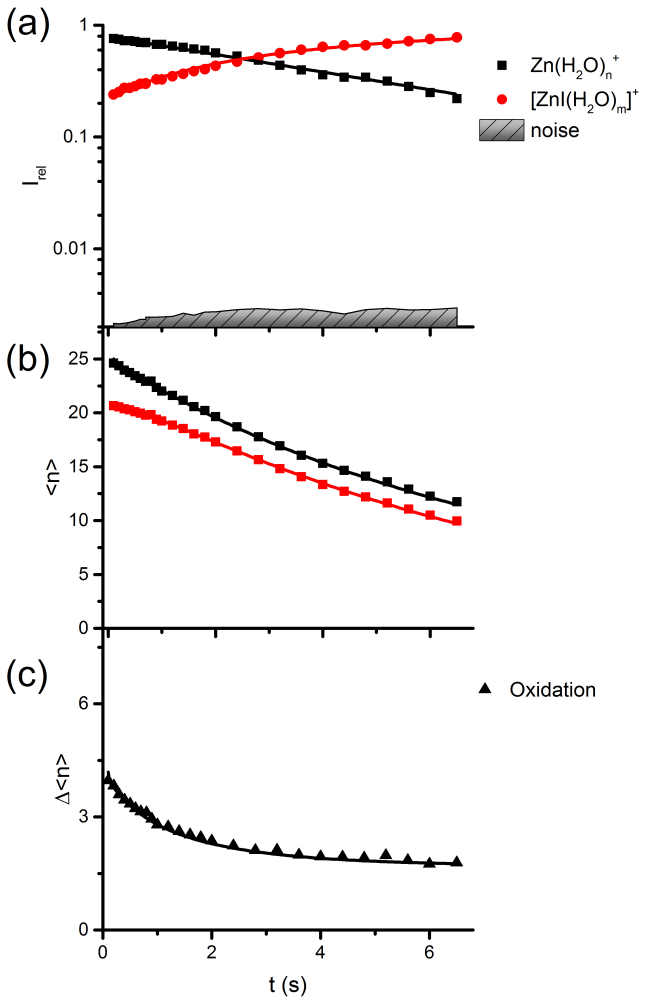

Figure 5.9.: Kinetics (a), average cluster size <n> (b) and difference of the cluster size Δ<n> (c) of the reaction of $[Zn(H_2O)_n]^+$ with C_6H_5I at a pressure of 4.5 x 10^{-8} mbar for the first 6.5 seconds. The kinetic fits follow a pseudo first order behavior.

5.4. DFT calculations

To investigate whether the differences of the reaction of the monovalent zinc cations have thermodynamic reasons DFT calculations were performed for the bare zinc ion and for a model system with three water molecules $Zn(H_2O)_3^+$. Duncan et al. [65] showed that the

direct coordination of $[Zn(H_2O)_n]^+$ is completed with three water molecules, whereas the n = 4 complex has one external water in a double-acceptor site. The reaction enthalpy was calculated for the reaction with ZnX^+ or $ZnC_6H_5{}^+$ as product and is summarized in table 5.5.

Both systems are consistent to the results that no reaction takes place with fluorobenzene. The reaction is endothermic and requires at least 70 kJ/mol for the activation. Thermodynamically the formation of ZnX^+ is not preferred under waterless conditions, because the ionic compound is stabilized by the water molecules. However the formation of $ZnC_6H_5{}^+$ is more favored for the gas phase reaction, since the solubility of the organic part is negligible. The reactivity is increasing with increasing of the atomic number, because the binding energy of C-X is decreasing.

Table 5.5.: Reaction enthalpy for the possible reactions in the gas phase without water molecules and for a small system $Zn(H_2O)_3{}^+$.

ΔH_f kJ/mol	ZnX^+	$ZnX(H_2O)_3{}^+$	$ZnC_6H_5{}^+$	$ZnC_6H_5(H_2O)_3{}^+$
F	247.7	70.8	202.8	206.7
Cl	138.3	7.1	64.9	68.8
Br	96.1	-10.3	12.3	13.4
I	51.6	-22.5	-38.6	-34.7

Due to the presence of the water molecules the reactivity is changing in favor of the ionic compounds and not the metallo-organic coupling. This is consistent with our investigation and the observation that ions dissolve better in protic solvents like water.

The optimized geometry for the product $ZnX(H_2O)_3{}^+$ is shown in figure 5.10. Due to the negative charge is located on the halide the water molecules are arranged on the opposite side of the cluster and the third water molecule is in the second solvation shell. The distance between the Br^- and Zn^{2+} is 2.21 Å. In contrast the bond between the hydrated Zn(I) and the C atom is 1.93 Å long. This corresponds with the bond lengths in organometallic compounds with Zn determined by X-Ray and neutron diffraction. [133] The difference of the bond lengths of the two products depends on the different type of bonds and also on the size of the atoms, since the bromine atom has a larger radius than the carbon atom.

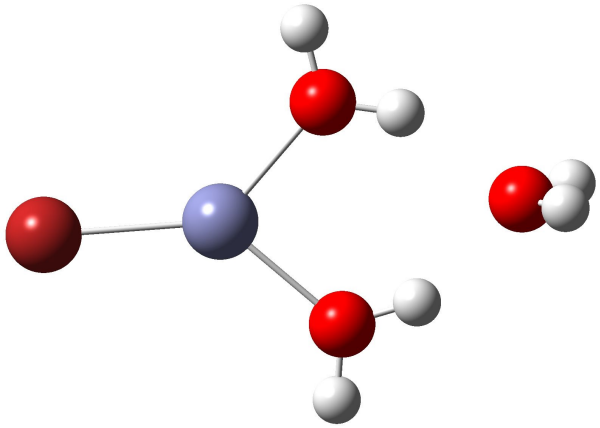

Figure 5.10.: Optimized geometry of $[ZnBr(H_2O)_3]^+$.

The formation of the metallo organic $ZnC_6H_5^+$ is only favored for iodine molecules, but is not observed in our measurements. However, the formation of $ZnC_6H_5^+$ with chlorobenzene is highly endothermic for both systems and proceeds not thermodynamically. The energy barrier for the reaction may be lower.

5.5. Discussion

Hydrated monovalent $[Cu(H_2O)_n]^+$ cations are not reacting with fluorobenzene and only by ligand exchange with the other observed organic compounds. As in table 5.6 shown fluorobenzene has the highest bond dissociation energy, thus the bond is very stable and more energy is required for breaking the bond. The bond dissociation energy is decreasing with increasing atomic number from fluorine to iodine, hence the electronegativity is decreasing.

None of the determined enthalpies reach the required energy for dissociation and a possible reaction with the halide. The uptake of fluorobenzene is not observed; hence the high electronegativity of fluorine prevents the charge distribution.

The reaction with iodobenzene is the slowest one since iodobenzene has the lowest aqueous solubility, hence it is rather insoluble in water. Therefore energy is required for the solvation and the ligand exchange is endothermic. Reaction rates of the ligand

Table 5.6.: Comparison between the bond dissociation energies (BDE) [83] of the aryl halides and the determined nanocalorimetry enthalpies for the reaction with $[Cu(H_2O)_n]^+$. Aqueous solubility (S) [83] of the organic compound in units of grams per one kilogram of water.

	BDE (kJ/mol)	ΔE_{nc} (kJ/mol)	S (g/kg H_2O)
C_6H_5-F	525 ± 8.4		1.7
C_6H_5-Cl	399.6 ± 6.3	-199	0.59
C_6H_5-Br	336.4 ± 6.3	-131	0.387
C_6H_5-I	272 ± 4.2	4	0.193

exchange of the other molecules are located in the same range since the solubility is increasing. Reaction with C_6H_5Cl has the highest enthalpy, which can be a possible intramolecular cluster reaction, but the energy is not high enough for the dehalogenation. It is well known that bare Cu^+ ions are reacting with alkyl halides by dehalogenation and formation of CuX^+, but with aryl halides no reactions or only ligand exchange was investigated. [8] There are some copper promoted couplings, where copper inserted in a C-I-bond like Ullmann coupling. [134] Moreover the Chan-Lam coupling [135] proceeds through a heterocycle copper(III) intermediate complex.

Zhang et al. [136] studied the mechanism of amination reactions between aryl bromides and alkyl amines catalyzed by Cu(I) species with ligands with theoretical calculations. They observed that for an acidic substrate a neutral ligand is preferred, while for a basic substrate an acidic ligand is necessary for achieving high efficiency. Therefore the combination of ligands and base or acid for a specific nucleophile is important for the success of the reaction.

According to the hard and soft acids and bases (HSAB) [116] principle Zn^+ is a soft acid. Based on the principle soft acids are forming stable complexes with soft bases. Soft molecules, ions and atoms have a large radius and a low charge. Therefore the product $ZnC_6H_5^+$ is preferred, because it is a combination of a soft acid and bases, since chlorine is a hard bases. On the other hand iodine is a soft bases and the ZnI^+ product is favored. The principle is based on empirical observations and does not apply for all reactions. However, Zn is used in the organometallic chemistry as a soft nucleophile.

Hydrated Zn(I) cations are showing an interesting chemistry with the selected organic compounds. However a reaction with fluorobenzene is not observed. While only with chlorobenzene the reaction with $C_6H_5^{\bullet}$ is observed, Zn(I) is reacting with the halide with the bromine and iodine compounds.

There are few examples where such differences were also observed. Uppal et al. [119] analyzed the chemistry of Ti^+ ion with halomethanes, alkyl chlorides, chloroethylenes and chlorobenzene in the gas phase. Only for the reaction with chlorobenzene no formation of $TiCl^+$ was determined. Ti^+ dehydrochlorinates chlorobenzene by eliminating HCl and formation of $TiC_6H_4{}^+$. Bare Fe^+ cations reacting mainly with aryl halides by dehydrohalogenation and formation of $FeC_6H_4{}^+$. [121,137] Only with iodobenzene ions are reacting with $C_6H_5^{\bullet}$ by the formation of $Fe(C_6H_5)_2{}^+$. Bjarnason et al. [137] determined lower bond energy for Fe^+-C_6H_5 as for Fe^+-C_6H_4, which is higher by 18 kcal/mol. [137] Maybe the higher bond energy of Fe^+-C_6H_4 depends on a positive inductive effect of the iron, since Fe^{3+} is favored. [116] It seems that for some compounds and metal ions the formation of metall organic compounds is exothermic.

Our observation could be the first step for the polymerization of $C_6H_5^{\bullet}$ in the cluster like Fe^+ does. Because zinc metal organic reagents are taken to synthesize functionalized diaryl compounds by halide-zinc exchange. [138,139] However, due to the high pressure a study for long reaction delays was not possible. Fisher et al. [104,140] analyzed the reaction of Co^+ and Ni^+ with CH_3CX (X = Cl, Br and I) by guided ion beam and observed the formation of $MCH_3{}^+$ and MX^+. They assumed that at low energies an intermediate complex is formed by insertion of the metal ion into the C-X bond. Therefore both products can be observed. At high energies a direct mechanism followed by the reaction with the halide takes place.

DFT calculations of the thermochemistry for the Zn^+ reactions show the high influence of the water molecules. While the formation of the metallo organic compound is preferred in the gas phase, it changes in aqueous environment. On the one hand it depends on the solubility of the chemicals; hence benzene has a low solubility of 1.77 g/kg H_2O (for 30°C) and is in aprotic environment better soluble. In contrast for example ZnI_2 has a high solubility of 43.8 g/kg H_2O. [83] On the other hand the water molecules stabilize the ionic bond with the hydrogen bonds. The formation of $ZnC_6H_5{}^+$ with chlorobenzene

is not preferred due to the thermodynamically calculations. Therefore a lower energy barrier for this reaction and a kinetically preferred product is assumed.

Supporting Information

Figures with mass spectra for the reaction of hydrated Cu(I)/Zn(I) with C_6H_5Br and C_6H_5I. In addition the mass spectra for the reaction of $[Zn(H_2O)_n]^+$ with C_6H_5Br and C_6H_5I at 30 s reaction delay.

6. Theoretical study of geometry, IR and UV/VIS spectra for $V(H_2O)_n^+$, n = 8-12, relevant for the water activation pathways during room temperature blackbody infrared radiative dissociation (BIRD)

6.1. Introduction

Hydrated monovalent vanadium ions are object of different experimental and theoretical studies. [141–143] V(II) and V(III) are characterized in aqueous solutions, while V(I) is not stable in solutions. [144] Walker et al. [143] measured the infrared spectra of Ar-tagged $V(H_2O)_1^+$ and Rosi and Bauschlicher [127,129] characterized $V(H_2O)_1^+$ and $V(H_2O)_2^+$ with ab initio calculations. Sasaki et al. [144] studied $[V(H_2O)_n]^+$, n = 2-8, with infrared photodissociation spectroscopy and the help of theoretical calculations. They suggest that $d_{x^2-y^2}$ is the empty orbital, which provides four sites of lower energy density along the x and y axes. Ugalde et al. [141] characterized the reaction of water with first row transition metal ions. They determined for V^+ the elimination of molecular hydrogen by the change of the spin configuration from quintet to triplet. Furthermore Silica et al. [145] observed the spin change for the reaction of monovalent vanadium cations with ammonia.

FT-ICR mass spectrometry experiments of $[V(H_2O)_n]^+$, n = 5-30, with room temperature blackbody radiation show not only the loss of water molecules, also redox reactions are observed. [41] The loss of atomic and molecular hydrogen followed by the oxidation and formation of $[V(II)OH(H_2O)_m]^+$ and $[V(III)(OH)_2(H_2O)]_l^+$ is determined. Both reactions are strongly dependent on the cluster size. Specially for $[V(H_2O)_n]^+$, the elimination with low activation energies with n= 9 – 12 for atomic, and n= 9 – 23 for molecular hydrogen was observed. [41] The blackbody fragmentation provides a further tool for gently removing water ligands from an ionic cluster and allowing observations of the effect due to the loss of the stabilizing solvent.

Furthermore studies in our working group show that the reactions are not only cluster size dependent, it is also dependent on the geometry of the clusters. The reaction rates are different for clusters producing in the source or clusters, which are products of the blackbody infrared radiative dissociation. [146] First results of photodissociation of selected $[V(H_2O)_n]^+$, n = 1 – 4, clusters in an FT-ICR mass spectrometer with a high-pressure mercury lamp and bandpass filters show a characteristic photochemistry. [147]

To learn more about the electronic states and water activation pathways of hydrated monovalent vanadium ions, geometry optimization and calculation of IR and UV/VIS

spectra were done for $[V(H_2O)_n]^+$, n = 8 – 12. For this cluster range three reactions with different reactivity for every cluster are observed. First the fragmentation:

$$[V(H_2O)_n]^+ + hv_{IR} \rightarrow [V(H_2O)_{n\text{-}m}]^+ + m\ H_2O \tag{6.1}$$

with the lowest reactivity for $[V(H_2O)_{12}]^+$. Furthermore the loss of atomic hydrogen induced by the infrared photons, which is only observed at room temperature for $[V(H_2O)_{12}]^+$:

$$[V(H_2O)_n]^+ + hv_{IR} \rightarrow [VOH(H_2O)_{n\text{-}m\text{-}x}]^+ + x\ H_2O + H \tag{6.2}$$

At least the loss of molecular hydrogen with the highest reactivity for $[V(H_2O)_{12}]^+$:

$$[V(H_2O)_n]^+ + hv_{IR} \rightarrow [V(OH)_2(H_2O)_{n\text{-}m\text{-}x}]^+ + x\ H_2O + H_2 \tag{6.3}$$

Further reactions of the primary products are observed. This work is serving for the future photodissociation analysis of the clusters in our working group.

6.2. Computational methods

All quantum chemical calculations are performed with Gaussian 09 program package. [92] For vanadium the 6-311+G(2df), and for hydrogen and oxygen the 6-31+G(d) basis set is used. The geometries are optimized with the DFT/B3LYP theory and the local minimum character is verified by frequency calculations. Electronic absorption spectra are calculated by the time dependent density functional theory with the B3LYP functional for all geometries and for the first two most stable geometries with CAM-B3LYP. The molar attenuation coefficient σ, in units of cm^2, is calculated due to the direct relation [148] to the attenuation cross section ε via the Avogadro constant N_A:

$$\sigma = ln\frac{10^3}{N_A}\varepsilon \tag{6.4}$$

The attenuation cross section ε is determined by the theoretical calculations.

6.3. Results

For $[V(H_2O)_8]^+$ nine geometries were optimized, which are summarized in figure 6.1. The number of geometries was limited for all clusters to nine due to the high plurality of possible cluster geometries.

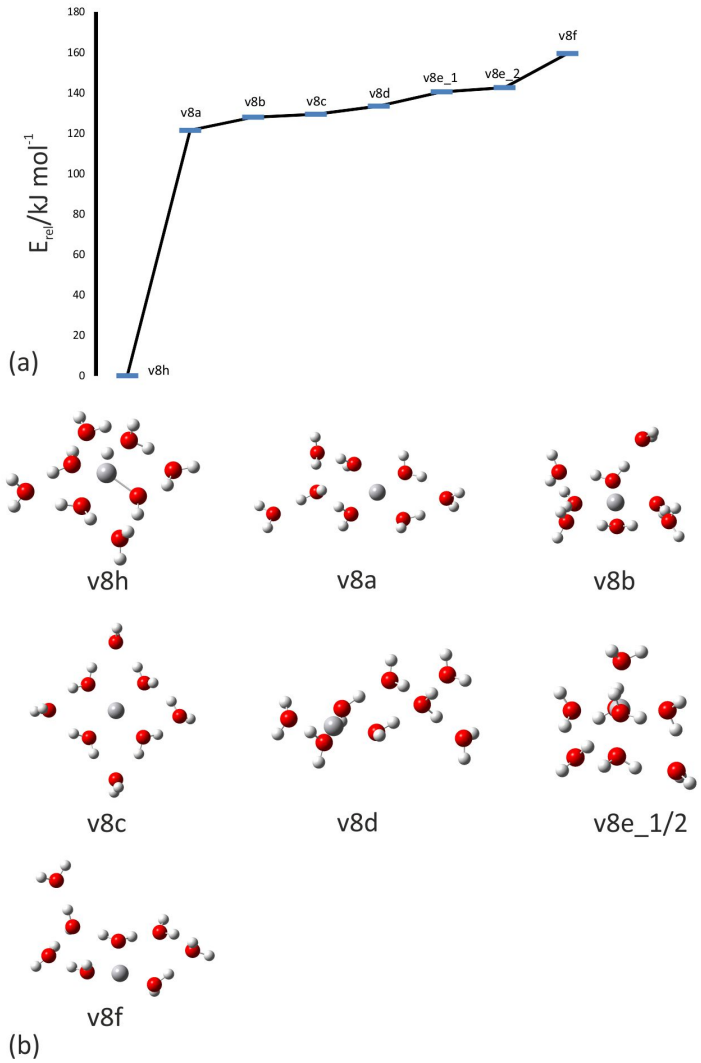

Figure 6.1.: Optimized geometries (b) of $[V(H_2O)_8]^+$ and the relative energy difference (a) to the most stable geometry with $[HVOH]^+$-core.

The most stable geometry is **v8h** with three water molecules and one hydroxide in the first solvation shell. This square is not planar, because the three water molecules are

tilted down. The proton is bound perpendicular two the vanadium with an angle of 108.2°. The remaining water molecules interact with to molecules of the first solvation shell and are arranged between them in the second solvation shell.

Geometry with a planar square or less tensed first solvation shell were not been determined. The energy of the most stable geometry (**v8a**) without the $[HVOH]^+$ core is 122 kJ/mol higher as the hydroxide geometry and has a square geometry with four water molecules in the first solvation shell. Further three water molecules interact with the first solvation shell water molecules, while the last molecule is bound by one of the second solvation shell.

The geometry of **v8b** has an 128 kJ/mol higher energy than the **v8h** cluster. The first solvation shell has the same geometry as **v8a**, but the second solvation shell consists of three water molecules, which are orientated at the edges of the square of the first solvation shell. One molecule is raised above this level and interacts by hydrogen bond only with one molecule of the first solvation shell.

Geometry **v8c** has a relative energy which is 130 kJ/mol higher than the hydroxide geometry. It differs to **v8b** by four water molecules are oriented in the edges of the square, but two of them protrude from the plane slightly. For **v8d** the first solvation shell is equal to that of the **v8a-c** and the energy is 134 kJ/mol higher. However, in the second solvation shell two water molecules interact with two hydrogen bonds of the first solvation shell water molecules. One of these water molecules forms a triangle with two further water molecules.

At **v8e_1/2** six water molecules are orientated in an octahedron in the first solvation shell and the remaining two water molecules interact with the top or down of the square water molecules. The geometries differ in the spin multiplicity, **v8e_2** has a triplet spin state, and slight variations in the angles. The energy difference between the two octahedron geometries is very small, 2.1 kJ/mol.

Frequency calculations were done for the calculated geometries to prove that there is not a transition state and to determine the differences between them. The spectra are shown in figure 6.2. For all clusters in the range of 3500 – 3900 cm^{-1} bands are caused by the symmetric and asymmetric valence vibrations of water. Immediately below until 3100 cm^{-1} are the bands assumed by the hydrogen bonds between the water molecules. At

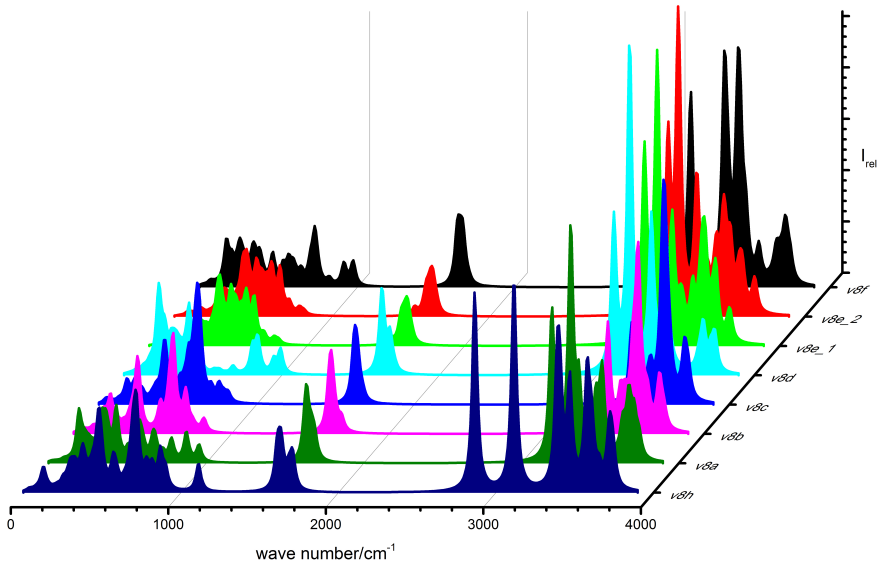

Figure 6.2.: Calculated infrared spectra of $[V(H_2O)_8]^+$. The spectra are ordered according to the relative energy; in the front the most stable one.

1650 – 1700 cm^{-1} there is mostly one band, which is assignable to the bending vibration of the water molecules. The region under 1000 cm^{-1} is the so called fingerprint region with further valence, bending and combination bands of the water molecules and of the whole cluster.

For the $[HVOH(H_2O)_7]^+$, three additional bands are determined. At 1130 cm^{-1} the hydroxide bending vibration is observed and at 1750 cm^{-1} a further band is observed, which is caused by the vibration of the proton to the vanadium ion. Additionally in the region of 3600 cm^{-1} hydroxide stretching bands occur. Furthermore a peak with high intensity is present at 2950 cm^{-1}, which is caused by a high stretching vibration of one hydrogen atom [1] to the opposite oxygen atom (see figure 6.3).

It seems that this hydrogen bond is weak and a mobile proton is present. Johnson et al. [149] investigated the vibrational spectra of hydrogen bonding in the first solvation shell of $MOH^+(H_2O)_n$, n = 1 – 5, (M = Mg, Ca). They observed a proton migration between the water molecule and hydroxide ion which is characterized by red-shift of the hydroxide stretching frequency. The studied systems were smaller than in this work;

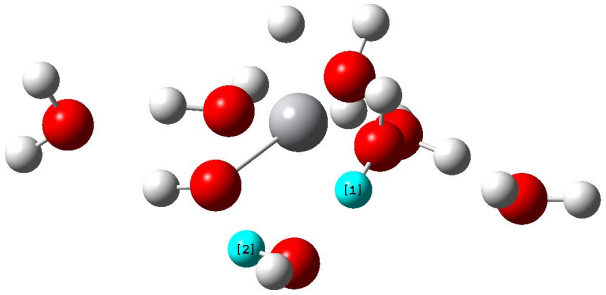

Figure 6.3.: O–H stretching modes, which cause the band at 2950 cm^{-1} [1] and at 3470 cm^{-1} [2].

however the stretching vibration is so intensive in their intensity and movement that it corresponds to a mobile proton. Even at 3470 cm^{-1} is a band, which is caused by the same vibration between the hydrogen [2] and the oxygen atom of the hydroxide. Thus a proton migration is possible, but proceeds through several water molecules.

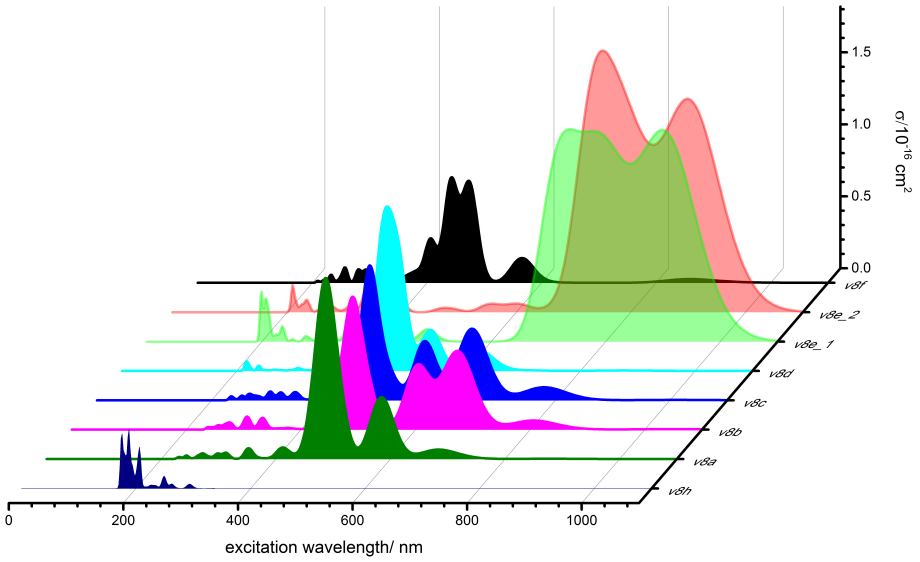

Figure 6.4.: Calculated UV/VIS spectra of $[V(H_2O)_8]^+$. The spectra are ordered according to the relative energy; in the front the most stable one.

Due to the different electronic structure of V(I) and V(III), absorption spectra were calculated in order to differentiate the geometries. These are summarized in figure 6.4.

The strongest absorption of $[HVOH(H_2O)_7]^+$ lies at 175 nm and is mainly caused by the transition between the molecular orbitals shown in figure 6.5.

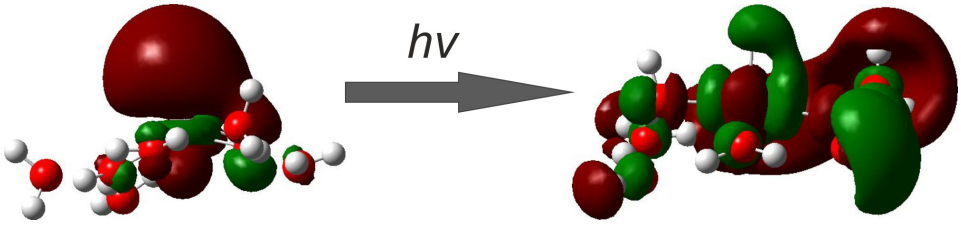

Figure 6.5.: Transition with highest calculated oscillator strength at 175 nm for **v8h**.

It is difficult to say in which orbital the electron is, hence the excitation to 3d4s for the bare metal ion V^{3+} needs 12.4 eV. [107] The excitation energy increases with increasing number of water molecules, therefore the transition takes place within the 3d orbitals.

For **v8a-c** the strongest absorption at 520 nm is the allowed $3d^3(^3F)4p \leftarrow 3d^4$ transition [107], known for the bare metal ion V^+. The weaker transitions at longer wavelengths are due to transitions corresponding to $3d^34s \leftarrow 3d^4$ and for the transitions within the $3d^4$ molecular orbitals. They are both parity forbidden for the bare metal ion, but the probability increases with increasing number of water molecules since interaction of the orbitals and more combination of the molecular orbitals occur. The representative molecular orbitals for the transition with the highest oscillator strength at 480.41 nm are shown in figure 6.6.

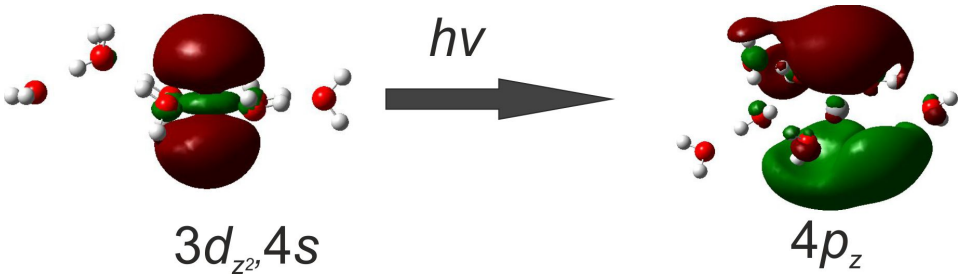

Figure 6.6.: Transition with highest calculated oscillator strength at 480.41 nm for **v8a**.

As shown the ground state molecular orbital is a linear combination of the vanadium $3d_{z^2}$ and 4s atomic orbitals. Furthermore the excited state molecular orbital corresponds to the vanadium $4p_z$. Surprisingly the spectra of the octahedron geometry barely differ,

although the electron configuration is different. Probably the geometry plays a stronger role, due to a preferred linear combination of the molecular orbitals. As mentioned before the hydroxide geometry is also the most stable one for $\mathbf{[V(H_2O)_9]^+}$.

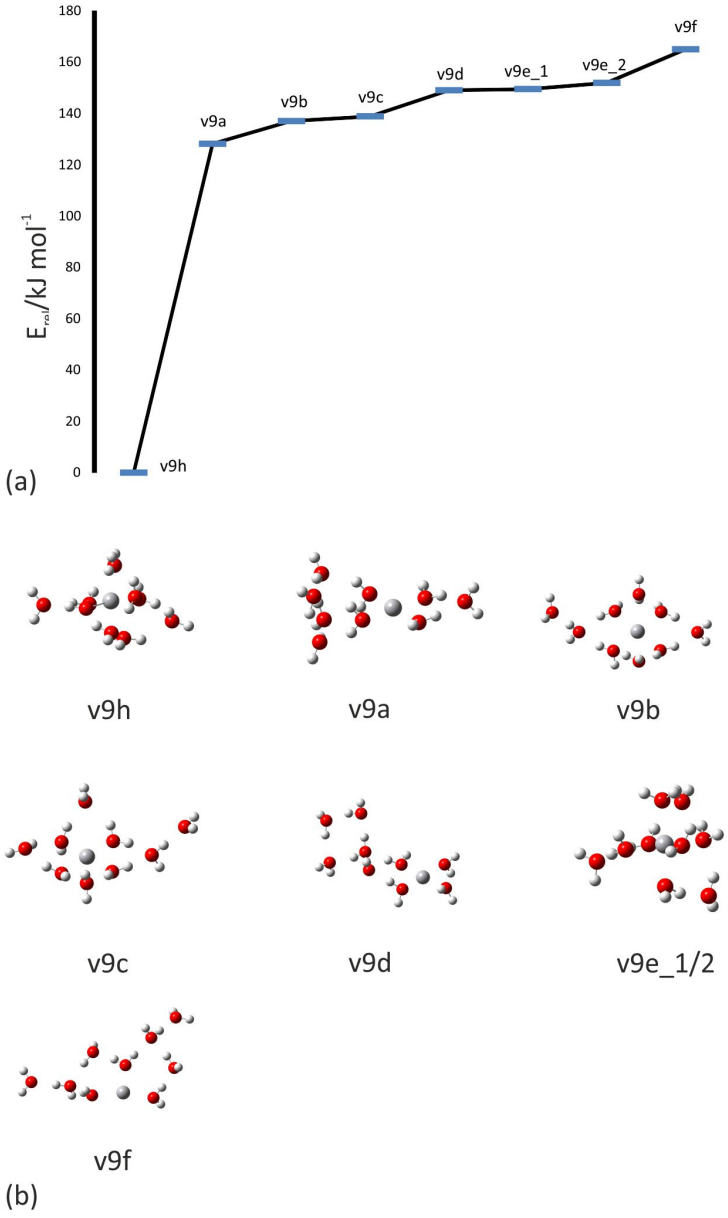

Figure 6.7.: Optimized geometries (b) of $[V(H_2O)_9]^+$ and the relative energy difference (a) to the most stable geometry with $[HVOH]^+$-core.

The geometries are summarized in figure 6.7. In contrast to the hydroxide geometry of $[V(H_2O)_8]^+$, the structure of the first solvation shell is more planar. By the three-dimensional arrangement of the water molecules in the second solvation shell the structure of the first solvation shell became more stabilized and less tensed. The main structural change induced by the eight water molecule is that interaction between the water molecule and the proton is possible, thus further stabilization is present. Also the angle between the hydroxide and the proton only amounts to 102.5°.

The trend of the relative energy and geometries is not changing for the geometry without hydroxide, because the additional water molecule is arranged to the original geometry for $V(H_2O)_8^+$ and the energy ratio remains constant. However, the energy difference between the hydroxide geometry and **v8a** increases to 128 kJ/mol.

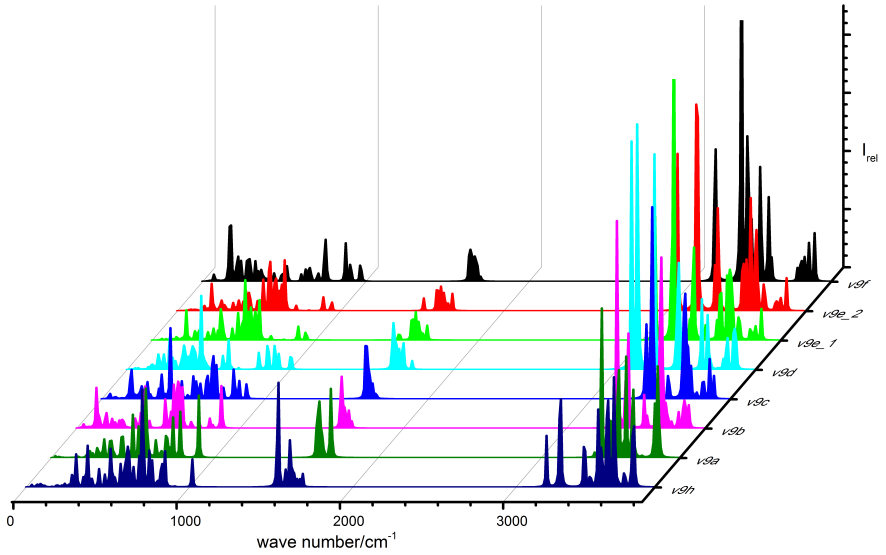

Figure 6.8.: Calculated infrared spectra of $[V(H_2O)_9]^+$. The spectra are ordered according to the relative energy; in the front the most stable one.

The calculated infrared absorption spectra for $[V(H_2O)_9]^+$ are summarized in figure 6.8. In contrast to $[HVOH](H_2O)_7^+$ the two bands at 2935 cm^{-1} and 3352 cm^{-1}, which we assume belong to a partially labile proton, lose intensity. These bands are caused by the same water molecules as described before (fig. 6.3). The loss of intensity can be

explained by the change of the geometry of the square in the first solvation shell. For $[HVOH](H_2O)_7^+$ the square is not planar and it is more like a T-shaped geometry with an additional water molecule which is below this plane. Hence the $d_{x^2-y^2}$ orbital is empty, four coordinated structure with a square planar geometry and for V(III) a octahedral structure is preferred.

However, this is hindered by the binding of the metal ion to the proton and by the absence of further water molecules, which would stabilize the square structure. Thus we assume that the labile mobile proton is stabilizing the T-shaped geometry by mesomerism. By the change of the geometry, the cluster is more stabilized and the proton is no longer so labile. Furthermore the intensity of the band at 1600 cm^{-1} is increasing due to the interaction of the proton between the additional hydrogen bond and the metal ion.

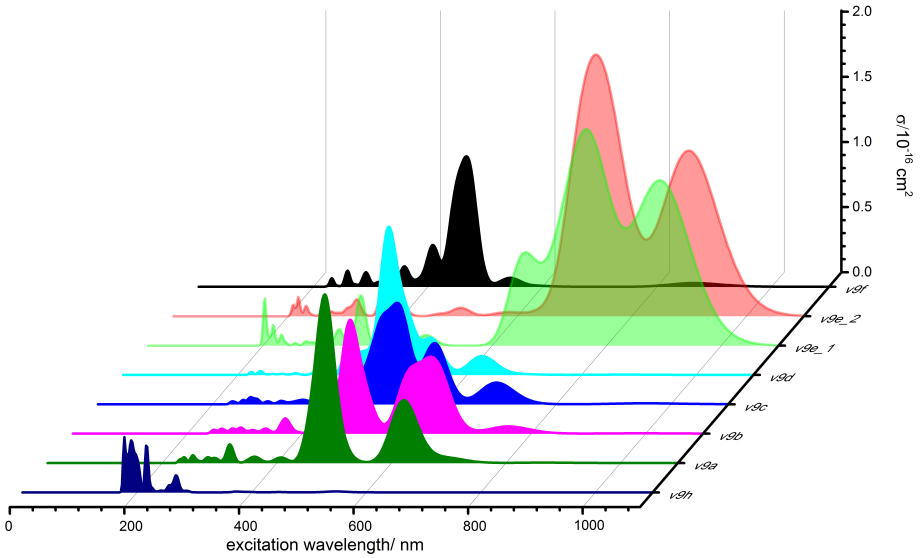

Figure 6.9.: Calculated UV/VIS of $[V(H_2O)_9]^+$. The spectra are ordered according to the relative energy; in the front the most stable one.

The calculated UV/VIS spectra (figure 6.9) show how the absorption spectra are dependent on the geometry and not only on the oxidation state of the metal ion. The absorption spectra are looking different due to the additional water molecule. Furthermore the transition with the calculated strongest oscillator strength is shifting to the

red, namely for the **v9h** from 206.34 nm to 216.82 nm and for **v9a** from 480.41 nm to 486.73 nm.

The geometry **[HVOH](H$_2$O)$_9^+$** is the most stable one of the calculated geometries (figure 6.10).

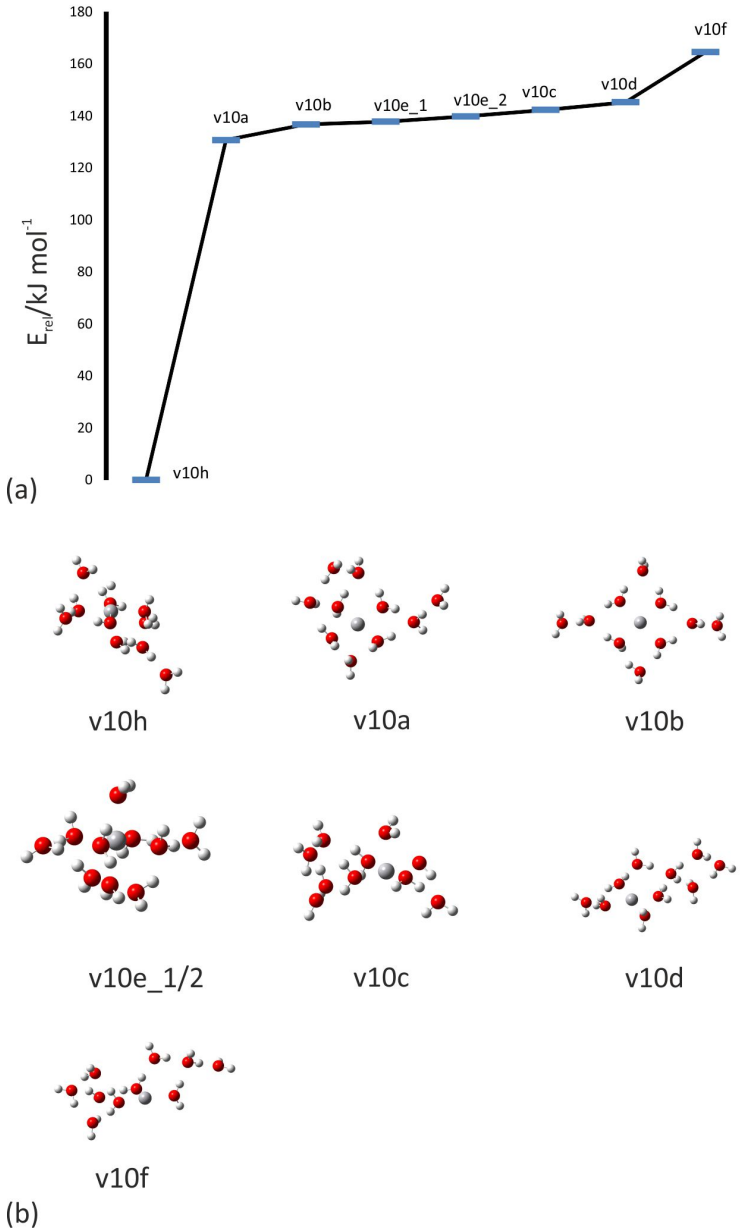

Figure 6.10.: Nine optimized geometries (b) of $[V(H_2O)_{10}]^+$ and their relative energy difference (a) to the most stable geometry with $[HVOH]^+$-core.

In the third solvation shell the additional water molecule is attached. It is interacting with the water molecule, which forms a hydrogen bond with the hydroxide. Otherwise there are no changes in the first and second solvation shell compared to $[HVOH](H_2O)_8^+$. However, the addition of the tenth water molecule to the geometries **v9a-f** changes the stability of the cluster.

The next stable geometry, **v10a** (+131 kJ/mol), is for this cluster size a square planar geometry in the first solvation shell with three water molecules coordinated by one edge water molecule in the second solvation shell. Moreover the remaining water molecules are arranged on the opposite site. All water molecules of the second shell are above or below the square plane. Surprisingly the octahedron geometry is more favored, although the planar square is preferred for V(I).

Maybe the first solvation shell is more stabilized through the additional four water molecules in the second solvation shell. Furthermore the geometry **v10c**, following from **v9a**, lost stability due to the pyramidal quadratic geometry. This seems to be less favored than the octahedron geometry.

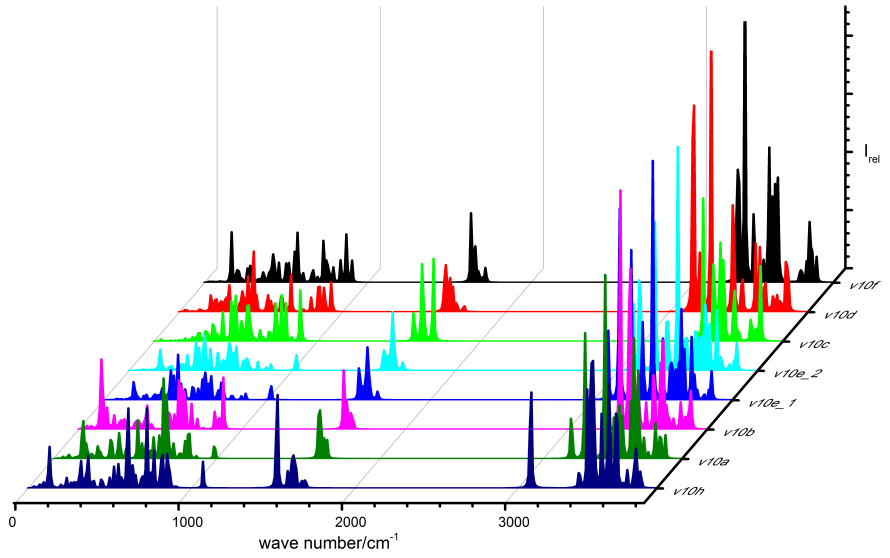

Figure 6.11.: Calculated infrared spectra of $[V(H_2O)_{10}]^+$. The spectra are ordered according to the relative energy; in the front the most stable one.

Due to the hydrogen bond between the additional water molecule and the water molecule next to the hydroxide, the mobility of the labile proton is limited. This is evidenced by the loss of the band at 3350 cm^{-1} (figure 6.11). The band at 3155 cm^{-1} is caused by both stretching vibrations, which were described before in detail, except that one vibration is prevented by the hydrogen bond to the additional water molecule. An increase of the intensity of the band at 1580 cm^{-1} is observed, hence more water molecules are involved to the vibration between proton and metal ion.

The UV/VIS spectra have partially changed by the addition of the tenth water molecule, shown in figure 6.12.

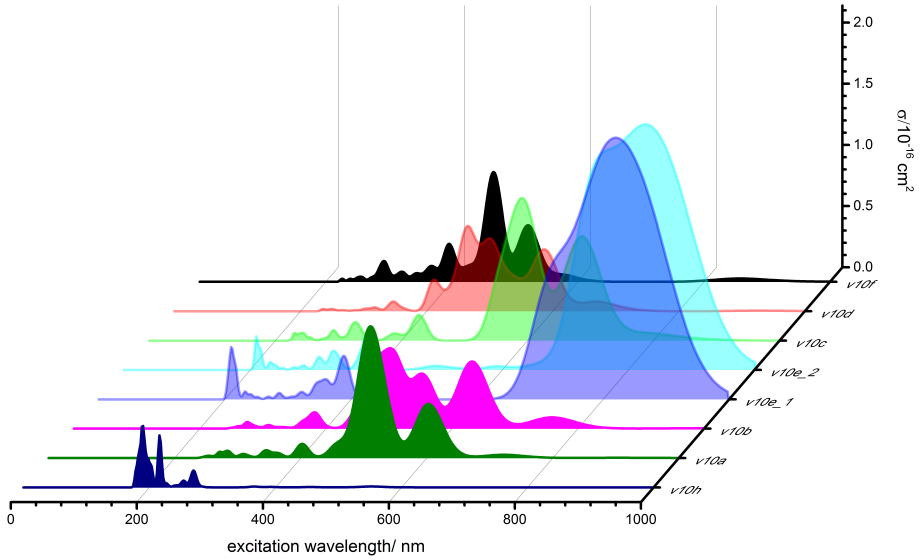

Figure 6.12.: Calculated UV/VIS of $[V(H_2O)_{10}]^+$. The spectra are ordered according to the relative energy; in the front the most stable one.

Due to the change of the square planar to the pyramidal quadratic geometry (**v9a** →**v10c**) the maximum of the absorption at 520 nm disappear. Instead the maximum is now at 600 nm, because the rather weak transitions are preferred. Also the decrease of the intensity for the $3d^3(^3F)4p \leftarrow 3d^4$ transition for **v10a** is observed, since the number of the water molecules is increasing. Presumably new linear combinations of the molecular orbitals make the different transitions possible.

For $[V(H_2O)_{11}]^+$ the distorted planar geometry (figure 6.13) for the first solvation shell at the hydroxide geometry is observed but the distance between the oxygen atoms is not equal, so a square is not present.

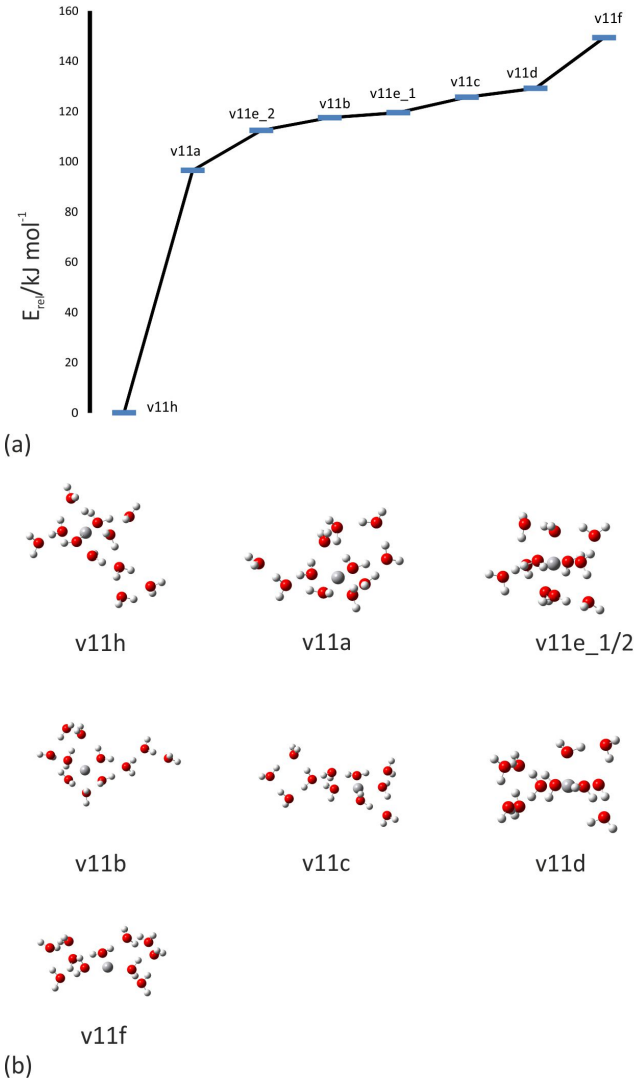

Figure 6.13.: Nine optimized geometries (b) of $[V(H_2O)_{11}]^+$ and their relative energy difference (a) to the most stable geometry with $[HVOH]^+$-core. The octahedral geometry as a low spin complex is more stable than the high spin complex.

Additionally a second water molecule is interacting with the water molecule, which has a hydrogen bond to the hydroxide. Furthermore the hydroxide geometry is less

energetically stable for **v11a** as for $[HVOH](H_2O)_9^+$, namely 34 kJ/mol. The geometry **v11a** with a planar square coordination in the first solvation shell, surrounded only on one plain by the remaining water molecules in the second solvation shell, is 97 kJ/mol unstable.

Surprisingly the distorted octahedral environment around the vanadium(I) ion is the next stable geometry. Uncommonly it is the geometry with a triplet spin state. By running several calculations we could demonstrate that this is not a unique result.

Since the occupation of orbitals with two electrons requires more energy, ^5D is the preferred ground state for the monovalent vanadium ion. Therefore the higher stability of the ^3F ground state is an exception and is only determined for $[V(H_2O)_{11}]^+$. Maybe the octahedral distortion causes that the energy difference between the e_g and t_{2g} orbitals is higher and therefore the occupation of the d_{z^2} orbital is energetically unfavorable for this cluster size.

Irigoras et al. [141] observed the reaction of V^+ with water and they investigated the cross of the low- and high-spin potential surfaces between an intermediate and the $M(OH_2)^+$ ion-molecule complex. Accordingly the exothermic product VO^+ is in the low spin configuration. Such a crossing is possible from the ^5F excited state, which lies 0.557 eV above the ^5D state. [141] Thus, this state is not completely unlikely for vanadium(I). The quintet octahedral geometry lies 7.1 kJ/mol about the triplet spin state.

For the hydroxide geometry the loss of the assumed mobile proton bands is observed, shown in figure 6.14. As mentioned before the change of the geometry in the first solvation shell to planar distorted square causes the increase of the distance between the hydrogen bonds shown in figure 6.3. Furthermore the interaction with the additional water molecules prevents the interaction with the hydroxide.

An unexpected band, shown in figure 6.14, at 3021 cm^{-1} for **v11a** is observed, which is caused by the asymmetrical stretching vibration between the metal ion and the water molecule above (figure 6.15). The vibration is strongly one-sided, whereas the impression follows that there is a labile proton.

Due to the electrostatic polarization of the metal ion, a mechanism is possible where V(I) is oxidized by reacting with the loss of the proton. Furthermore the geometry is predestined for the formation of the hydroxide geometry.

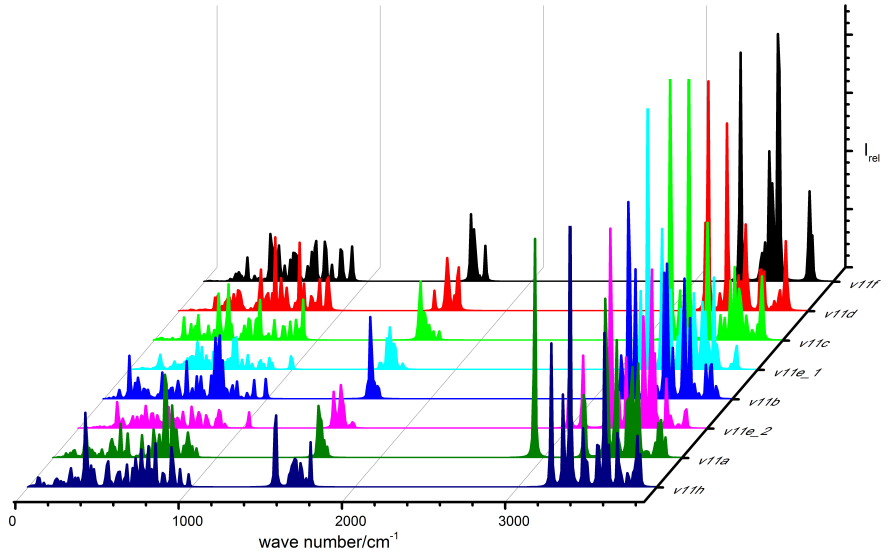

Figure 6.14.: Calculated infrared spectra of $[V(H_2O)_{11}]^+$. The spectra are ordered according to the relative energy; in the front the most stable one.

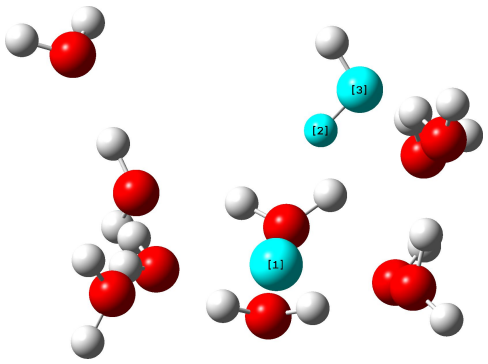

Figure 6.15.: Asymmetrical stretching vibration of the hydrogen atom (2) to the metal ion, which cause the band at 3021 cm^{-1}.

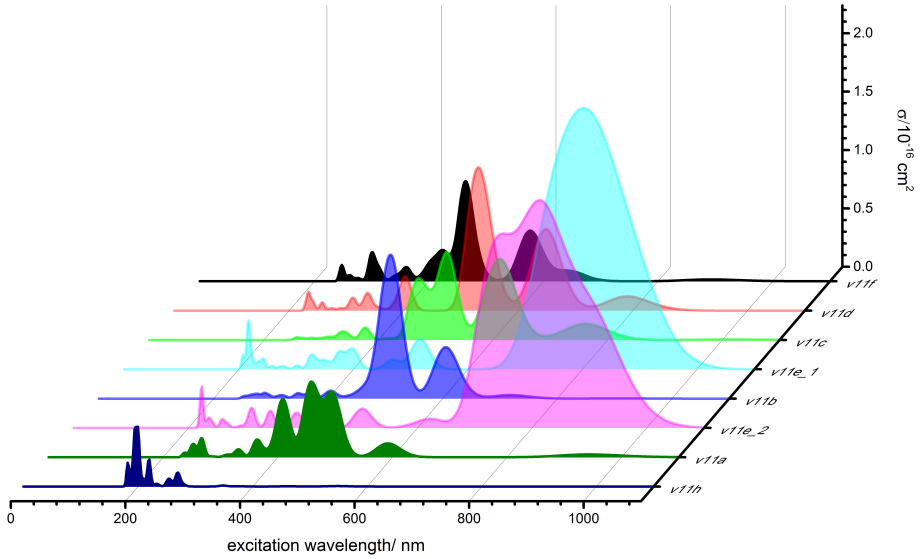

Figure 6.16.: Calculated UV/VIS of $[V(H_2O)_{11}]^+$. The spectra are ordered according to the relative energy; in the front the most stable one.

Due to the additional water molecule the UV/VIS spectra of **v11a** is changing (figure 6.16). There is a loss of intensity observed, which is caused by the increase in the number of absorption bands. Thus new linear combinations are possible with the additional water molecule, whereby the absorption spectrum is changing. Also the absorption spectrum of **v11b** is different to **v10b**, since the geometry is changed in the second solvation shell by interacting with the additional molecule. But only **v11b** next to **v11d/f** show the unique strongest absorption for the $3d^3(^3F)4p \leftarrow 3d^4$ transition.

For the hydroxide geometry of $\mathbf{[V(H_2O)_{12}]^+}$ the additional water molecule is coordinated in the third solvation shell. Furthermore the distance between the water molecule and the proton next to is decreasing from 1.78 to 1.72 Å. The geometry of the first solvation shell, namely the planar distorted pyramidal square, remains the same (figure 6.17). The energy difference between **v12h** and **v12a** is 110 kJ/mol.

While for **v11a** the geometry of the first solvation shell remains a planar square, changes are observed for **v12a**, since distances between the water molecules of the square are not the same and it is no longer planar. The remaining water molecules are arranged

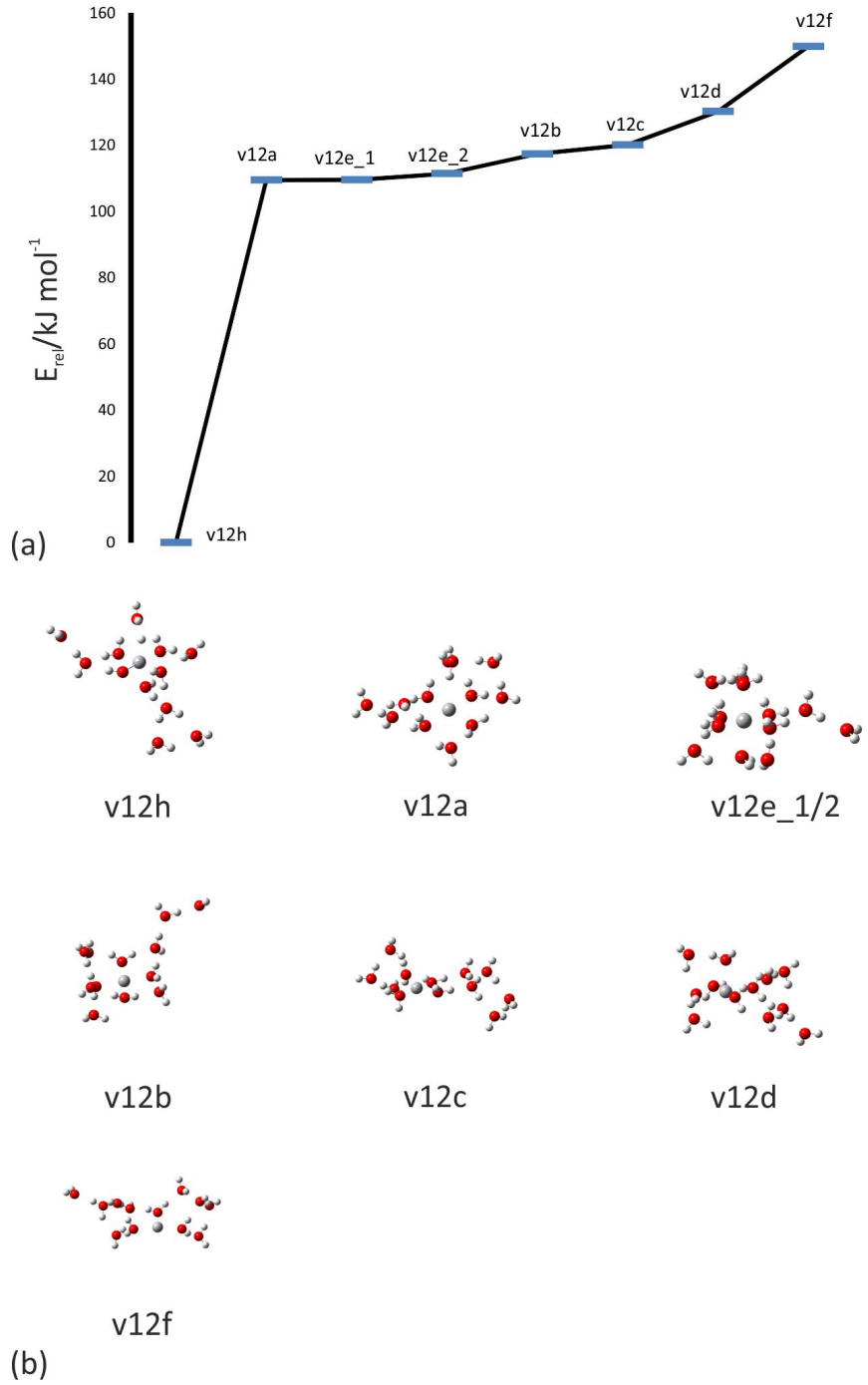

Figure 6.17.: Nine optimized geometries (b) of $[V(H_2O)_{12}]^+$ and their relative energy difference (a) to the most stable geometry with $[HVOH]^+$-core.

on one plane of the square. Due to the changes of the first solvation shell the distance between the metal ion and the hydrogen atom above is decreasing from 2.61 (**v11a**) to 2.57 Å (**v12a**), therefore the interaction between both is facilitated.

The energy difference between **v12a** and the distorted octahedral geometry with quintet spin state amounts only 0.1 kJ/mol, thus both geometries are equally stable. The arrangement of the water molecules in the second solvation shell of the octahedral geometry is changing due to one molecule beeing further away from the others and interacting with the additional water molecule. Furthermore the energy difference between the different spin state geometries is only 2 kJ/mol. Thereby the first three geometries with a water molecules core do not barely differ in their stability. The further order of the geometries remains the same as for $[V(H_2O)_{11}]^+$.

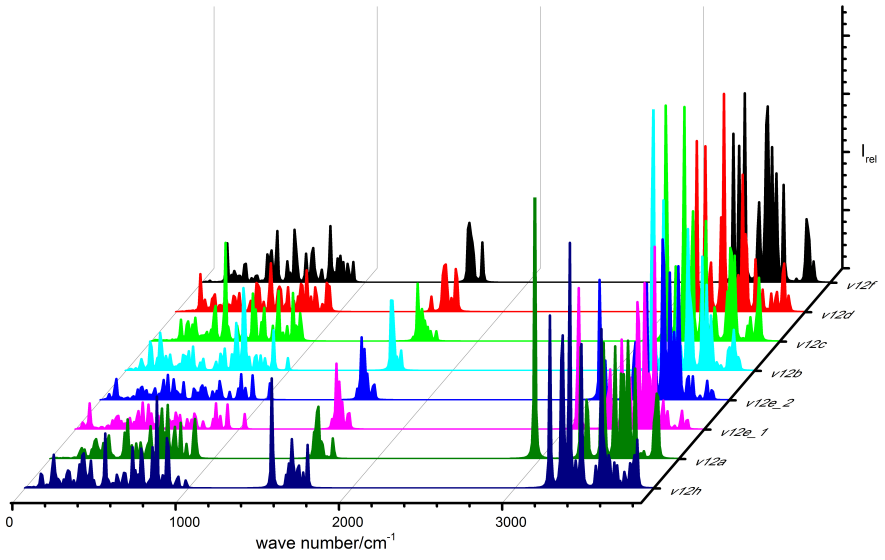

Figure 6.18.: Calculated infrared spectra of $[V(H_2O)_{12}]^+$. The spectra are ordered according to the relative energy; in the front the most stable one.

The infrared spectra for the optimized geometries of $[V(H_2O)_{12}]^+$ are summarized in figure 6.18. Two geometries, namely **v12h** and **v12a**, are notable for certain bands. For **v12h** the band at 1550 cm^{-1} is caused by the proton metal core vibration and is particularly for the hydroxide core. Moreover the band at 3040 cm^{-1} for **v12a** is observed.

As described before it is caused by the asymmetrical stretching vibration between the metal ion and the water molecule above (figure 6.15). This vibration is not influenced by the additional water molecule.

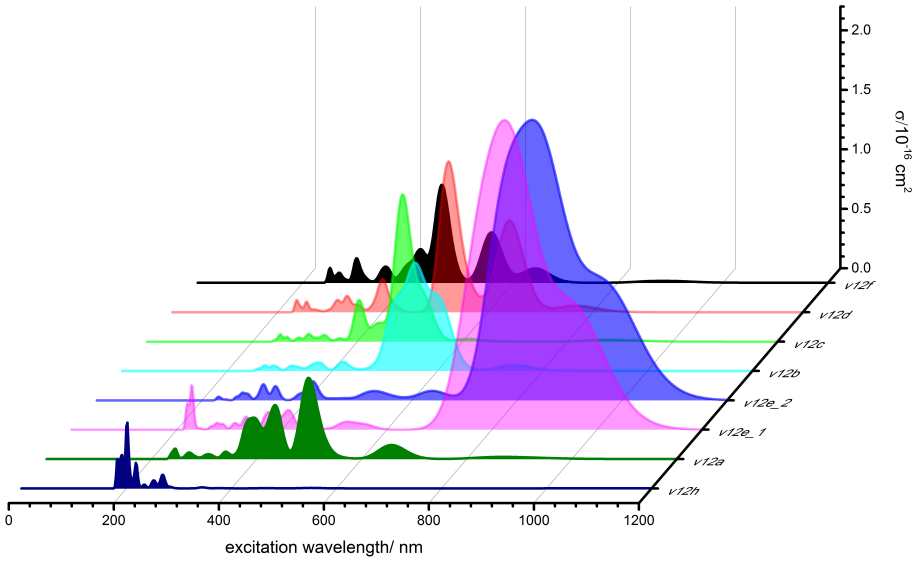

Figure 6.19.: Calculated UV/VIS of $[V(H_2O)_{12}]^+$. The spectra are ordered according to the relative energy; in the front the most stable one.

As for the other hydroxide geometries the absorption maximum lies for $[V(H_2O)_{12}]^+$ at around 220 nm, shown in figure 6.19. The main differences in the spectra are observed for **v12b** and **v12c**. For **v12b** a broader and non unique maximum is determined. While for **v12c** less absorption bands as for **v11c** are calculated. The spectra of the octahedral geometries differ mainly by the weak absorptions, while the strongest absorptions are equal.

6.4. Comparison between B3LYP and CAM-B3LYP

With increasing cluster size the question is raised as to if the B3LYP functional is suitable for the clusters with a full second solvation shell, since the exchange potential of B3LYP has no dependence on the range (r-1). Therefore the UV/VIS spectra for $[V(H_2O)_n]^+$,

n = 8-12, were additionally calculated with the Coulomb-attenuating method (CAM-B3LYP).

CAM-B3LYP is a hybrid functional with improved long-range properties. [150] Marsh et al. [151] calculated with this method the vibrational spectra and optimized the geometry of D_2 tagged $CuOH^+(H_2O)_n$. They observed differences between the various calculation methods, caused by the different treatment of interactions between Cu(II) and the hydroxide ligand. Differences for the calculated UV/VIS spectra were also observed in this study.

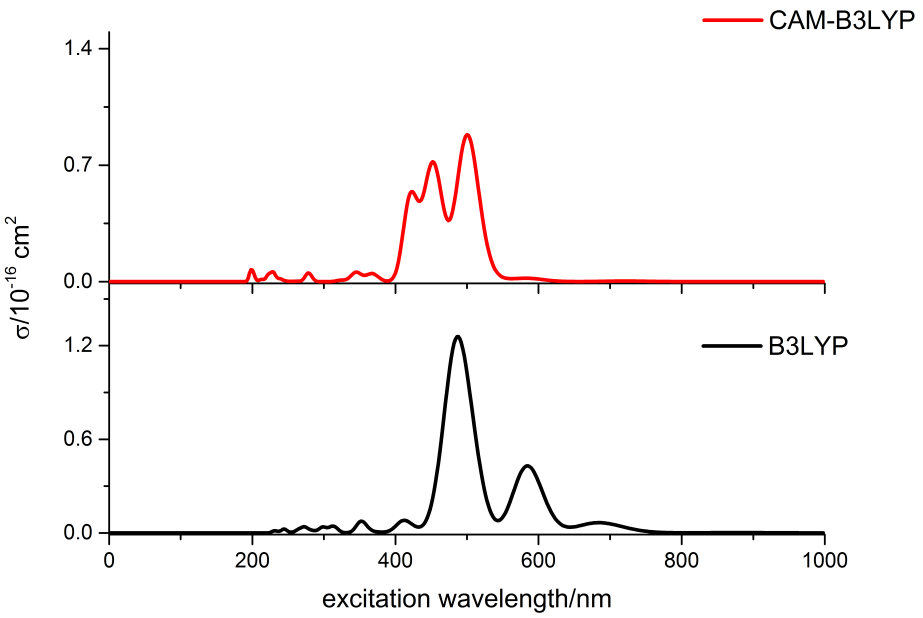

Figure 6.20.: Calculated UV/VIS spectra of $[V(H_2O)_8]^+$ (**v8a** geometry) with CAM-B3LYP (red) and B3LYP (black).

The calculated absorption spectra for $[V(H_2O)_8]^+$ with CAM-B3LYP and B3LYP are shown in figure 6.20.

The strongest calculated oscillator strength for CAM-B3LYP shifts by 19 nm to 499 nm. However, the molecular orbitals for the transition with calculated strongest oscillator strength are the same for both methods, while the intensity is different. Furthermore the weaker absorptions are with B3LYP at higher wavelengths and with CAM at shorter wavelengths as well as the main absorption. The weak absorption $3d^34s \leftarrow 3d^4$ with

B3LYP are not taken into account as with CAM. Instead the transitions between the electrons in the other d-orbitals and the 4p orbitals are more relevant with the CAM calculations.

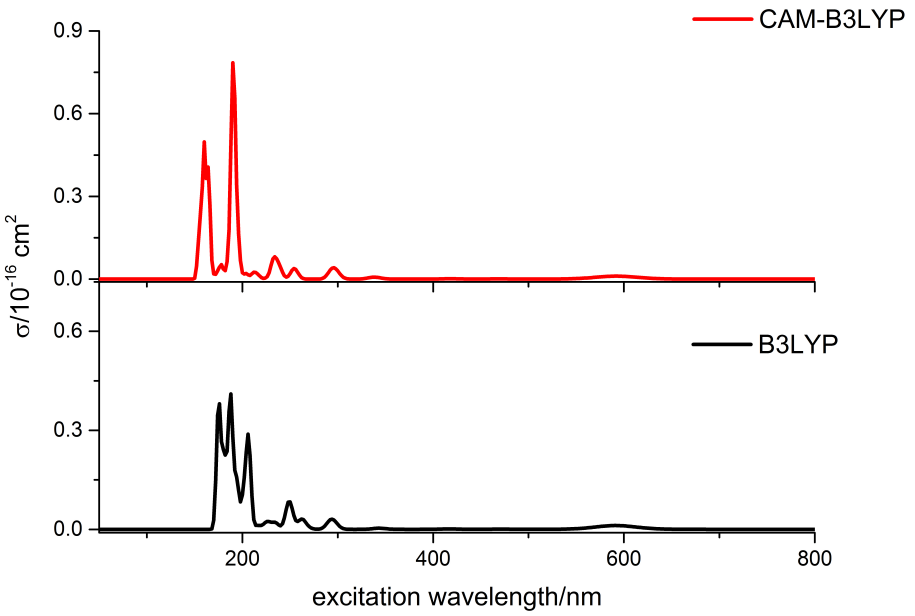

Figure 6.21.: Calculated UV/VIS spectra of $HVOH(H_2O)_7^+$ with CAM-B3LYP (red) and B3LYP (black).

For the calculated UV/VIS spectra of $HVOH(H_2O)_7^+$, shown in figure 6.21, more similarities are observed. The strongest calculated oscillator strength for CAM-B3LYP shifts by 16 nm to 175 nm, but it belongs to a transition between the d-orbitals like the calculated results with B3LYP. Weaker absorptions are also determined at higher wavelengths for both methods. The main differences are in case of the strong absorptions, which have different intensities and appear at different wavelength.

Comparing between the geometries the two methods are more consistent for the hydroxide geometry. While for **v8a** the weak absorptions $3d^3 4s \leftarrow 3d^4$ are not strongly present with the CAM-B3LYP method, a strong absorption at 580 nm is observed with the B3LYP calculation. The interaction between the d_{xy}, d_{xz} and d_{yz} and the 4p orbitals are much stronger with the CAM method, caused by the strong absorption between 400

and 480 nm. This interaction is not so strong for the hydroxide geometry since only two d molecular orbitals are occupied.

Both methods have to be verified experimentally, because no spectra are published so far as we know for this cluster size until now. Scharfschwerdt et al. [147] analyzed the photodissociation of $[V(H_2O)_n]^+$, n = 1-4, in the 360-380 nm region and compared it with B3LYP calculations. Accordingly the calculated maximum is shifting to lower wavelengths (20 nm), which would favor the CAM calculations. But the resolution of the experiment was not enough to resolve the peaks and verify the functional.

6.5. Discussion

The hydroxide geometry is for $V(H_2O)^+$ and $V(H_2O)_2{}^+$ (figure 6.22, orange) not the most stable geometry. Only by the addition of the third water molecule does the hydroxide geometry became the most stable one. A distorted T-shaped structure of the core is formed, which do not change till the $HVOH(H_2O)_7{}^+$ cluster.

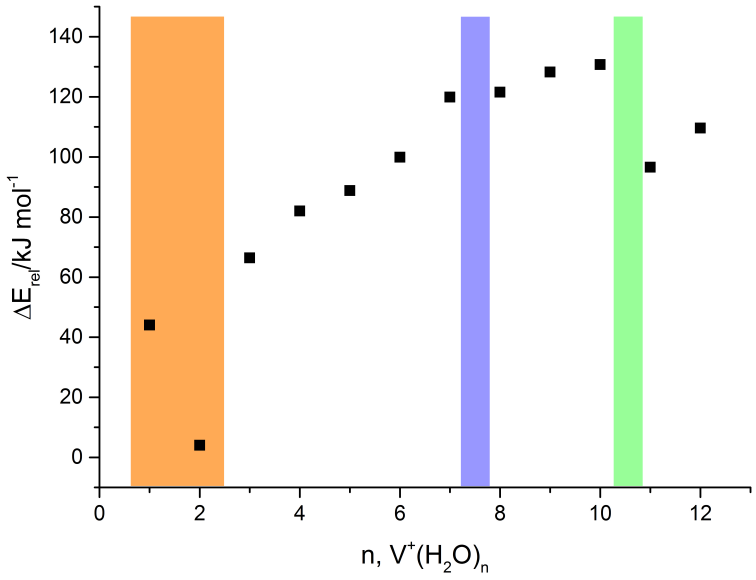

Figure 6.22.: Summary of the relative energy difference between the hydroxide and water molecule geometry for the twelve clusters $[V(H_2O)_n]^+$, n = 1-12.

With increasing number of water molecules the relative energy is increasing linearly until $[V(H_2O)_8]^+$, since the geometry of the first solvation shell is not changing and the additional water molecules are arranging in the second solvation shell by interacting with the hydroxide and the water molecules of the first solvation shell.

At the transition from seven to eight water molecules the relative energy difference is not increasing like before, shown by the purple interruption in figure 6.22. This is caused by the change of the first solvation shell to a less tensed geometry, whereby the stability is decreasing slightly.

For the next three clusters the relative energy is increasing linearly but less strongly as before, due to the changes of the first solvation shell. Furthermore a skip in the relative energy is observed between $HVOH(H_2O)_9^+$ and $HVOH(H_2O)_{10}^+$ caused by the reached distorted planar square geometry of the first solvation shell.

Moreover the geometry with a water molecules $[V(H_2O)_4]^+$ core changes to a three dimension geometry, which is more stable. Overall a formation of a three dimensional geometry is observed with increasing number of water molecules, caused by the polarization of the metal core and loss of stability by water molecules in the third solvation shell interacting only with water molecules.

The influence of the changes in the first solvation shell of the hydroxide geometry is also observed in the IR spectra, shown in figure 6.23. With increasing number of water molecules the number of vibrations caused by the water molecules and the interaction of the cluster is increasing, thus the number of the bands is increasing with the cluster size. For $HVOH(H_2O)_4^+$ a band at 3362.5 cm^{-1} is observed, which is red shifting until $HVOH(H_2O)_7^+$. As described before we assume a stabilization of the T-shaped geometry by a mobile proton. The presence of a mobile proton is also confirmed by the red shift of the frequency through the additional water molecules.

Johnson et al. [149] observed the red shift and explained it by formation of hydrogen bond to neighboring water molecules. Additional water molecules cause the loss of intensity of these bands until they disappear at $HVOH(H_2O)_n^+$, n = 10 – 11. This is reached by the interaction between the water molecule next to the hydroxide and the additional neighboring water molecules. The mobile proton favors the atomic hydrogen abstraction for the reaction with infrared photons. We observed the H abstraction for $[V(H_2O)_n]^+$, n

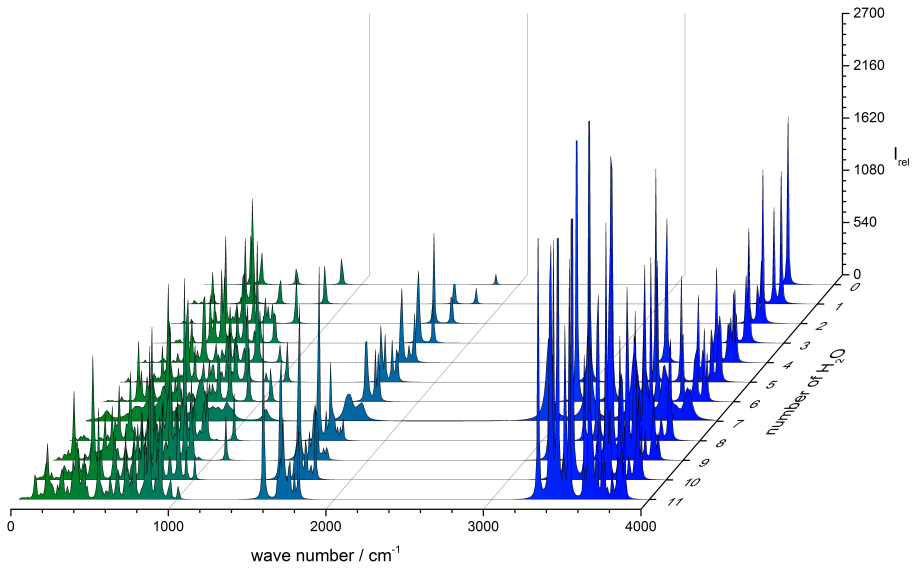

Figure 6.23.: Summary of the IR-Spectra for the hydroxide geometry of $HVOH(H_2O)_n^+$, n = 0-11.

= 8 – 11, and not for $[V(H_2O)_{12}]^+$. The loss of the atomic hydrogen may be stabilized by the mobile proton and additionally the relaxation of the geometry to a distorted square planar geometry is preferred.

For $[V(H_2O)_{11}]^+$ and $[V(H_2O)_{12}]^+$ a big change in the geometry and IR spectra is observed. This agrees well with the experimental results, since for $[V(H_2O)_{12}]^+$ fragmentation and atomic hydrogen loss only occur at room temperature with very low reactivity, while the molecular hydrogen abstraction is the main reaction. [146] Furthermore for $[V(H_2O)_{11}]^+$ the simultaneous loss of three water molecules is determined. [146] For both clusters no bands caused by the mobile proton for the hydroxide geometry are observed.

However, they are present for the water core geometry, shown in figure 6.24. They are caused by the vibration of the hydrogen atom to the metal core. This potential mobile proton, and the fact of the very small energy difference between the triplet and quintet spin state, could cause the different reaction pathways as for $[V(H_2O)_n]^+$,n = 8 – 10. Irigoras et al. [141] studied the reaction of water with V^+. They showed that the H_2

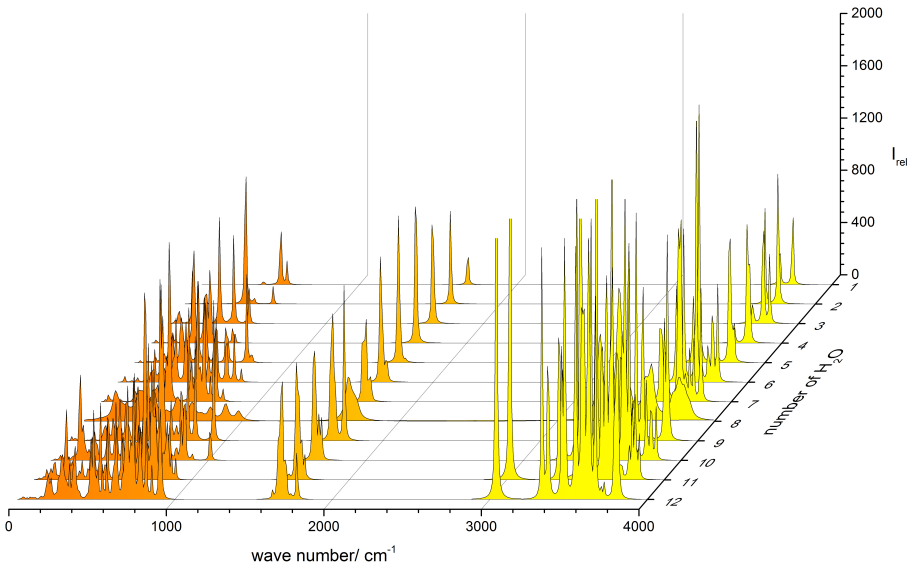

Figure 6.24.: Summary of the IR-spectra for the most stable distorted square planar geometry of $[V(H_2O)_n]^+$, n = 1-12.

elimination process passes from HV^+OH intermediate by crossing between the low and high spin potential energy surfaces.

Our calculations show the high stability of the hydroxide geometry with a triplet spin state, which favor the H_2 abstraction. Additionally the high stability of the octahedral geometry with triplet spin state for $[V(H_2O)_n]^+$, n = 11 – 12, favors the possibility of the molecular hydrogen abstraction. Sasaki et al. [144] studied $[V(H_2O)_n]^+$, n = 2 – 7, by infrared photodissociation spectroscopy in the range of 3000 – 4000 cm^{-1}. A comparison is difficult because of the low resolution of the spectra, but there is a band at 3200 – 3400 cm^{-1} for $[V(H_2O)_n]^+$, n = 5 – 8, so the hydroxide geometry is possible.

With UV/VIS spectroscopy unique evidence is possible to differentiate between the geometries due to the different electronic states of the metal ion. The difference between the absorption maxima of the hydroxide core and square planar geometry, shown in figure 6.25-6.28, allows spectroscopic investigation between them.

The absorption maximum for $[HVOH]^+$ lies around 160 nm and undergoes a red shift by the solvation with water molecules till $HVOH(H_2O)_{11}{}^+$ to 210 nm, shown in figure

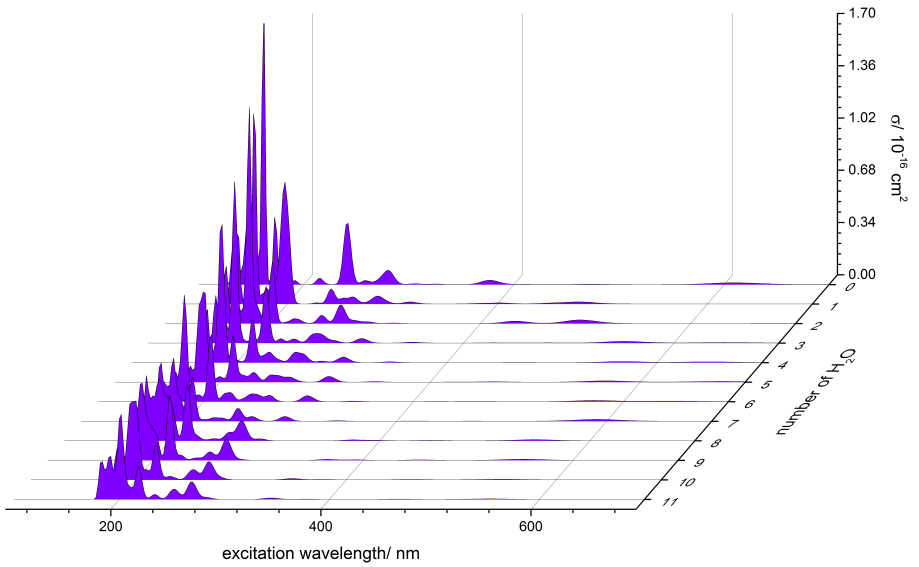

Figure 6.25.: UV/VIS spectra for the $HVOH(H_2O)_n^+$ geometry with n = 0-11 water molecules calculated with B3LYP.

6.25. The red shift is for the first four water molecules significantly pronounced since the first solvation shell is filled completely. Altogether a loss of intensity for the main absorption is observed with increasing number of water molecules. In comparison the intensity of the weak absorptions is increasing. Linear combinations with the water molecules favor the parity forbidden one. For $HVOH(H_2O)_n^+$, n= 7 – 11, small changes for the absorptions are observed for both methods, for CAM shown in figure 6.26, but the intensity remains constant. This is due to the open geometry, since only the first solvation shell is completely filled and the further water molecules do not complete the second solvation shell.

The absorption maximum for $V(H_2O)^+$ lies around 230 nm [147] and is shifting via 440 nm for $[V(H_2O)_5]^+$ to 500 nm until $[V(H_2O)_{12}]^+$, shown in figure 6.27.

Like for the hydroxide geometry, the largest red shift is caused by completing the first solvation shell. The red shift for the square planar geometry is higher than for the hydroxide geometry due to the stronger interactions between the exited state of the

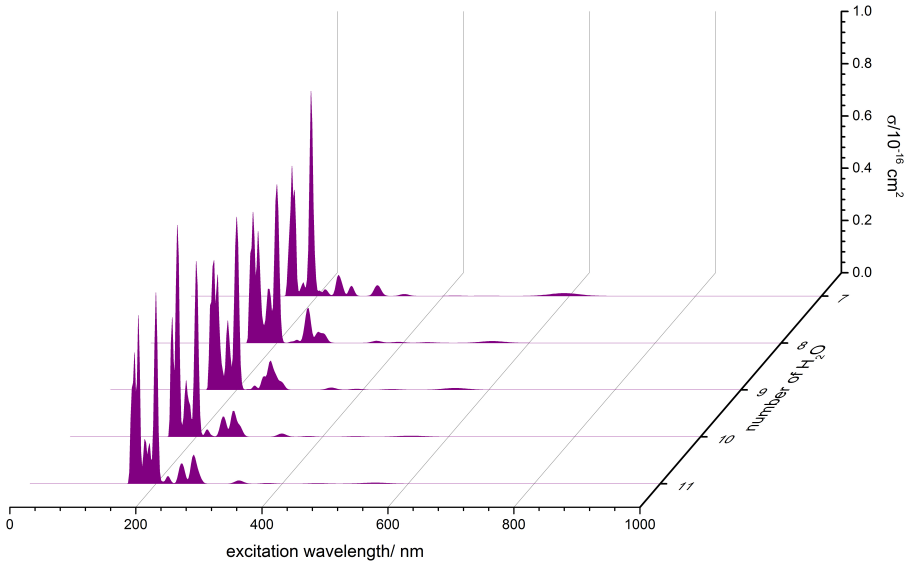

Figure 6.26.: UV/VIS spectra for the $HVOH(H_2O)_n^+$ geometry with n = 7-11 water molecules calculated with CAM-B3LYP.

vanadium ion with the water molecules. Therefore the binding energy of the water molecules is increasing and a stronger red shift is observed.

Whereas, the interaction to the V(III) ion is lower since it is bound to the hydroxide and the proton. The intensity decreases in contrast to the hydroxide geometry not continuously. An abrupt decrease of the intensity is observed between $[V(H_2O)_{10}]^+$ and $[V(H_2O)_{11}]^+$, because the transition with the strongest calculated oscillator strength is changing. While for $[V(H_2O)_n]^+$, n = 1 – 10, the strong absorption is caused by the allowed $3d^3(^3F)4p \leftarrow 3d^4$ transition with the before mentioned molecular orbitals, the strong absorption for $[V(H_2O)_n]^+$, n = 11-12, is induced by the transition with the strongest calculated oscillator strength between the d^4 molecular orbitals.

This observation is consistent with the calculation with the CAM-B3LYP functional, shown in figure 6.28. Both methods show the change of the transition for $[V(H_2O)_n]^+$, n = 11 – 12.

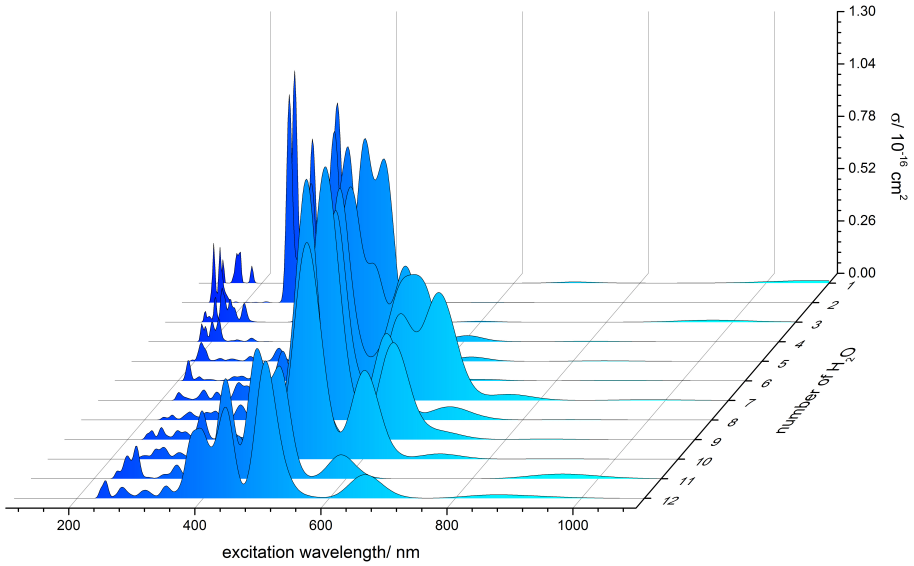

Figure 6.27.: UV/VIS spectra for the $[V(H_2O)_n]^+$ geometry with n = 1-12 water molecules calculated with B3LYP.

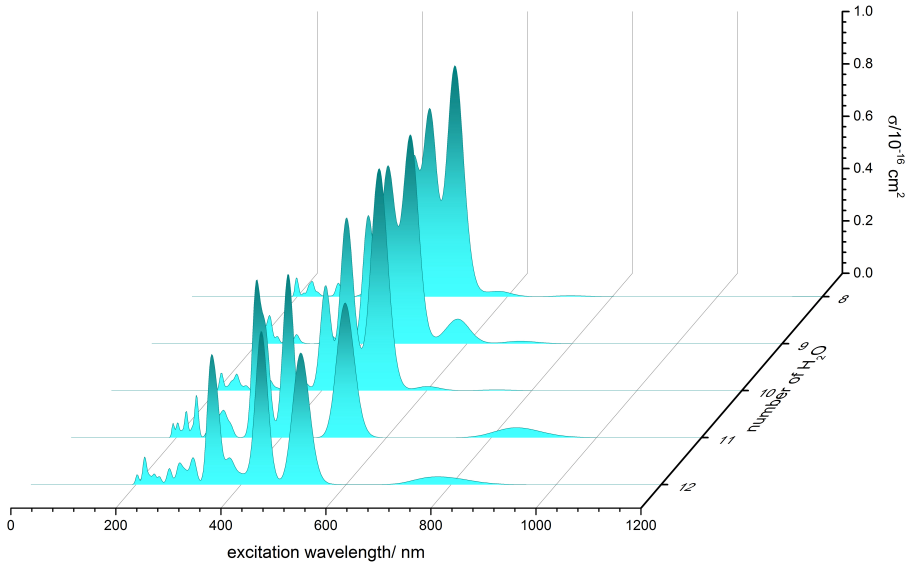

Figure 6.28.: UV/VIS spectra for the $[V(H_2O)_n]^+$ geometry with n = 8-12 water molecules calculated with CAM-B3LYP.

The loss of intensity implies weaker interactions between the exited state of the metal ion and the water molecules. This could be achieved by reduction of the electron density of the metal ion by the interaction with the mobile proton. The reduction of the electron density is observed for the hydroxide geometry, hence the intensity of the absorptions are lower. Perhaps the geometry has a hydroxide character, which would explain the different reaction pathways for both clusters.

7. Summary and Outlook

7.1. Summary

In the present PhD thesis reactions of the hydrated first–row transition monovalent metal ions $[M(H_2O)_n]^+$ with different organic reactants were studied. Information regarding reaction rates and reactivity were obtained by kinetic and nanocalorimetric analysis. Altogether four different reaction types were observed, which depend on the reactant and on the metal ion. Moreover, the dependence of the reactivity on the cluster size were examined.

The first and most frequently observed type of reaction is ligand exchange:

$$[M(H_2O)_n]^+ + RX \rightarrow [MRX(H_2O)_m]^+ + (n-m)\ H_2O \tag{7.1}$$

Furthermore evidence for charge transfer was found:

$$[M(H_2O)_n]^+ + RX \rightarrow [M^{2+}RX^-(H_2O)_m]^+ + (n-m)\ H_2O \tag{7.2}$$

Also evidence for the insertion of the metal ion into the R–X bond was observed:

$$[M(H_2O)_n]^+ + RX \rightarrow [X - M - R(H_2O)_m]^+ + (n-m)\ H_2O \tag{7.3}$$

Although the product mass alone does not allow to distinguish the reaction (7.2) and (7.3). Besides the formation of metal-organic or salt-like compounds were investigated:

$$[M(H_2O)_n]^+ + RX \rightarrow [MX(H_2O)_m]^+ + (n-m)\ H_2O + R^\bullet \tag{7.4}$$

Note that for reaction (7.2) – (7.4) the oxidation state of the metal changes from M(I) in the educt clusters to M(II) (equation (7.2)/(7.4)) and M(III) (equation (7.3)) in the product clusters. Therefore three different types of oxidation reactions were observed. In table 7.1 all reactions are summarized.

Table 7.1.: Overview of all observed reactions for $[M(H_2O)_n]^+$, M = Cr, Mn, Fe, Co, Ni, Cu and Zn.

reactant	ligand exchange (7.1)	charge transfer (7.2)	insertion (7.3)	redox reaction (7.4)
CH_3CN	Cr,Mn,Fe,Co,Ni,Cu,Zn	Cr		Zn
C_3H_7I	Cr,Mn,Fe,Co,Ni,Cu		Ni,Co,Cu	Cr,Mn,Fe,Co,Zn
C_6H_5Cl	Cu			Zn
C_6H_5Br	Cu			Zn
C_6H_5I	Cu			Zn

For all metal cations ligand exchange reactions were observed with acetonitrile. Furthermore products are formed with metal ions solvated only by acetonitrile. Especially the ligand exchange with Cr^+ and the first acetonitrile molecule is heavily exothermic (-195 kJ/mol), so a charge transfer to the acetonitrile molecule is assumed like in equation (7.2), since the values for the formation enthalpy for the second and third ligand exchange are consistent with a simple exchange. For hydrated Zn(I) ions formation of $[ZnOH(CH_3CN)_m(H_2O)_n]^+$ is observed via loss of CH_3CNH or CH_3CHN. In this case Zn(I) is oxidized to Zn(II) and a hydroxide OH^- is formed.

The ligand exchange reaction with iodopropane was observed for all metals except zinc and vanadium. This reaction is sensitive to the cluster size and starts in most cases in a narrow cluster size range about n = 20–5. Cr(I), Co(I) and Zn(I) are oxidized by iodopropane to the oxidation state II with formation of the MI^+ ion, equation (7.4). For Mn(I) and Fe(I) the oxidation and formation of the MI^+ ion is sensitive to the cluster size and occurs at long reaction delays. The investigated reaction rates are in the same range; however the formation enthalpy is different. The oxidation of Cr^+ is the most exothermic reaction. For cobalt and nickel the formation of $[MC_3H_6(C_3H_7I)_2]^+$ was noticed, which is caused due to a possible metal insertion mechanism (equation 7.3) followed by loss of HI through the transfer of an H atom to the metal ion. Because of the detected products an olefin formation is assumed. Moreover the high reactivity of the second ligand exchange of Cu^+ and the high stability of $[CuC_3H_7I(H_2O)]^+$ indicates an intra-cluster reaction, where a metal insertion into the C-I bond is possible.

Zn(I) is oxidized to Zn(II) by halogenated aromatic compounds, while hydrated Cu(I) undergoes ligand exchange. The ligand exchange for Cu(I) depends on the solubility of the organic compounds in water. Thus the reaction rates are correlated with the solubility of the aryl halides. Activation of the C-Cl bond is difficult due to the high bond dissociation energy (BDE(C_6H_5-Cl) = 95.5 kcal/mol). [83] Therefore the reaction between $[Zn(H_2O)_n]^+$ and chlorobenzene is observed only at relatively high pressure. The selective formation of the hydrated organometallic $C_6H_5Zn^+$ ion in the reaction with C_6H_5Cl is in contrast to the reactions with C_6H_5Br and C_6H_5I, in which efficient formation of hydrated $ZnBr^+$ and ZnI^+ is observed. DFT calculations for the thermodynamics of the reactions show, that the formation of $C_6H_5Zn^+$ is not preferred, because it is endothermic. Furthermore the formation of $ZnBr^+$ and ZnI^+ is only exothermic in aqueous environment.

Altogether the oxidation of Zn(I) occured with every reactant, since Zn(II) is stable with d^{10} electron configuration. Chromium is showing a higher reactivity than most of the other metal ions, which depends on the reactant. Furthermore cobalt and nickel show interesting chemistry with iodopropane, which depends on the cluster size. In addition iron and manganese exhibit low reactivity and a high cluster size dependence with iodopropane. For iron it is surprising, because a metal insertion like for cobalt and nickel was expected due to results with bare iron cations. [111] Here, the influence of the solvation shell is observable. Copper is mostly reacting by ligand exchange like it was expected. Vanadium is not reacting with iodopropane due to the different oxidation state depending on the reaction with room-temperature blackbody photons. This was investigated with DFT calculations.

Using the DFT method different optimized geometries for $[V(H_2O)_n]^+$, n = 1-12, were investigated, whose local minimum character is verified by frequency calculations. The hydroxide geometry with $[HVOH]^+$ core is the most stable one for $[V(H_2O)_n]^+$, n = 3-12 and undergoes a change of the geometry from a distorted T-shape to a distorted square in the first solvation shell with increasing number of water molecules. Furthermore a mobile proton is observed for the distorted T-shape geometry, which might stabilize the strained geometry due to its mobility within the first solvation shell. During the change of the geometry for $HVOH(H_2O)_n{}^+$, n = 7-9, the frequency caused by the mobile proton is shifting and an intensity loss is observed until it disappears at $HVOH(H_2O)_{10}{}^+$. The other stable geometry for $[V(H_2O)_n]^+$ consists of a distorted square planar first solvation

shell. With increasing number of water molecules the stability of the triplet spin state and the octahedral geometry increase. Furthermore another mobile proton occurs for $[V(H_2O)_n]^+$, n= 11-12, which is an indication of the different reaction pathways with infrared photons.

Using TD-DFT UV/VIS spectra were calculated for all optimized geometries and for the most stable ones additionally with CAM-B3LYP functional. Both main geometries differ due to different absorption spectra and maxima, which are separated by about 200 nm. In addition the octahedral geometry has specific absorption bands, which are equal for the quintet and triplet spin state of the metal ion. For $[V(H_2O)_n]^+$, n = 1-10, with square planar first solvation shell the main absorption is the allowed $3d^3(^3F)4p \leftarrow 3d^4$ transition and for the hydroxide geometry it is a transition within the 3d orbitals. For both a red shift is observed with increasing number of water molecules. However, for $[V(H_2O)_n]^+$, n = 11-12, the strong absorption is unexpectedly changing to a transition between the d orbitals. Comparisons with the CAM calculations confirm that the trends and the strong transitions are the same. Particularly there are differences for the weak absorptions.

7.2. Outlook

Experiments with different alkyl halides and different chain lengths would gather information about the catalytic olefine formation in aqueous environment. Furthermore the formation of cyclic compounds at long chain lengths could be possible. Moreover, further information about the corrosion process of metals, which results in economic damage, can be obtained.

The insertion of the metals into the R-X bond is so far speculative and no information about the time of the insertion can be obtained. Therefore a combination of the ICR mass spectrometer with spectroscopy would be a powerful tool to investigate the oxidation state of the metals, because the absorption maxima depend on the oxidation state of the metal. In addition, the possibility would be given to study the photochemistry of the metals in the gas phase. Thermochemical information can be obtained from measuring the wavelength threshold for different photodissociation channels.

A further advantage of the combination would be the verification of the theoretical calculations of $[V(H_2O)_n]^+$, which provide reasons for the different reactivity of the clusters induced by room temperature blackbody radiation. Furthermore the functional of the TD-DFT calculations and thus the calculated absorption spectra should be tested experimentally. Even choice of the most adequate functional and basis set could be simplified by experiments with clusters in the gas phase. B3LYP and CAM-B3LYP differ in the description of weak interactions, which results in different absorption maxima in the calculated UV-VIS spectra. Experiments will show which functional is more adequate for the description of the interactions in hydrated vanadium ions.

Bibliography

[1] Martin Chaplin, Water structure and science http://www1.lsbu.ac.uk/water/, **30.09.15**.

[2] K. P. C. Vollhardt, N. E. Schore, *Organische Chemie*, 4 . Auflage, Wiley-VCH Verlag, Weinheim, **2005**.

[3] B. S. Fox, O. P. Balaj, I. Balteanu, M. K. Beyer, V. E. Bondybey, *Chem. Eur. J.* **2003**, *34*(9).

[4] B. S. Fox, M. K. Beyer, U. Achatz, S. Joos, G. Niedner-Schatteburg, V. E. Bondybey, *J. Phys. Chem. A* **2000**, *104*(6), 1147.

[5] U. Achatz, S. Joos, C. Berg, T. Schindler, M. Beyer, G. Albert, G. Niedner-Schatteburg, V. E. Bondybey, *J. Am. Chem. Soc.* **1998**, *120*(8), 1876.

[6] B. S. Fox, O. P. Balaj, I. Balteanu, M. K. Beyer, V. E. Bondybey, *J. Am. Chem. Soc.* **2002**, *124*(2), 172.

[7] W. A. Donald, R. D. Leib, J. T. O'Brien, Holm, Anne I S, E. R. Williams, *Proc. Natl. Acad. Sci. USA* **2008**, *105*(47), 18102.

[8] K. Eller, H. Schwarz, *Chem. Rev.* **1991**, *91*(6), 1121.

[9] J. Roithová, D. Schröder, *Chem. Rev.* **2010**, *110*(2), 1170.

[10] D. K. Böhme, H. Schwarz, *Angew. Chem. Int. Ed. Engl.* **2005**, *44*(16), 2336.

[11] L. M. Roth, B. S. Freiser, *Mass Spectrom. Rev.* **1991**, *10*(4), 303.

[12] Giffin D. Jones, Harold E. Doorenbos, Eneynols from acetylenes and propargylic alcohols, us 4620045 a, **1986**.

[13] L. Brandsma, S. F. Vasilevsky, H. D. Verkruijsse, *Application of transition metal catalysts in organic synthesis*, Springer desktop editions in chemistry, Springer, Berlin and New York, **1999**.

[14] M. A. Duncan, *Annu. Rev. Phys. Chem.* **1997**, *48*, 69.

[15] M. A. Duncan, *Int. J. Mass Spectrom.* **2000**, *200*(1-3), 545.

[16] K. Fuke, K. Hashimoto, S. Iwata, in *Adv. Chem. Phys.*, Bd. 110, pp. 431–523.

[17] G. Niedner-Schatteburg, V. E. Bondybey, *Chem. Rev.* **2000**, *100*(11), 4059.

[18] V. E. Bondybey, M. K. Beyer, *Int. Rev. Phys. Chem.* **2002**, *21*(2), 277.

[19] M. K. Beyer, *Mass Spectrom. Rev.* **2007**, *26*(4), 517.

[20] W. A. Donald, R. D. Leib, J. T. O'Brien, M. F. Bush, E. R. Williams, *J. Am. Chem. Soc.* **2008**, *130*(11), 3371.

[21] R. F. Höckendorf, O. P. Balaj, C. van der Linde, M. K. Beyer, *Phys. Chem. Chem. Phys.* **2010**, *12*(15), 3772.

[22] T.-W. Lam, C. van der Linde, A. Akhgarnusch, Q. Hao, M. K. Beyer, C.-K. Siu, *ChemPlusChem* **2013**, *78*(9), 1040.

[23] D. B. Jacobson, B. S. Freiser, *J. Am. Chem. Soc.* **1983**, *105*(16), 5197.

[24] J. Allison, D. P. Ridge, *J. Am. Chem. Soc.* **1979**, *101*(17), 4998.

[25] B. S. Fox-Beyer, Z. Sun, I. Balteanu, O. P. Balaj, M. K. Beyer, *Phys. Chem. Chem. Phys.* **2005**, *7*(5), 981.

[26] B. S. Fox, I. Balteanu, O. P. Balaj, H. Liu, M. K. Beyer, V. E. Bondybey, *Phys. Chem. Chem. Phys.* **2002**, *4*(11), 2224.

[27] C. Garino, L. Salassa, *Philos. Trans. R. Soc. London, Ser. A* **2013**, *371*(1995), 20120134.

[28] E. O. Lawrence, M. S. Livingston, *Phys. Rev.* **1932**, *40*(1), 19.

[29] M. B. Comisarow, A. G. Marshall, *Chem. Phys. Lett.* **1974**, *25*(2), 282.

[30] A. G. Marshall, C. L. Hendrickson, *Int. J. Mass Spectrom.* **2002**, *215*(1-3), 59.

[31] P. Caravatti, M. Allemann, *Org. Mass Spectrom.* **1991**, *26*(5), 514.

[32] I. A. Boldin, E. N. Nikolaev, *Rapid Commun. Mass Spectrom.* **2011**, *25*(1), 122.

[33] C. Berg, T. Schindler, G. Niedner-Schatteburg, V. E. Bondybey, *J. Chem. Phys.* **1995**, *102*(12), 4870.

[34] R. F. Höckendorf, C. van der Linde, O. P. Balaj, I. Herber, M. K. Beyer, *Int. J. Mass Spectrom.* **2011**, *300*(1), 44.

[35] V. E. Bondybey, J. H. English, *J. Chem. Phys.* **1981**, *74*(12), 6978.

[36] T. G. Dietz, M. A. Duncan, D. E. Powers, R. E. Smalley, *J. Chem. Phys.* **1981**, *74*(11), 6511.

[37] S. Maruyama, L. R. Anderson, R. E. Smalley, *Rev. Sci. Instrum.* **1990**, *61*(12), 3686.

[38] O.P.Balaj, *The Chemistry of Solvated Ions studied by FT-ICR Mass spectrometry*, Dissertation, Technische Universität München, Garching, **2005**.

[39] C. van der Linde, S. Hemmann, R. F. Höckendorf, O. P. Balaj, M. K. Beyer, *J. Phys. Chem. A* **2013**, *117*(6), 1011.

[40] C. van der Linde, *Reaktivität und Thermochemie hydratisierter Radikalanionen von atmosphärischer Relevanz*, Dissertation, Christian-Albrechts-Universität zu Kiel, Kiel, **2009**.

[41] B. S. Fox, M. K. Beyer, V. E. Bondybey, *J. Phys. Chem. A* **2001**, *105*(26), 6386.

[42] P. D. Schnier, W. D. Price, R. A. Jockusch, E. R. Williams, *J. Am. Chem. Soc.* **1996**, *118*(30), 7178.

[43] R. C. Dunbar, *Mass Spectrom. Rev.* **2004**, *23*(2), 127.

[44] O. P. Balaj, C. B. Berg, S. J. Reitmeier, V. E. Bondybey, M. K. Beyer, *Int. J. Mass Spectrom.* **2009**, *279*(1), 5.

[45] T. Schindler, C. Berg, G. Niedner-Schatteburg, V. E. Bondybey, *Chem. Phys. Lett.* **1996**, *250*(3-4), 301.

[46] C. Hock, M. Schmidt, R. Kuhnen, C. Bartels, L. Ma, H. Haberland, B. v.Issendorff, *Phys. Rev. Lett.* **2009**, *103*(7).

[47] M. K. Beyer, B. S. Fox, B. M. Reinhard, V. E. Bondybey, *J. Chem. Phys.* **2001**, *115*(20), 9288.

[48] Michael J. Pilling, Paul. W. Seakins, *Reaction Kinetics*, Oxford Science Publikations, Oxford, **2007**.

[49] T. Schindler, Dissertation, Technische Universität München, Garching, **1992**.

[50] J. E. Bartness, R. M. Georgiadis **1983**, (33(3)), 149.

[51] M. K. Beyer, Analyzze, **2004-2012**.

[52] V. Nissen, *Einführung in Evolutionäre Algorithmen: Optimierung nach dem Vorbild der Evolution*, Vieweg Verlag, Braunschweig, Wiesbaden, **1997**.

[53] I. Gerdes, F. Klawonn, R. Kruse, *Evolutionäre Algorithmen: Genetische Algorithmen - Strategie und Optimierungsverfahren- Beispielanwendungen*, 1 . Auflage, Vieweg Verlag, Wiesbaden, **2004**.

[54] M. K. Beyer, Nanocal, **2010-2013**.

[55] W. A. Donald, R. D. Leib, M. Demireva, B. Negru, D. M. Neumark, E. R. Williams, *J. Phys. Chem. A* **2011**, *115*(1), 2.

[56] F. Jensen, *Introduction to Computational Chemistry*, 2 . Auflage, Wiley-VCH Verlag, Weinheim, **2007**.

[57] B. Hartke, *Theoretische Chemie 1: Quantenchemie: http://ravel.pctc.uni-kiel.de/scripts/TC1/folien.pdf*, **2012**.

[58] P.W. Atkins, *Physikalische Chemie*, 3. korr . Auflage, Wiley-VCH Verlag, Weinheim, **2004**.

[59] P. Hohenberg, W. Kohn, *Phys. Rev.* **1964**, (136(3B)), B864.

[60] W. Kohn, L. J. Sham, *Phys. Rev.* **1965**, (140(4a)), A1133.

[61] J. B. Foresman, A. Frisch, *Exploring Chemistry with Electronic Structure Methods*, 2 . Auflage, Gaussian Inc., Pittsburgh, **1996**.

[62] G. Taylor, *Proc. R. Soc. London, Ser. A* **1964**, *280*(1382), 383.

[63] A. D. Becke **1988**, *38*(3098-3100).

[64] P. B. Armentrout, L. F. Halle, J. L. Beauchamp, *J. Chem. Phys.* **1982**, *76*(5), 2449.

[65] B. Bandyopadhyay, K. N. Reishus, M. A. Duncan, *J. Phys. Chem. A* **2013**, *117*(33), 7794.

[66] A. Irigoras, O. Elizalde, I. Silanes, J. E. Fowler, J. M. Ugalde, *J. Am. Chem. Soc.* **2000**, *122*(1), 114.

[67] D. Lessen, P. J. Brucat, *Chem. Phys. Lett.* **1988**, *149*(1), 10.

[68] C. van der Linde, R. F. Höckendorf, O. P. Balaj, M. K. Beyer, *Chem. Eur. J.* **2013**, *19*(11), 3741.

[69] K. Furukawa, K. Ohashi, N. Koga, T. Imamura, K. Judai, N. Nishi, H. Sekiya, *Chem. Phys. Lett.* **2011**, *508*(4-6), 202.

[70] L. Poisson, L. Dukan, O. Sublemontier, F. Lepetit, F. Réau, P. Pradel, J.-M. Mestdagh, J.-P. Visticot, *Int. J. Mass Spectrom.* **2002**, *220*(2), 111.

[71] N. F. Dalleska, K. Honma, L. S. Sunderlin, P. B. Armentrout, *J. Am. Chem. Soc.* **1994**, *116*(8), 3519.

[72] T. G. Dietz, M. A. Duncan, D. E. Powers, R. E. Smalley, *J. Chem. Phys.* **1981**, *74*(11), 6511.

[73] O. P. Balaj, I. Balteanu, B. S. Fox-Beyer, M. K. Beyer, V. E. Bondybey, *Angew. Chem. Int. Ed. Engl.* **2003**, *42*(44), 5516.

[74] X. Chen, E. A. Syrstad, F. Tureček, *J. Phys. Chem. A* **2004**, *108*(18), 4163.

[75] P. Svejda, D. H. Volman, *J. Phys. Chem.* **1970**, *74*(9), 1872.

[76] T.-W. Lam, H. Zhang, C.-K. Siu, *J. Phys. Chem. A* **2015**, .

[77] T. D. Vaden, J. M. Lisy, *J. Phys. Chem. A* **2005**, *109*(17), 3880.

[78] A. A. Shvartsburg, J. G. Wilkes, J. O. Lay, K. W. Michael Siu, *Chem. Phys. Lett.* **2001**, *350*(3-4), 216.

[79] M. Kohler, J. A. Leary, *J. Am. Soc. Mass Spectrom.* **1997**, *8*(11), 1124.

[80] P. Kofel, M. Allemann, H. Kellerhals, K.-P. Wanczek, *Int. J. Mass Spectrom. Ion Processes* **1986**, *72*(1-2), 53.

[81] M. Allemann, H. Kellerhals, K. P. Wanczek, *Int. J. Mass Spectrom. Ion Phys.* **1983**, *46*, 139.

[82] T. Su, M. T. Bowers, *J. Am. Chem. Soc.* **1973**, *95*(23), 7609.

[83] W. M. Haynes, *CRC handbook of chemistry and physics, 95th edition: A ready-reference book of chemical and physical data.*

[84] D. Thoelmann, D. S. Tonner, T. B. McMahon, *J. Phys. Chem.* **1994**, *98*(8), 2002.

[85] C. van der Linde, M. K. Beyer, *J. Phys. Chem. A* **2012**, *116*(44), 10676.

[86] R. S. Walters, E. D. Pillai, M. A. Duncan, *J. Am. Chem. Soc.* **2005**, *127*(47), 16599.

[87] J. S. Daluz, A. Kocak, R. B. Metz, *J. Phys. Chem. A* **2012**, *116*(5), 1344.

[88] T. F. Magnera, D. E. David, J. Michl, *J. Am. Chem. Soc.* **1989**, *111*(11), 4100.

[89] M. Rosi, C. W. Bauschlicher, *J. Chem. Phys.* **1990**, *92*(3), 1876.

[90] J. Roithová, D. Schröder, *Coordin. Chem. Rev.* **2009**, *253*(5-6), 666.

[91] B. S. Fox, M. K. Beyer, V. E. Bondybey, *J. Am. Chem. Soc.* **2002**, *124*(45), 13613.

[92] M. J. Frisch, G. W. Trucks, H. B. Schlegel, G. E. Scuseria, M. A. Robb, J. R. Cheeseman, G. Scalmani, V. Barone, B. Mennucci, G. A. Petersson, H. Nakatsuji, M. Caricato, X. Li, H. P. Hratchian, A. F. Izmaylov, J. Bloino, G. Zheng, J. L. Sonnenberg, M. Hada, M. Ehara, K. Toyota, R. Fukuda, J. Hasegawa, M. Ishida, T. Nakajima, Y. Honda, O. Kitao, H. Nakai, T. Vreven, Montgomery, J., J. A., J. E. Peralta, F. Ogliaro, M. Bearpark, J. J. Heyd, E. Brothers, K. N. Kudin, V. N. Staroverov, R. Kobayashi, J. Normand, K. Raghavachari, A. Rendell, J. C. Burant, S. S. Iyengar, J. Tomasi, M. Cossi, N. Rega, N. J. Millam, M. Klene, J. E. Knox, J. B. Cross, V. Bakken, C. Adamo, J. Jaramillo, R. Gomperts, R. E. Stratmann, O. Yazyev, A. J. Austin, R. Cammi, C. Pomelli, J. W. Ochterski, R. L. Martin, K. Morokuma, V. G. Zakrzewski, G. A. Voth, P. Salvador, J. J.

Dannenberg, S. Dapprich, A. D. Daniels, Ö. Farkas, J. B. Foresman, J. V. Ortiz, J. Cioslowski, D. J. Fox, Gaussian 09, revision B.01, Gaussian Inc., Wallingford CT **2010**, .

[93] Q. K. Timerghazin, G. H. Peslherbe, *J. Phys. Chem. B* **2008**, *112*(2), 520.

[94] C. van der Linde, A. Akhgarnusch, C.-K. Siu, M. K. Beyer, *J. Phys. Chem. A* **2011**, *115*(36), 10174.

[95] C.-K. Siu, Z.-F. Liu, *Phys. Chem. Chem. Phys.* **2005**, *7*(5), 1005.

[96] G. Kresse, J. Furthmüller, *Phys. Rev. B* **1996**, *54*(16), 11169.

[97] D. Meyerstein, W. A. Mulac, *J. Phys. Chem.* **1968**, *72*(3), 784.

[98] D. Meyerstein, *Acc. Chem. Res.* **1978**, *11*(1), 43.

[99] R. D. Mountain, *J. Phys. Chem. B* **2010**, *114*(49), 16460.

[100] A. Ricca, C. W. Bauschlicher, *J. Phys. Chem.* **1995**, *99*(22), 9003.

[101] R. H. Schultz, P. B. Armentrout, *J. Phys. Chem.* **1993**, *97*(3), 596.

[102] K. Ohashi, J. Sasaki, G. Yamamoto, K. Judai, N. Nishi, H. Sekiya, *J. Chem. Phys.* **2014**, *141*(21), 214307.

[103] B. Wang, H. Hou, Y. Gu, *J. Phys. Chem. A* **2001**, *105*(1), 156.

[104] E. R. Fisher, L. S. Sunderlin, P. B. Armentrout, *J. Phys. Chem.* **1989**, *93*(21), 7375.

[105] D. L. Miller, M. L. Gross, *J. Am. Chem. Soc.* **1983**, *105*(12), 3783.

[106] B. D. Nourse, K. A. Cox, R. G. Cooks, *Org. Mass Spectrom.* **1992**, *27*(4), 453.

[107] A. Kramida, Y. Ralchenko, J. Reader and NIST ASD Team, http://www.nist.gov/pml/data/asd.cfm (2015).

[108] J. K. Kochi, J. W. Powers, *J. Am. Chem. Soc.* **1970**, *92*(1), 137.

[109] J. S. Uppal, R. H. Staley, *J. Am. Chem. Soc.* **1982**, *104*(5), 1238.

[110] V. Baranov, G. Javahery, A. C. Hopkinson, D. K. Bohme, *J. Am. Chem. Soc.* **1995**, *117*(51), 12801.

[111] J. Allison, D. P. Ridge, *J. Am. Chem. Soc.* **1979**, *101*(17), 4998.

[112] R. W. Jones, R. H. Staley, *J. Am. Chem. Soc.* **1980**, *102*(11), 3794.

[113] F. Lang, D. Zewge, I. N. Houpis, R. Volante, *Tetrahedron Lett.* **2001**, *42*(19), 3251.

[114] A. Guijarro, D. M. Rosenberg, R. D. Rieke, *J. Am. Chem. Soc.* **1999**, *121*(17), 4155.

[115] C. van der Linde, M. K. Beyer, *Phys. Chem. Chem. Phys.* **2011**, *13*(15), 6776.

[116] A. F. Holleman, E. Wiberg, N. Wiberg, *Lehrbuch der anorganischen Chemie*, 102., stark umgearbeitete und verb. . Auflage, de Gruyter, Berlin and New York, **2007**.

[117] W. Keim, *Angew. Chem. Int. Ed. Engl.* **1990**, *29*(3), 235.

[118] X. Zhao, A. C. Hopkinson, D. K. Bohme, *Chem. Eur. J.* **2008**, *9*(6), 873.

[119] J. S. Uppal, R. H. Staley, *J. Am. Chem. Soc.* **1980**, *102*(12), 4144.

[120] A. Bjarnason, *Organometallics* **1996**, *15*(15), 3275.

[121] T. G. Dietz, D. S. Chatellier, D. P. Ridge, *J. Am. Chem. Soc.* **1978**, *100*(15), 4905.

[122] Steven Z. Kan, Young C. Xu, Quan Chen, Ben S. Freiser, *Int. J. Mass Spectrom.* **1997**, (32), 1310.

[123] Y. Huang, Ranatunga, Don Rufus A., B. S. Freiser, *J. Am. Chem. Soc.* **1994**, *116*(11), 4796.

[124] F. Ullmann, *Ber. Dtsch. Chem. Ges.* **1903**, *36*(2), 2382.

[125] I. Goldberg, *Ber. Dtsch. Chem. Ges.* **1906**, *39*(2), 1691.

[126] A. Klapars, X. Huang, S. L. Buchwald, *J. Am. Chem. Soc.* **2002**, *124*(25), 7421.

[127] M. Rosi, C. W. Bauschlicher, *J. Chem. Phys.* **1990**, *92*(3), 1876.

[128] A. Bjarnason, *Organometallics* **1991**, *10*(5), 1244.

[129] M. Rosi, C. W. Bauschlicher, *J. Chem. Phys.* **1989**, *90*(12), 7264.

[130] A. M. Egorov, *J. Phys. Org. Chem.* **2006**, *19*(10), 664.

[131] C. Jubert, P. Knochel, *J. Org. Chem.* **1992**, *57*(20), 5425.

[132] N. Hoshi, K. Sasaki, S. Hashimoto, Y. Hori, *J. Electroanal. Chem.* **2004**, *568*, 267.

[133] A. G. Orpen, L. Brammer, F. H. Allen, O. Kennard, D. G. Watson, R. Taylor, *J. Chem. Soc., Dalton Trans.* **1989**, (12), S1.

[134] P. E. Fanta, *Synthesis* **1974**, *1974*(01), 9.

[135] P. Y. S. Lam, C. G. Clark, S. Saubern, J. Adams, K. M. Averill, D. M. T. Chan, A. Combs, *Synlett* **2000**, *2000*(05), 0674.

[136] S. Zhang, Y. Ding, *Organometallics* **2011**, *30*(3), 633.

[137] A. Bjarnason, J. W. Taylor, *Organometallics* **1989**, *8*(8), 2020.

[138] A. O. King, E. Negishi, F. J. Villani, A. Silveira, *J. Org. Chem.* **1978**, *43*(2), 358.

[139] F. F. Kneisel, M. Dochnahl, P. Knochel, *Angew. Chem. Int. Ed. Engl.* **2004**, *43*(8), 1017.

[140] E. R. Fisher, R. H. Schultz, P. B. Armentrout, *J. Phys. Chem.* **1989**, *93*(21), 7382.

[141] A. Irigoras, J. E. Fowler, J. M. Ugalde, *J. Am. Chem. Soc.* **1999**, *121*(3), 574.

[142] M. Citir, R. B. Metz, *J. Chem. Phys.* **2008**, *128*(2), 024307.

[143] N. R. Walker, R. S. Walters, E. D. Pillai, M. A. Duncan, *J. Chem. Phys.* **2003**, *119*(20), 10471.

[144] J. Sasaki, K. Ohashi, K. Inoue, T. Imamura, K. Judai, N. Nishi, H. Sekiya, *Chem. Phys. Lett.* **2009**, *474*(1-3), 36.

[145] E. Sicilia, N. Russo, *J. Am. Chem. Soc.* **2002**, *124*(7), 1471.

[146] I. Herber, *Experimentelle und theoretische Untersuchungen von Vanadium-Wasserclustern in der Gasphase*, Diplomarbeit, Christian-Albrechts-Universität zu Kiel, Kiel, **2012**.

[147] B. Scharfschwerdt, C. van der Linde, O. Petru Balaj, I. Herber, D. Schütze, M. K. Beyer, *Low Temp. Phys.* **2012**, *38*(8), 717.

[148] J. R. Lakowicz, *Principles of fluorescence spectroscopy*, 3. ed. . Auflage, Springer, New York, NY, **2006**.

[149] C. J. Johnson, L. C. Dzugan, A. B. Wolk, C. M. Leavitt, J. A. Fournier, A. B. McCoy, M. A. Johnson, *J. Phys. Chem. A* **2014**, *118*(35), 7590.

[150] T. Yanai, D. P. Tew, N. C. Handy, *Chem. Phys. Lett.* **2004**, *393*(1-3), 51.

[151] B. M. Marsh, J. Zhou, E. Garand, *J. Phys. Chem. A* **2014**, *118*(11), 2063.

A. Appendices

A.1. Supporting Information – Chapter 3

Tables with structural parameters, relative energies, and free energies of selected calculated structures and the full Cartesian coordinates, harmonic frequencies, and energies of all calculated structures are available free of charge on the ACS Publications website at:

DOI:10.1021/acs.jpca.5b02946.

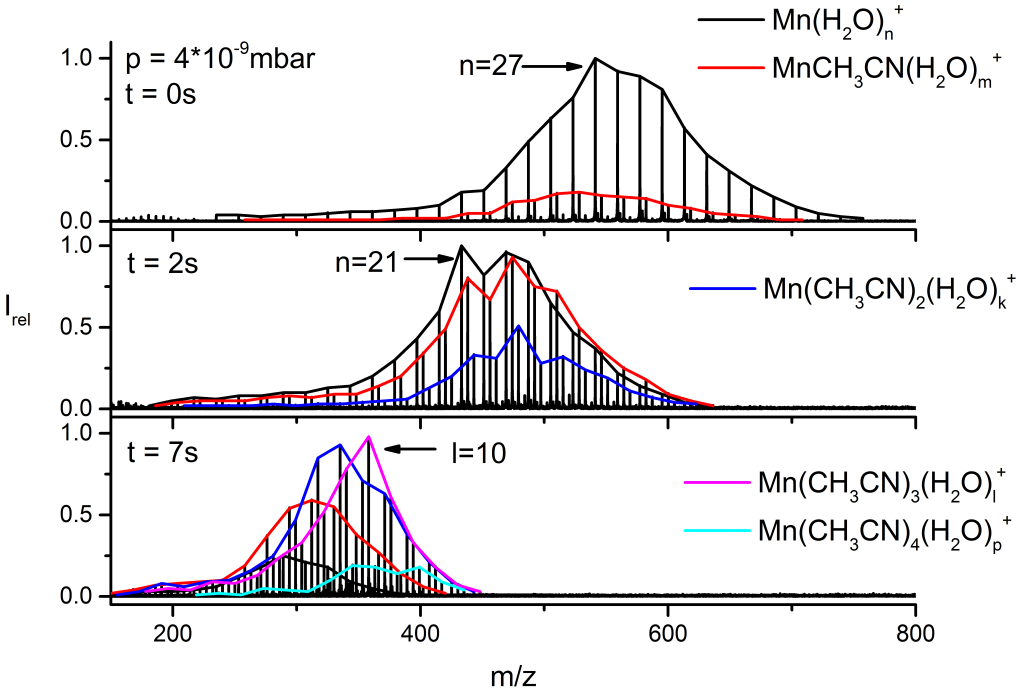

Figure A.1.: Mass spectra of the reaction of $[Mn(H_2O)_n]^+$ with CH_3CN at a pressure of 4 x 10^{-9} mbar after 0, 2.4 and 7 s. Quantitative formation of $[Mn(CH_3CN)_4(H_2O)_p]^+$ is observed.

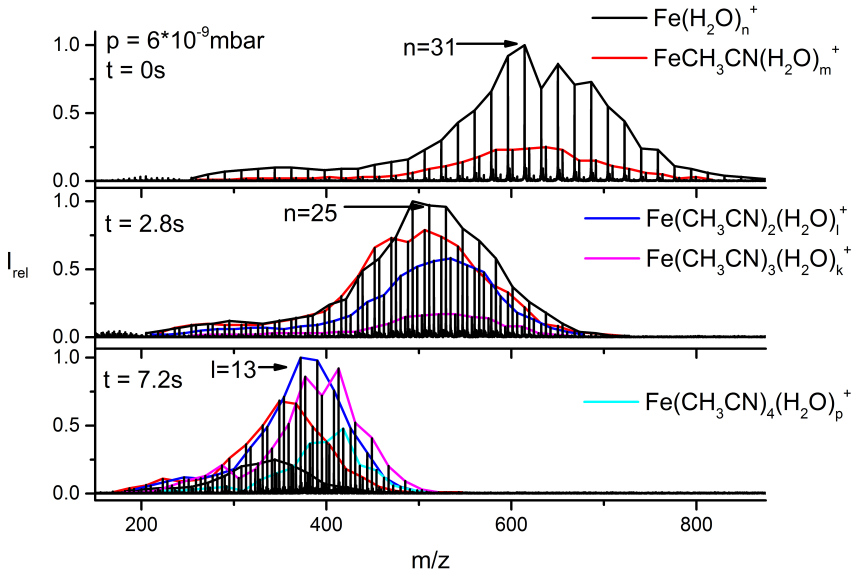

Figure A.2.: Mass spectra of the reaction of $[Fe(H_2O)_n]^+$ with CH_3CN at a pressure of 6 x 10^{-9} mbar after 0, 2.8 and 7 s. Stepwise uptake of four acetonitrile molecules is observed.

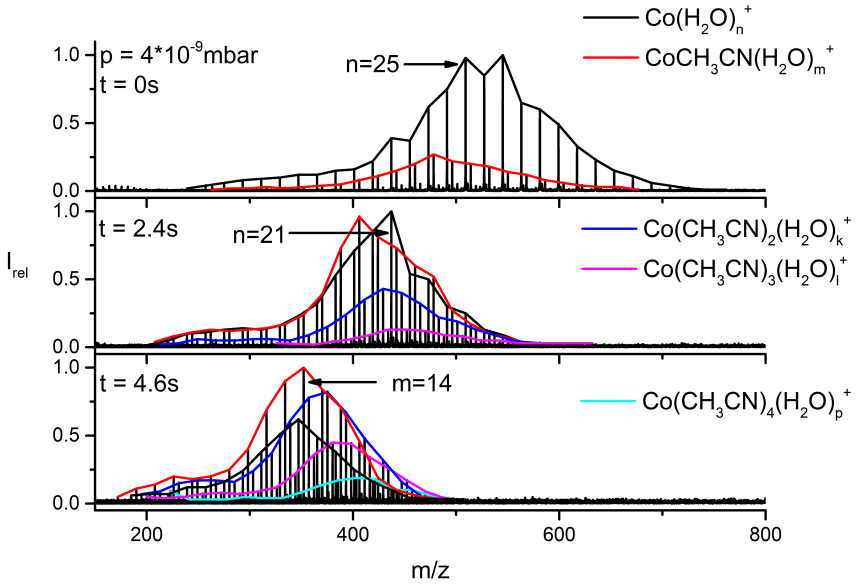

Figure A.3.: Mass spectra of the reaction of $[Co(H_2O)_n]^+$ with CH_3CN at a pressure of 4 x 10^{-9} mbar after 0, 2.4 and 4.6 s. Quantitative formation of $[Co(CH_3CN)_4(H_2O)_p]^+$ is observed.

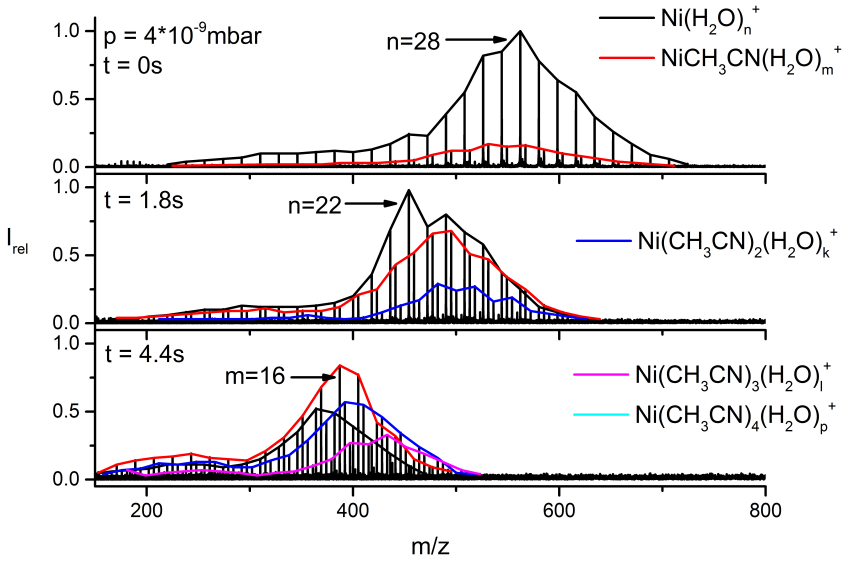

Figure A.4.: Mass spectra of the reaction of $[Ni(H_2O)_n]^+$ with CH_3CN at a pressure of 4 x 10^{-9} mbar after 0, 1.8 and 4.4 s. Uptake of up to four acetonitrile molecules is determined.

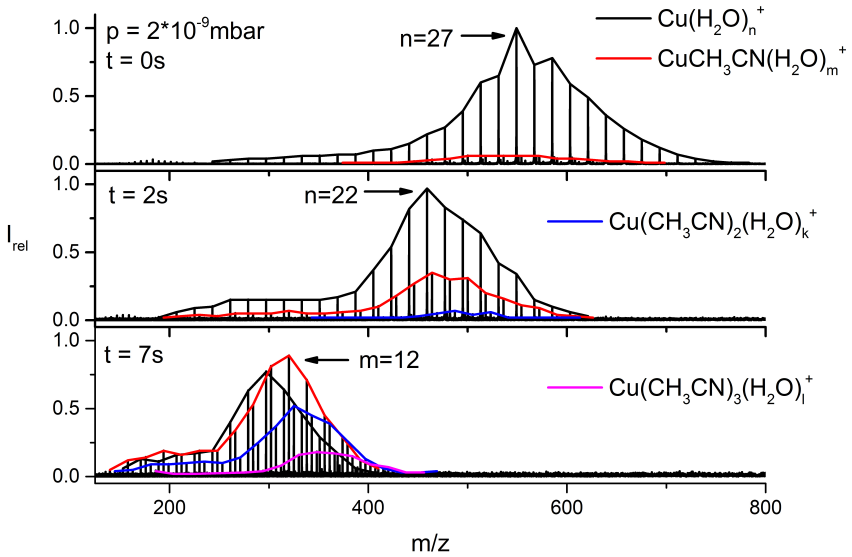

Figure A.5.: Mass spectra of the reaction of $[Cu(H_2O)_n]^+$ with CH_3CN at a pressure of 2 x 10^{-9} mbar after 0, 2 and 7 s. Formation of $[Cu(CH_3CN)_3(H_2O)]_l^+$ is observed.

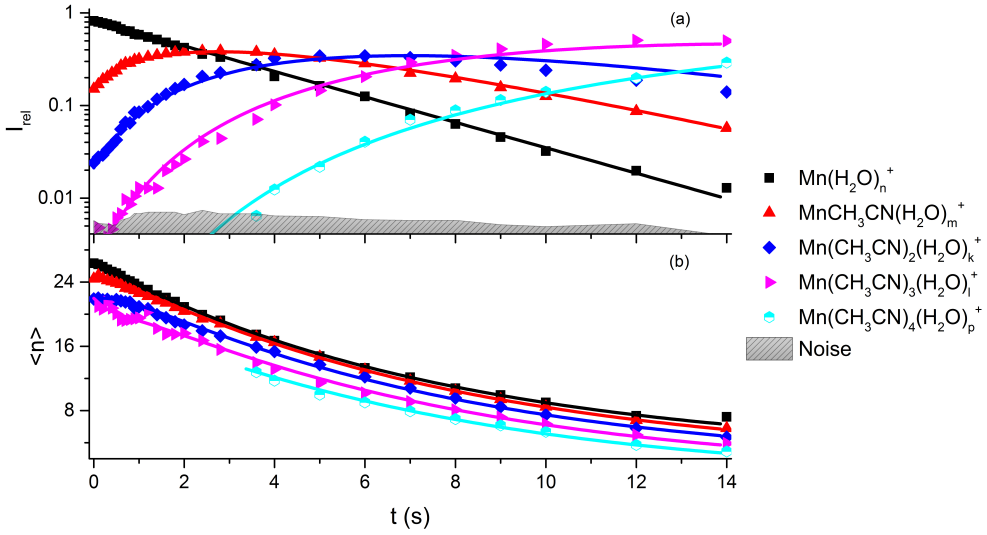

Figure A.6.: Kinetics and average cluster size <n> for the reaction of $[Mn(H_2O)_n]^+$ with CH_3CN at 4 x 10^{-9} mbar for the first 14 seconds. The kinetics shows the uptake of four acetonitrile molecules with pseudo-first-order behavior for up to 14 s.

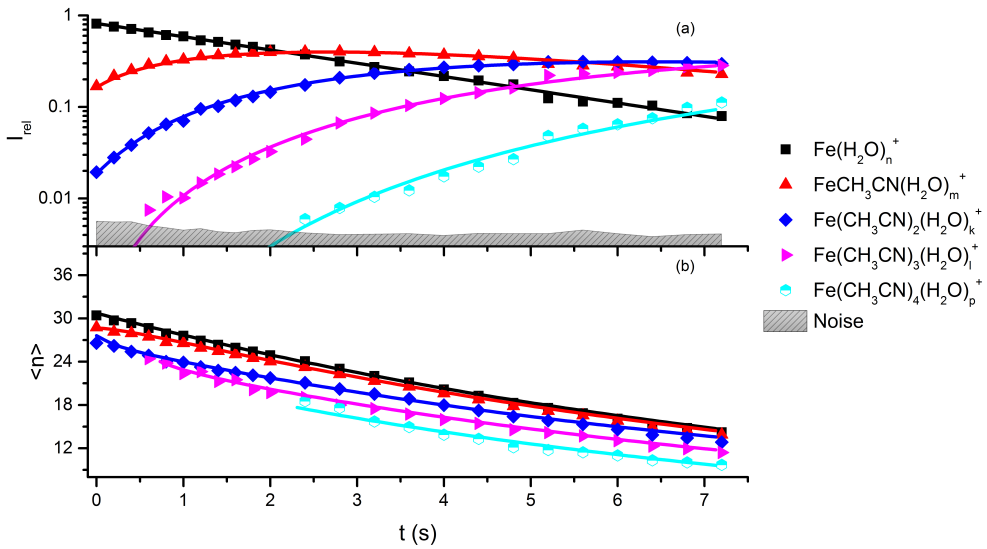

Figure A.7.: Kinetic plots and average cluster size <n> for the reaction of $[Fe(H_2O)_n]^+$ with CH_3CN at 6 x 10^{-9} mbar for the first 7 seconds. Iron show a good pseudo-first-order fit and the uptake of four acetonitrile molecules.

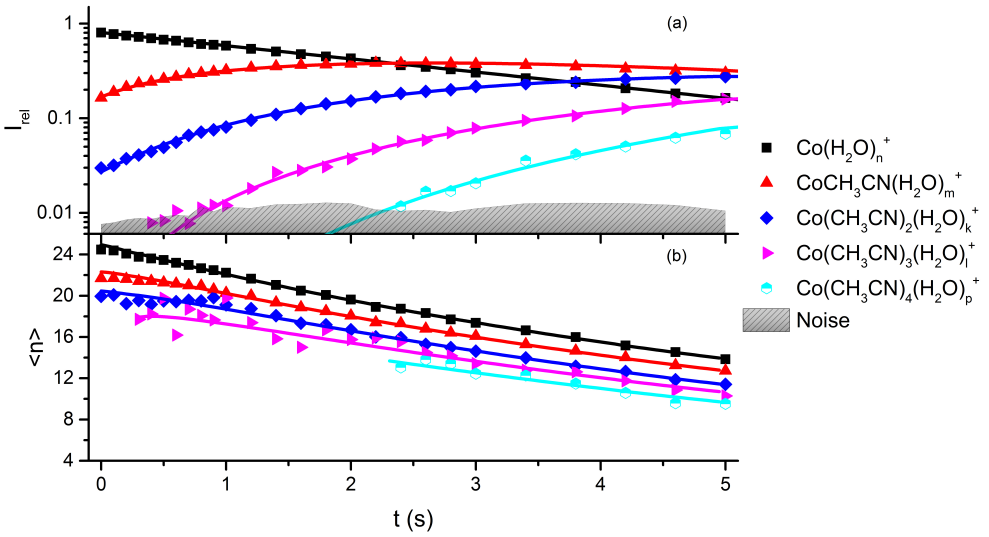

Figure A.8.: Kinetics and average cluster size <n> of the reaction of $[Co(H_2O)_n]^+$ with CH_3CN at 4 x 10^{-9} mbar. The kinetic shows a pseudo-first-order behavior. A stepwise uptake of four acetonitrile molecules is observed during the first 5 s.

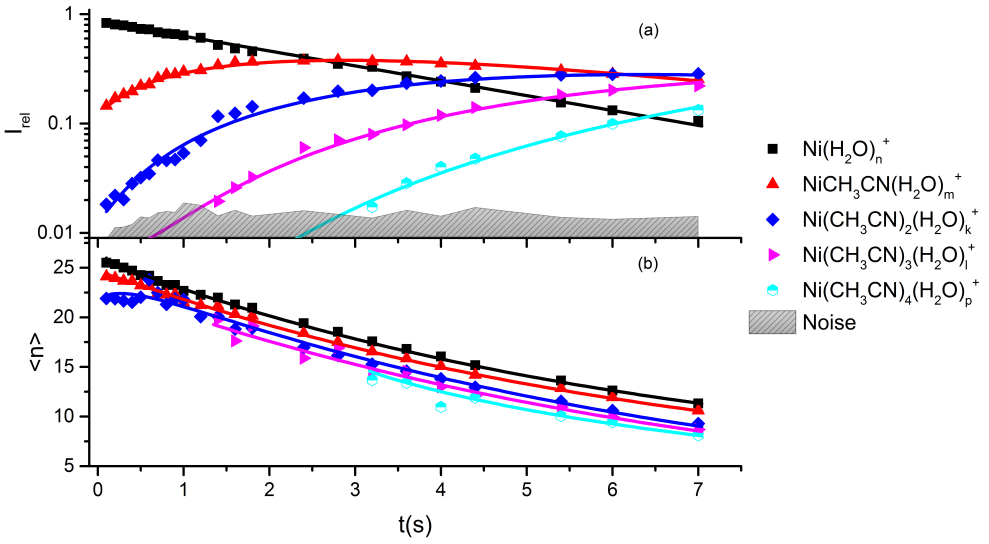

Figure A.9.: Kinetic plots and average cluster size <n> for the reaction of $[Ni(H_2O)_n]^+$ with CH_3CN at 4 x 10^{-9} mbar for the first 7 seconds. The kinetic shows four consecutive reactions in the first 7 s with pseudo-first-order behavior.

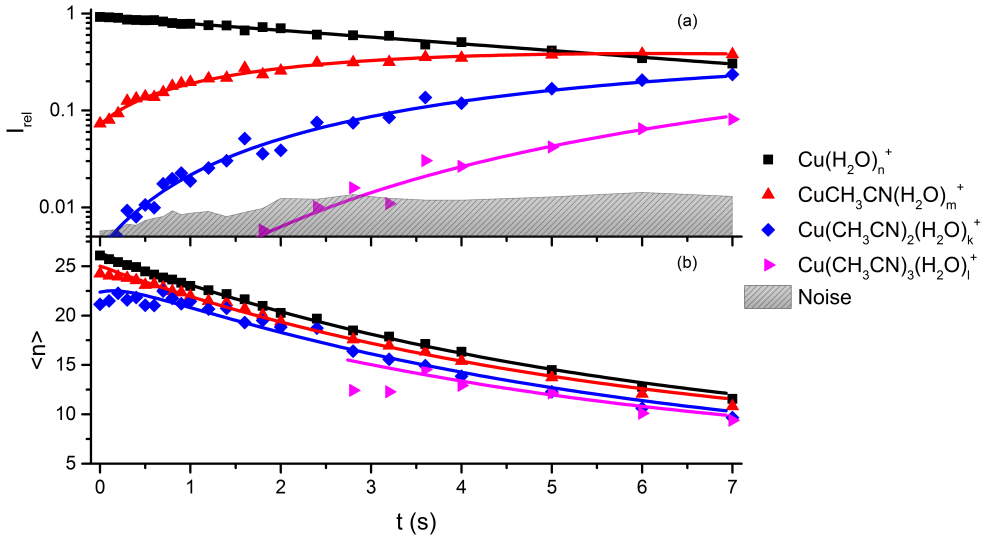

Figure A.10.: Kinetics and average cluster size <n> for the reaction of $[Cu(H_2O)_n]^+$ with CH_3CN at 2 x 10^{-9} mbar for the first 7 seconds. The kinetics show three consecutive reactions with pseudo-first-order behavior, uptake of the fourth acetonitrile molecule occurs only later.

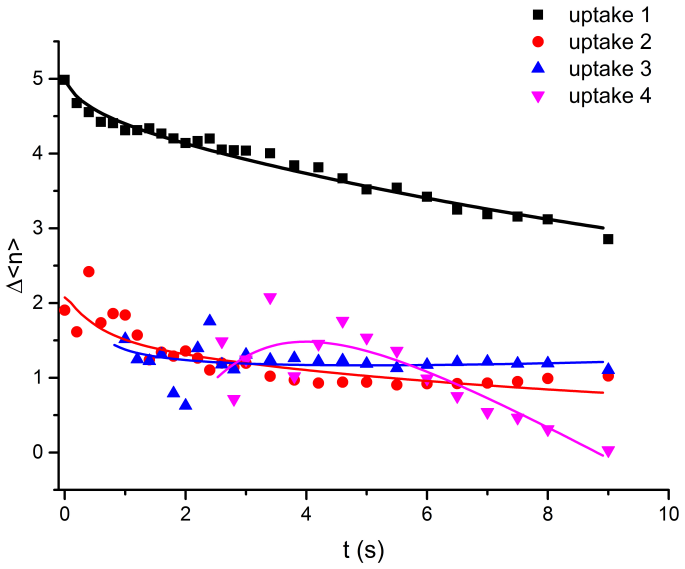

Figure A.11.: Difference Fit for reaction of $[Cr(H_2O)_n]^+$ with CH_3CN. The 4^{th} uptake signifies a pronounced cluster size dependence.

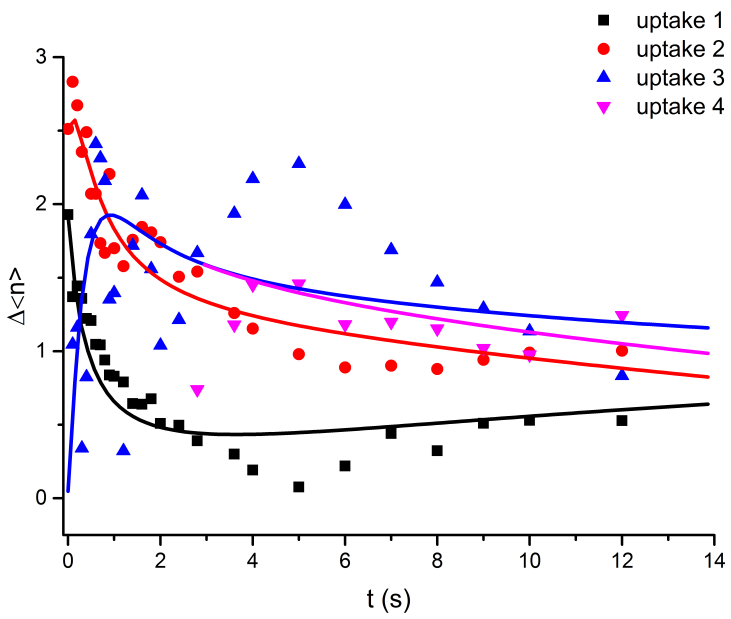

Figure A.12.: Difference Fit for reaction of $[Mn(H_2O)_n]^+$ with CH_3CN. All uptake steps are strongly size dependent.

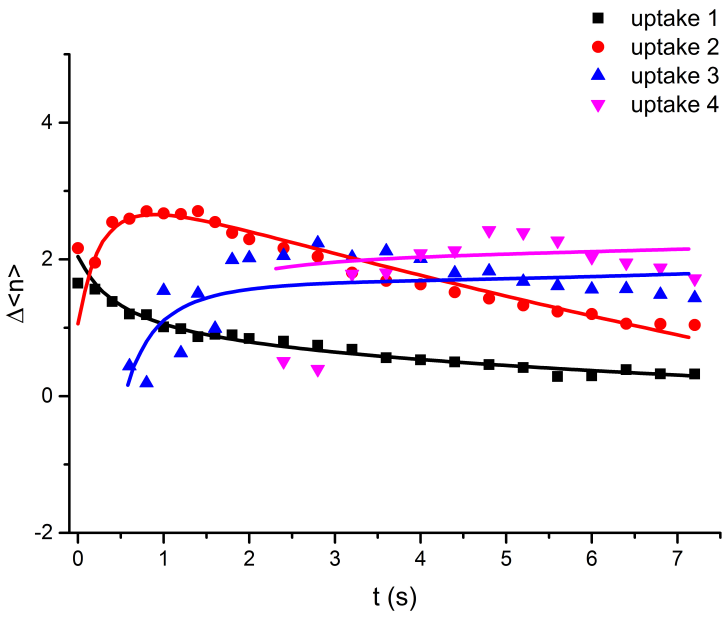

Figure A.13.: Difference Fit for reaction of $[Fe(H_2O)_n]^+$ with CH_3CN. Size dependence is strong starting with the 2nd uptake.

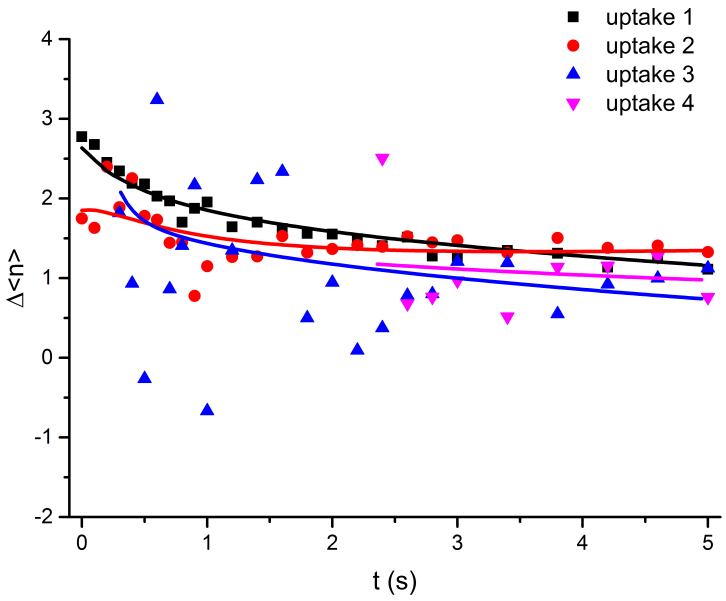

Figure A.14.: Difference Fit for reaction of $[Co(H_2O)_n]^+$ with CH_3CN. Data points are scattered due to low intensities.

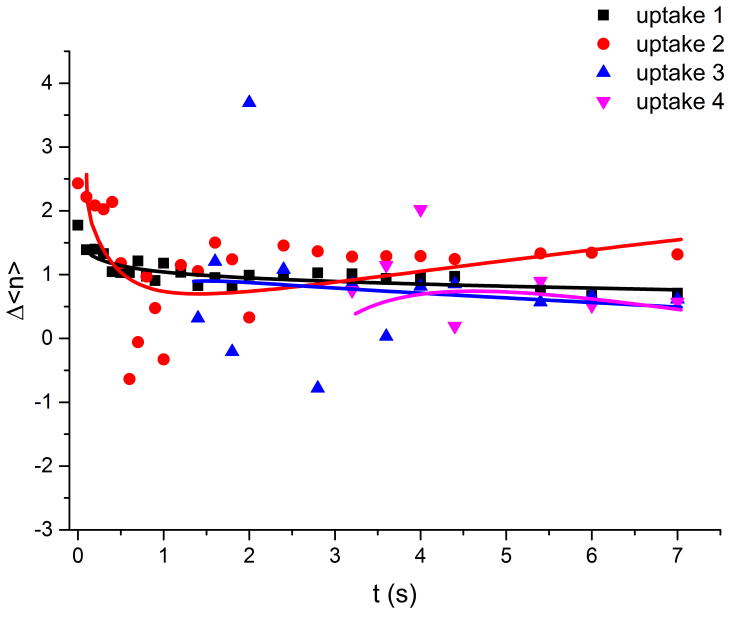

Figure A.15.: Difference Fit for reaction of $[Ni(H_2O)_n]^+$ with CH_3CN. The plot shows that the analysis of the second and subsequent uptakes is not useable.

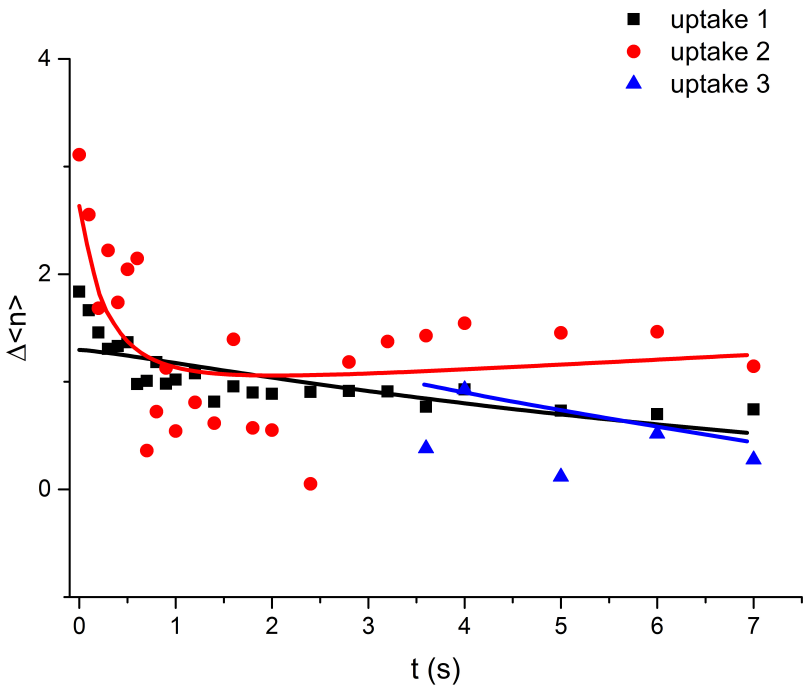

Figure A.16.: Difference Fit for reaction of $[Cu(H_2O)_n]^+$ with CH_3CN. Again, only the first step can be used.

A.2. Supporting Information – Chapter 4

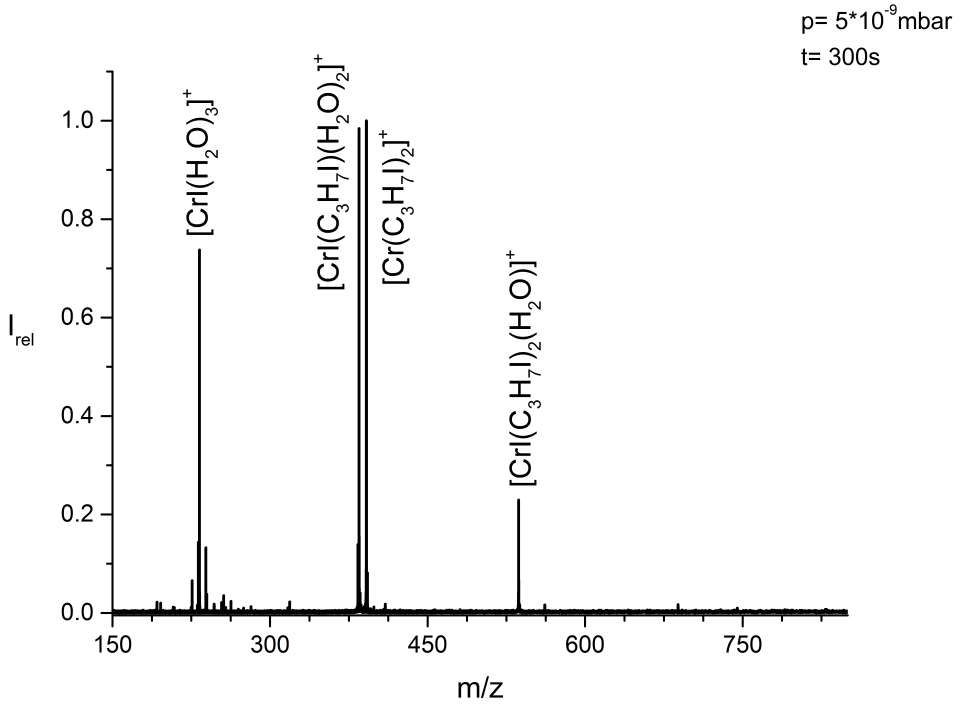

Figure A.17.: Mass spectrum of the reaction of $[Cr(H_2O)_n]^+$ with C_3H_7I at a pressure of 5 x 10^{-9} mbar after 300 s. Ligand exchange and oxidation reaction with 1–iodopropane molecules was observed. Small peaks due to products with impurities are observed as well.

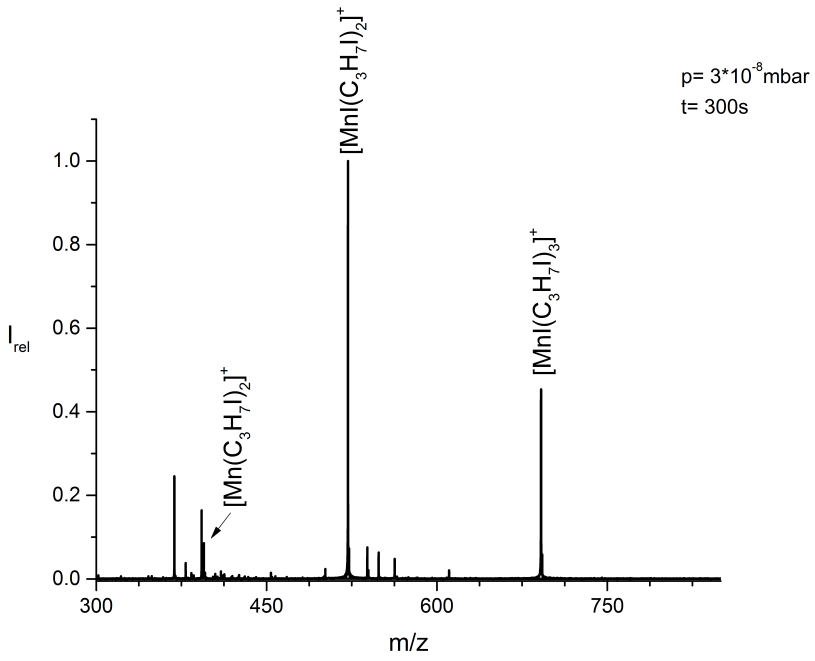

Figure A.18.: Mass spectrum of the reaction of $[Mn(H_2O)_n]^+$ with C_3H_7I at a pressure of 3 x 10^{-8} mbar after 300 s. Formation of $[MnI(C_3H_7)_2]^+$ and $[MnI(C_3H_7)_3]^+$ is observed for long reaction delays. Product peaks with impurities, like limonene and isoprene, and dimers are observed at long reaction delays.

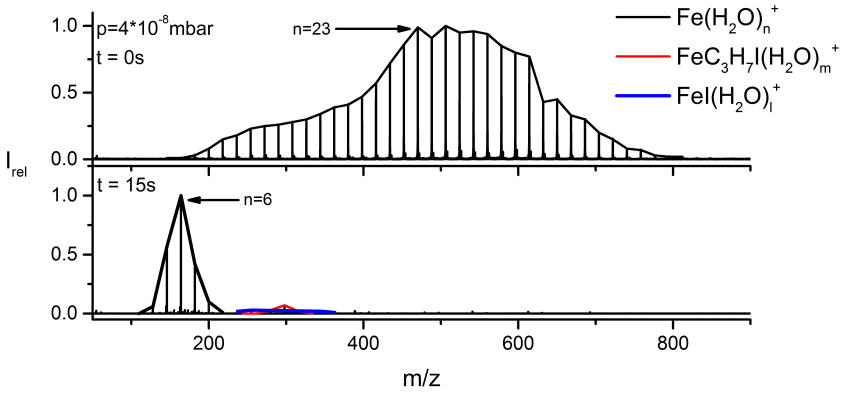

Figure A.19.: Mass spectra of the reaction of $[Fe(H_2O)_n]^+$ with C_3H_7I at a pressure of 4 x 10^{-8} mbar after 0 and 15 s. Ligand exchange and oxidation reaction with 1-iodopropane molecules was observed.

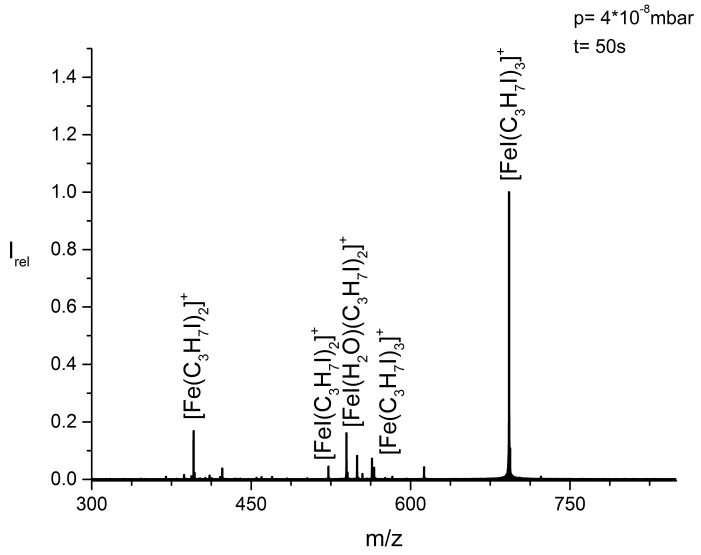

Figure A.20.: Mass spectrum of the reaction of $[Fe(H_2O)_n]^+$ with C_3H_7I at a pressure of 4 x 10^{-8} mbar after 50 s. Formation of $[FeI(C_3H_7)_2]^+$ and $[FeI(C_3H_7)_3]^+$ is observed for long reaction delays. Product peaks with impurities, like limonene and isoprene, and dimers are observed at long reaction delays.

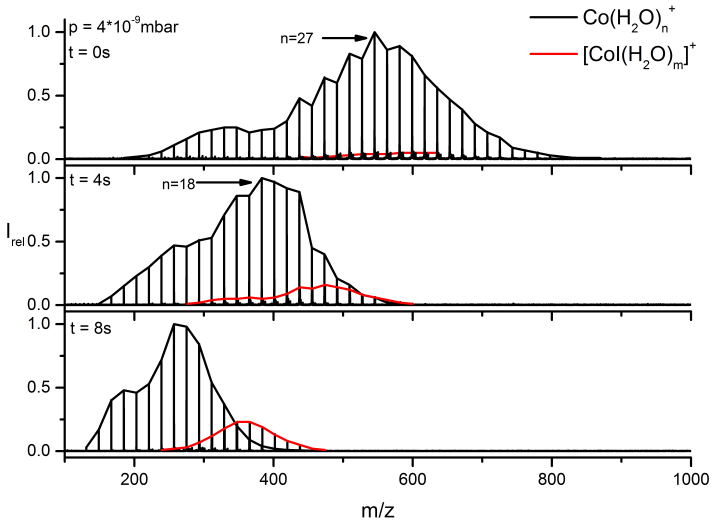

Figure A.21.: Mass spectra of the reaction of $[Co(H_2O)_n]^+$ with C_3H_7I at a pressure of 4 x 10^{-9} mbar after 0, 4 and 8 s. Quantitative formation of $[CoI(H_2O)_m]^+$ is observed.

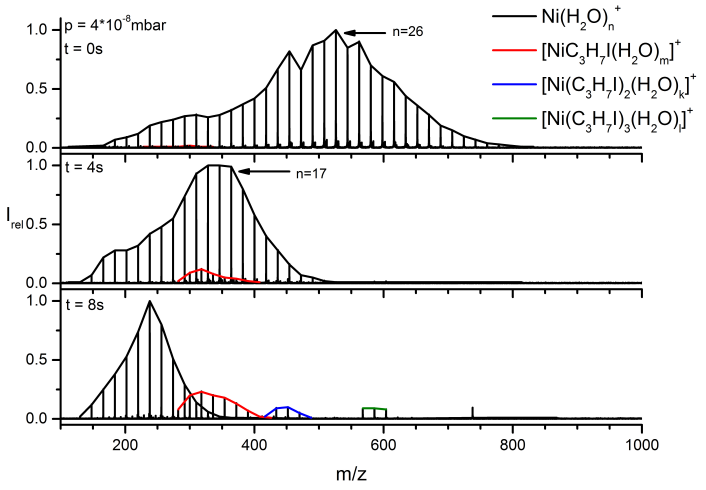

Figure A.22.: Mass spectra of the reaction of $[Ni(H_2O)_n]^+$ with C_3H_7I at a pressure of 4 x 10^{-8} mbar after 0, 4 and 8 s. Quantitative formation of $[NiC_3H_7I(H_2O)_m]^+$ is observed. At 8 s reaction delay also the sequential uptake of three further iodopropane molecules is determined.

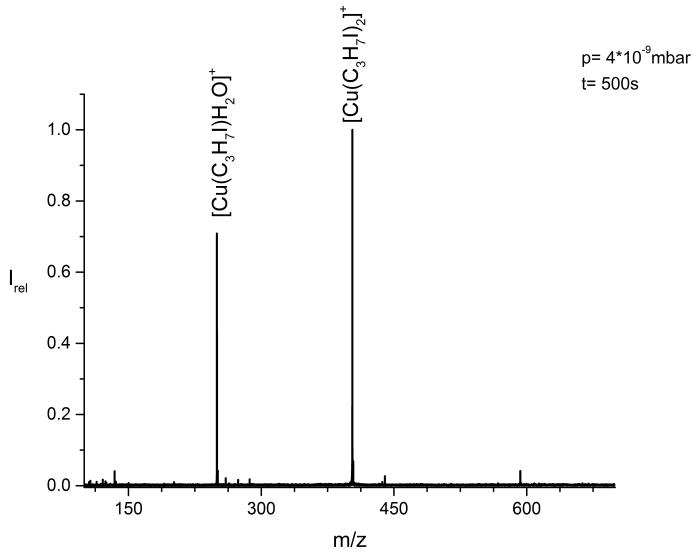

Figure A.23.: Mass spectrum of the reaction of $[Cu(H_2O)_n]^+$ with C_3H_7I at a pressure of 4 x 10^{-9} mbar after 500 s. The ligand exchange with two 1–iodopropane molecules and a high stability of $[CuC_3H_7I(H_2O)]^+$ was observed. Small peaks belongs either to products of impurities.

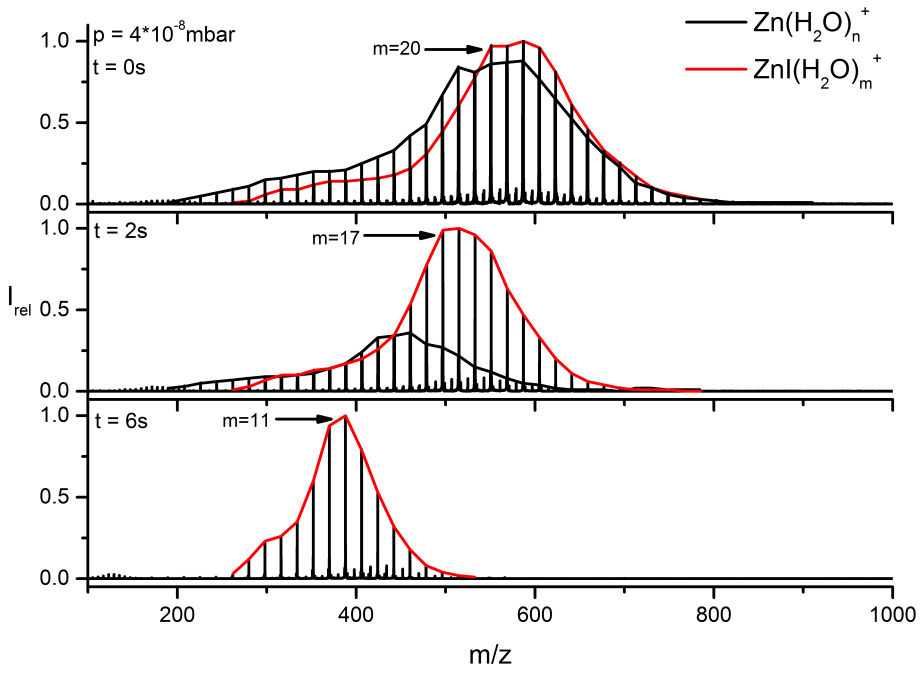

Figure A.24.: Mass spectra of the reaction of $[Zn(H_2O)_n]^+$ with C_3H_7I at a pressure of 4 x 10^{-8} mbar after 0, 2 and 6 s. Quantitative formation of $[ZnI(H_2O)_m]^+$ is observed. The small peaks are the zinc dimers with water and with one iodide.

A.3. Supporting Information – Chapter 5

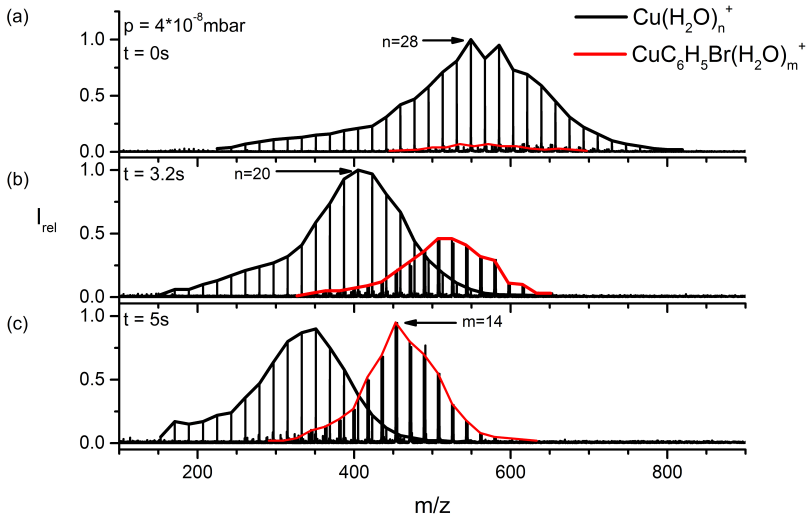

Figure A.25.: Mass spectra of the reaction of $[Cu(H_2O)_n]^+$ with C_6H_5Br at a pressure of 4 x 10^{-8} mbar after 0, 3.2 and 5 s. Quantitative formation of $[CuC_6H_5Br(H_2O)_m]^+$ is observed. The product signal consists of doublets due to the ^{81}Br isotope.

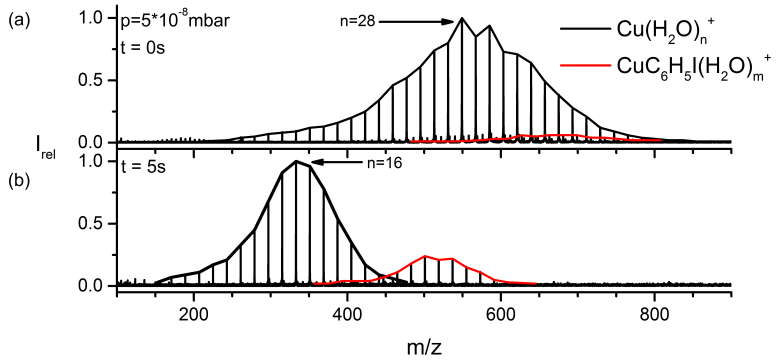

Figure A.26.: Mass spectra of the reaction of $[Cu(H_2O)_n]^+$ with C_6H_5I at a pressure of 5 x 10^{-8} mbar after 0 and 5 s. Quantitative formation of $[CuC_6H_5I(H_2O)_m]^+$ is observed. The reaction proceeds slowly. .

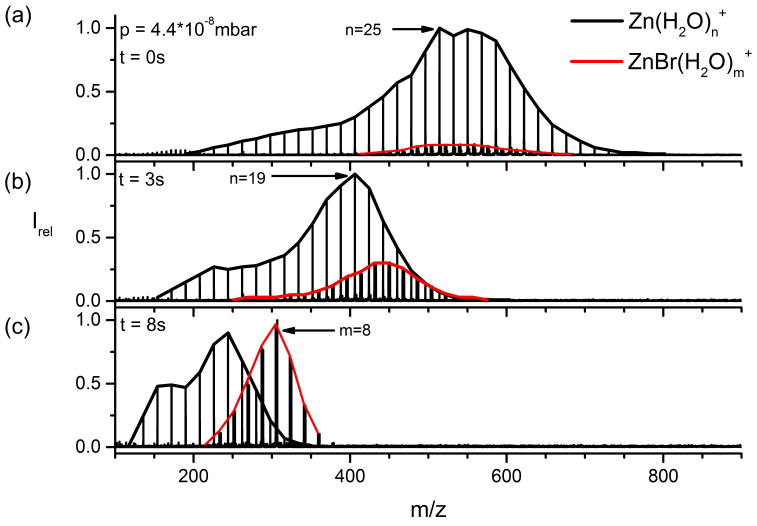

Figure A.27.: Mass spectra of the reaction of $[Zn(H_2O)_n]^+$ with C_6H_5Br at a pressure of 4.4 x 10^{-8} mbar after 0, 3 and 8 s. Quantitative formation of $[ZnBr(H_2O)_m]^+$ is observed.

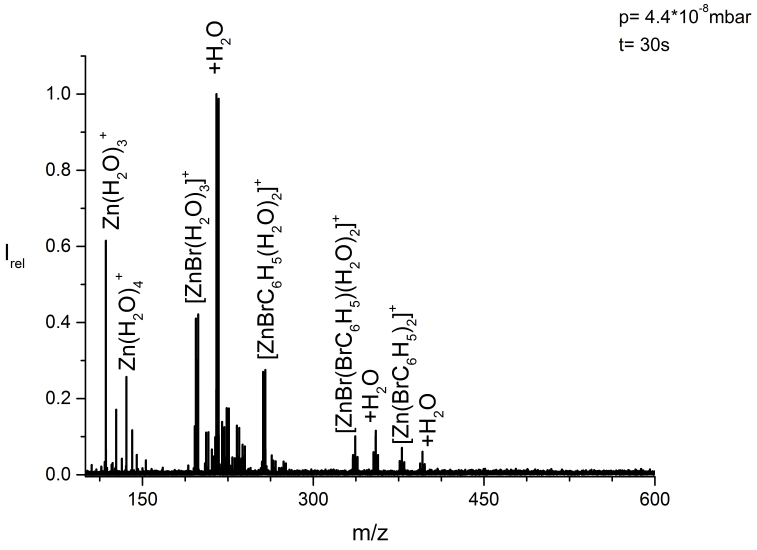

Figure A.28.: Mass spectrum of the reaction of $[Zn(H_2O)_n]^+$ with C_6H_5Br at a pressure of 4.4 x 10^{-8} mbar after 30 s. Quantitative formation of $[ZnBr(H_2O)_m]^+$ and $[ZnC_6H_5Br(H_2O)_m]^+$ is observed. Furthermore small peaks due to reaction with impurities like ammonia of the dimers and of the educt cluster are observed.

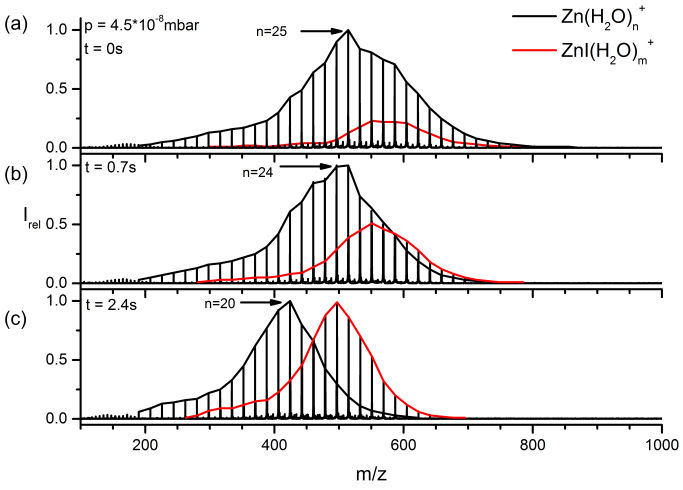

Figure A.29.: Mass spectra of the reaction of $[Zn(H_2O)_n]^+$ with C_6H_5I at a pressure of 4.5 x 10^{-8} mbar after 0, 0.7 and 2.4 s. Quantitative formation of $[ZnI(H_2O)_m]^+$ is observed.

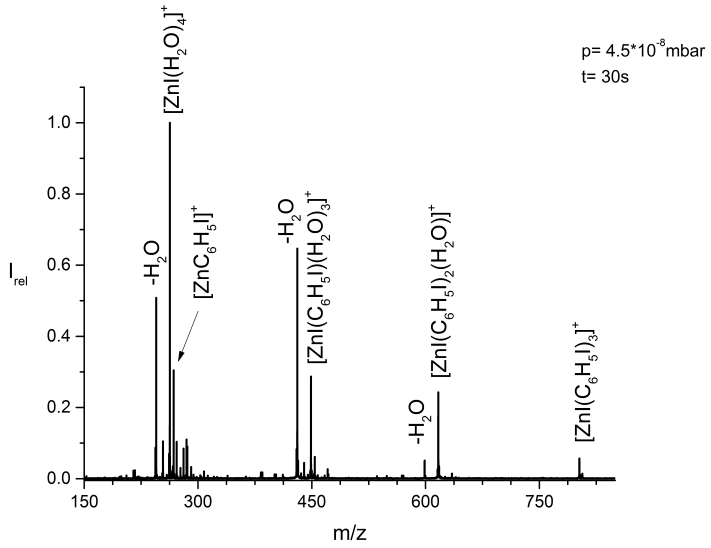

Figure A.30.: Mass spectrum of the reaction of $[Zn(H_2O)_n]^+$ with C_6H_5I at a pressure of 4.5 x 10^{-8} mbar after 30 s. Quantitative formation of $[ZnI(H_2O)_m]^+$ and $[ZnC_6H_5I(H_2O)_m]^+$ is observed. Furthermore small peaks due to reaction with impurities like ammonia of the dimers and of the educt cluster are observed.

B. Publications und Poster

2015

"Reactivity of Hydrated Monovalent First Row Transition Metal Ions $M^+(H_2O)_n$, M= Cu and Zn, towards C_6H_5Cl, C_6H_5Br, C_6H_5I and C_3H_7I." 48. DGMS Jahrestagung, Wuppertal (Germany), March 01 - 03

"Reactivity of hydrated monovalent first row transition metal ions $M(H_2O)_n^+$, M = Cr, Mn, Fe, Co, Ni, Cu and Zn, n < 50, toward acetonitrile" Ina Herber, Wai-Kit Tang, Ho-Yin Wong, Tim-Wai Lam, Chi-Kit Siu, and Martin K. Beyer, *The Journal of Physical Chemistry A*, 2015, 119 (22), pp. 5566–5578

2014

"Reactivity of Hydrated Monovalent First Row Transition Metal Ions $M^+(H_2O)_n$, M= Cu and Zn, towards C_6H_5Cl, C_6H_5Br, C_6H_5I and C_3H_7I." 20th International Mass Spectrometry Conference, Geneva (Switzerland), August 24 - 29

"Reactivity of Hydrated Monovalent First Row Transition Metal Ions $M^+(H_2O)_n$, M= Cr, Mn, Fe, Ni, Co, Cu and Zn, toward Acetonitrile." Gordon Research Conference on Molecular & Ionic Clusters, Lucca (Italy), April 27 - May 02

"Reactivity of Hydrated Monovalent First Row Transition Metal Ions $M^+(H_2O)_n$, M= Cr, Mn, Fe, Ni, Co, Cu and Zn, toward Acetonitrile." Symposium on Atomic, Cluster and Surface Physics (SASP) 2014, Obergurgl (Austria), February 09 - 14

2013

"Reactivity of Hydrated Monovalent First Row Transition Metal Ions $M^+(H_2O)_n$, M= Cr, Mn, Fe, Ni, Co, Cu and Zn, toward Acetonitrile." Clustertreffen 2013, Herzogenhorn (Germany), October 06 - 11

"Kinetic analysis of $V^+(H_2O)_n$, n = 8-12, at low temperature in the gas phase." Bunsentagung 2013, Karlsruhe (Germany), May 09 - 11

"Kinetic analysis of $V^+(H_2O)_n$, n = 8-12, at low temperature in the gas phase." Symposium on Size Selected Clusters (S^3C), Davos (Switzerland), March 03 - 08

Acknowledgment

Ich möchte mich hiermit ganz herzlich bei allen bedanken, die zum Gelingen dieser Doktorarbeit beigetragen haben.

Bei meinem Betreuer Prof. Dr. Martin K. Beyer möchte ich mich für die interessante Themenstellung und die Betreuung der Dissertation bedanken. Außerdem möchte ich mich für die Möglichkeit meine Arbeit auf unterschiedlichen Konferenzen präsentieren zu können bedanken.

Des Weiteren möchte ich mich nochmal bei Herrn Dr. O. P. Balaj für die Begleitung und Einarbeitung im ICR-Labor herzlich bedanken. Ich möchte mich auch herzlich bei Amou Akhgarnusch und Christian van der Linde für die Unterstützung bei Problemstellungen und gute Zusammenarbeit bedanken.

Ebenso gilt ein besonderes Dankeschön an Nina Bersenkowitsch und Andreas Herburger für die anregenden Diskussionen und das angenehme Arbeitsklima. Weiterhin bedanke ich mich bei Benjamin Lachmann für Hilfe bei Fragestellungen zu Programmen und Aufmunterungen durch Wanderausflüge, um den Kopf wieder frei zu bekommen.

Ich bedanke mich auch herzlich bei Irmgard Staud für die administrative Hilfe. Auch möchte ich mich bei den Mitarbeitern der Werkstatt in Kiel und in Innsbruck für die Reparaturen bedanken, ohne die ein schnelles Vorankommen der Arbeit nicht möglich wäre.

Außerdem möchte ich mich herzlich bei Sascha Frick und Dr. Andreas Mauracher für die Hilfe bei Fragestellungen zu den quantenmechanischen Berechnungen bedanken. Ein besonderer Dank gilt Dr. Andreas Mauracher für die Hilfe und Installation des LEO3 Zuganges.

Bei allen nicht namentlich genannten Personen, die mich in meiner Promotion unterstützt haben, danke ich für die aufmunternden Worte und die Hilfe. Auch möchte ich Richard Bedwell für die Hilfe bei Problemstellungen mit der englischen Sprache danken.

Vor allem möchte ich mich bei meinen Eltern Valentina und Ernst sowie meinem Bruder Eduard für die moralische und finanzielle Hilfe während meiner Studienzeit und meiner Promotion bedanken.

Zuletzt möchte ich mich bei Claus Gernert für die Motivation und Unterstützung während der Promotion herzlich bedanken. Besonders für die Mühe und die unternommenen Anstrengungen, die durch die räumliche Trennung während der letzten beiden Jahre entstanden sind, möchte ich mich bedanken.

Eigenanteil an der verwendeten Publikation

Chapter 3 *The Journal of Physical Chemistry A*, 2015, 119 (22), pp. 5566–5578
Durchführung der Experimente, Auswertung der Daten und Erstellung der ersten Fassung des Manuskriptes für den experimentellen Teil des Zeitungsartikels.

Erklärung der Urheberschaft

Ich erkläre hiermit an Eides statt, dass ich die vorliegende Dissertation - abgesehen von der Beratung meines Betreuers Prof. Dr. Martin K. Beyer - ohne Hilfe Dritter und ohne Benutzung anderer als der angegebenen Hilfsmittel angefertigt habe; die aus fremden Quellen direkt oder indirekt übernommenen Gedanken sind als solche kenntlich gemacht. Die Arbeit wurde bisher in gleicher oder ähnlicher Form in keiner anderen Prüfungsbehörde vorgelegt und auch noch nicht veröffentlicht. Kapitel 3 wurde in der vor dem Kapitel angegebenen Zeitschrift veröffentlicht.

Die Arbeit ist unter Einhaltung der Regeln der guten wissenschaftlichen Praxis der Deutschen Forschungsgemeinschaft (DFG) entstanden.

Ort, Datum Unterschrift